
The spectrum of atmospheric neutrinos above GeV energies

DISSE

TATION

zur Erlangung des Grades eines
Doktors der Naturwissenschaften

in der Fakulät für Physik und Astronomie
der Ruhr-Universität Bochum

vorgelegt von
Sebastian Schöneberg
aus
Bonn

Bochum 2016

RUHR
UNIVERSITÄT
BOCHUM

RUB

1. Gutachter: Prof. Dr. Julia Tjus
2. Gutachter: Prof. Dr. Dr. Wolfgang Rhode

Datum der Disputation: 18.11.2016

Contents

1	Introduction	1
2	Basic Concepts	3
2.1	Cosmic Rays	3
2.1.1	CR experiments	4
2.1.2	Primary CR flux models	6
2.2	Extended Air Showers	9
2.3	Atmospheric lepton measurements	13
2.3.1	IceCube	14
2.4	Atmospheric lepton fluxes	16
2.5	Neutrino Oscillations	18
2.6	Monte Carlo software	19
3	Phenomenological and Statistical Considerations	23
3.1	Primary CR composition - Superposition approximation	24
3.1.1	Nucleon flux from CR nucleus flux	26
3.2	Importance Sampling	31
3.2.1	Sliding low energy cutoff	31
3.2.2	Forced meson decay	34
3.3	Geometric effects	35
3.3.1	Geomagnetic Cutoff	35
3.3.2	Muons in the Earth's magnetic field	36
3.3.3	Geometry of CORSIKA output	39
3.3.4	Mirroring	41
4	Method: Implementation and Execution	45
4.1	CORSIKA Output	46
4.2	Simulation Parameters	47
4.3	LiDong Cluster	49
4.4	Post-processing	50
4.4.1	Calculation of CR flux weights	51
4.4.2	Oscillation Weights	52
5	Results	55
5.1	Selection of reference CR model	55

5.2	Impact of interaction models in different energy ranges	58
5.3	Comparison with observed fluxes	59
5.4	Comparison with simulation	64
5.4.1	EPOS vs. FLUKA	64
5.4.2	Meson charge ratios	68
5.4.3	Neutrino flavor ratios	68
5.5	Discussion of Uncertainties	72
5.6	Geometry	75
5.6.1	Production height	76
5.6.2	Opening Angle	77
5.6.3	Comparison with Honda	79
5.7	Post-processing options	83
5.7.1	Geomagnetic cutoff	83
5.7.2	Neutrino Oscillations	84
6	Conclusion and Outlook	89
6.1	Summary and Conclusion	89
6.2	Outlook	91
7	Appendix	93
A	Superposition Approximation: Supplemental plots	93
B	Geometry distributions for FLUKA	96
C	Shower Geometry - Attempted 3D corrections	98
Bibliography		103

List of Tables

2.1	Overview of relevant particles in air showers	12
3.1	Muon arrival location	37
4.1	Summary of the simulation parameters.	48

List of Figures

2.1.1 Primary CR specctrum	7
2.1.2 CR composition	8
2.2.1 Air shower schematic	9
2.3.1 Schematic of IceCube and DeepCore	15
2.5.1 Muon neutrino survival probability	19
3.1.1 Superposition: Example helium yield	25
3.1.2 Superposition: Example iron yield	26
3.1.3 Superposition: Muon neutrino flux from iron	27
3.1.4 Superposition: Muon neutrino flux from helium	28
3.1.5 Superposition: Muon flux from iron	29
3.1.6 Superposition: Helium and proton flux	30
3.2.1 Contribution of individual yields	31
3.2.2 Yields as a function of x	32
3.2.3 Runtime with sliding low-E cutoff	33
3.2.4 Runtime with varying HILOW parameter	34
3.2.5 Yields with forced meson decay	35
3.3.1 Magnetic deviation of muons	37
3.3.2 Lateral Distribution of 1 GeV muons	38
3.3.3 Lateral Distribution of 5 GeV muons	38
3.3.4 Example shower	39
3.3.5 Illustration of shower cone projection	42
3.3.6 Deviation of zenith dependence	43
3.3.7 Illustration of new weighting scheme	43
4.2.1 Pathlength difference of zenith binning	48
4.3.1 LiDO overview	49
4.4.1 Schematic of yield storage structure	50
4.4.2 Example distributions for the oscillation probability weighting scheme	53
5.1.1 GST model tuned to AMS data	56
5.1.2 GST model tuned to BESS data	57
5.1.3 Muon flux with BESS CR and muon data	57
5.2.1 Contribution of UrQMD	58
5.3.1 Muon flux with EPOS and FLUKA	60
5.3.2 Muon flux separated by charge	61
5.3.3 Neutrino flux with EPOS and FLUKA	61
5.3.4 Zenith dependence of Muon flux with FLUKA	62
5.3.5 Zenith dependence of Muon flux with EPOS	62
5.3.6 Muon charge ratios	63

List of Figures

5.4.1 Flux contribution of kaons and pions	65
5.4.2 EPOS/FLUKA discrepancy in muon flux	66
5.4.3 EPOS/FLUKA discrepancy in muon neutrino flux	66
5.4.4 Contribution of unflavored mesons to the muons flux	67
5.4.5 Kaon and pion charge ratios	69
5.4.6 Kaon to pion ratio	69
5.4.7 Muon to electron neutrino ratio	70
5.4.8 ν_μ to $\bar{\nu}_\mu$ ratio	71
5.4.9 ν_e to $\bar{\nu}_e$ ratio	71
5.5.1 Systematic uncertainties	73
5.5.2 Example transfer function	74
5.6.1 Example distribution of opening angle	75
5.6.2 Example production height distribution	76
5.6.3 Average muon production height	77
5.6.4 Average muon neutrino production height	78
5.6.5 Average opening angle of muons	79
5.6.6 Average opening angle of muon neutrinos	80
5.6.7 Average x for vertical and horizontal muons and muon neutrinos	80
5.6.8 Zenith dependence of muon neutrino flux with FLUKA	81
5.6.9 Zenith dependence of muon neutrino flux with EPOS	82
5.7.1 Effect of geomagnetic cutoff on muon neutrino flux	83
5.7.2 Example oscillation probabilities	84
5.7.3 Oscillation probability of electron neutrinos	85
5.7.4 Dependence of oscillation probabilities on production height	86
5.7.5 Muon neutrino oscillation by resulting neutrino flavor	86
5.7.6 Comparison of muon neutrino oscillations with SuperK data	87
A.1 Superposition: Electron neutrino flux from iron	93
A.2 Superposition: Electron neutrino flux from helium	94
A.3 Superposition: Muon flux from helium	95
B.1 Average production height of muons with FLUKA	96
B.2 Average production height of muon neutrinos with FLUKA	97
B.3 Average opening angle of muons with FLUKA	97
B.4 Average opening angle of muon neutrinos with FLUKA	98
C.1 Illustration of the overlap between shower footprint and detector	100

1. Introduction

An impromptu survey among members of the astroparticle physics working group at the RUB found that five out of six theses in the field of astroparticle physics feature the balloon experiments conducted by Viktor Hess prominently in the introduction. In his flights Hess was able to show that the rate of ionizing radiation increased with altitude, which was in contradiction to the predominant view at the time that this radiation originated from the Earth itself as the result of natural radioactivity. While these experiments marked the discovery of Cosmic Rays, Hess was not the only one who contributed to the field. His prominence in the aforementioned survey stands in stark contrast to the relative lack of recognition received by Carl Anderson, who discovered the positron and the muon Cosmic Ray observations and shared a Nobel price with Hess in 1936. Anderson was not mentioned in any of the surveyed theses. Rabi's often quoted "who ordered that?" regarding the discovery of the muon – or rather the discovery that the muon was not the pion predicted by Yukawa – seems just as apt to describe the disproportionate distribution of recognition. Maybe it has something to do with proving people wrong as Hess did as opposed to confirming other people's predictions. Anderson found the positron predicted by Dirac, and the muon was first misidentified as the pion predicted by Yukawa. Rabi became upset about the muon only after the actual pion was discovered. Or maybe it has something to do with the romantic notion of balloon flight, whereas muons are predominantly observed in caverns. Certainly an electroscope in a balloon sounds more exciting than a tank of dry-cleaning fluid in an abandoned mine, which is where solar neutrinos were first observed.



Carl Anderson [1]



Viktor Hess [1]

While redressing the perceived shortcomings in the fame of physicists past would be a worthwhile goal, the expectation for a thesis is still to propel scientific knowledge (however minor) instead of recognition (even when egregiously lacking). As the existence of Cosmic Rays is well established, the interest has shifted towards finding the sources of Cosmic Rays and understanding the processes involved in producing them. The ionizing radiation found by Hess is for the most part the result of the charged particles in Cosmic Rays, which are not well suited to resolve individual sources. The electrically neutral components constitute both the oldest (in the case of photons) and the newest (in the case of neutrinos) avenue of observation in astrophysics. Experiments have also progressed from measuring

1. Introduction

simple rates to more detailed observations of individual particles and their interaction products. However, as experiments grow more complex, so do the signatures of the observed events, which creates an increasing need for simulation in the design of the experiments and the analysis of experimental data.

For optical observatories, pollution from ambient light sources is a problem. This issue is even more severe for neutrinos as they are produced both in the astrophysical source candidates and inside the Earth's atmosphere and also by the very same hadronic processes. This leads to very low signal-to-noise ratios. The situation is further complicated by the fact that the direction of a neutrino can be resolved, but not the distance at which it originated. As the universe is more transparent for neutrinos than it is for photons, this is also a chance to study sources that would otherwise be impossible to observe, provided one can find them in the noise.

As the experimental signatures of individual atmospheric and astrophysical neutrinos are virtually identical, they can only be distinguished by their collective properties, in particular the shape of their energy and zenith angle distribution. In order to establish the astrophysical origin of a neutrino, it is necessary to determine the spectrum of atmospheric neutrinos both experimentally and through simulation. This work is focused solely on the latter. It builds on previous works, in particular by Fedynitch et al.[2]. The goal is to determine the flux of atmospheric muons, muon neutrinos and electron neutrinos down to total energies of 1 GeV, determine the uncertainties of the resulting spectra, and compare the results to experimental data and other simulations. Towards this goal, the interaction of Cosmic Rays in the atmosphere will be simulated with Monte Carlo methods using the propagation software CORSIKA and the interaction models EPOS and FLUKA included therein. In platonic terms, this work is concerned solely with sublunar physics, the universe beyond the Moon's orbit only serves to provide the input parameters to the calculations. Although the basic hadronic processes studied in this work are the same as those that might occur in astrophysical neutrino sources, the dense environment of the Earth's atmosphere gives rise to a range of complications that can be safely ignored pretty much everywhere else in the universe. At low energies the effects of the Earth's magnetic field, neutrino oscillations, and the geometry of the observation level need to be considered as well.

This work is structured as follows: Chapter 2 covers the basic concepts and physical processes involved in Cosmic Ray interactions and air showers, as well as the software used to simulate them. Chapter 3 contains the technical details of the simulation as well as a description of the phenomena that can be exploited to reduce the CPU needs of the simulation. The resulting spectra and distributions will be presented in detail in Chapter 4.

2. Basic Concepts

2.1. Cosmic Rays

Earth is exposed to a constant stream of charged particles – mostly protons – which are called Cosmic Rays (CR) mainly for historical reasons (see above). Cosmic Matter would be the more appropriate term. The term CR particles will often be used in the following to emphasize the particle nature of CRs, which is most relevant to this work. Apart from protons, CRs comprise nuclei of elements with charge numbers up to $Z = 26$ (iron), depending on the definition the small number of electrons or positrons from astrophysical sources is also counted among CRs. The exact sources of CRs are yet to be determined. While the nuclei of heavier elements would have had to be produced in stars that subsequently exploded, protons have been around since before the formation of stars. Because CR particles are deflected by magnetic fields on their way to Earth and their flux is mostly isotropic once they arrive, they do not point back to their source as photons or neutrinos would. As this work focuses on the secondary particles produced in hadronic CR interactions inside Earth's atmosphere, the term *primary CRs* is generally used to refer only to the hadronic particles among CRs. Electrons, photons or neutrinos from extraterrestrial sources are not considered in this work.

For the purpose of this work, the only relevant effects occur within a 500 km radius around the Earth, where the CR flux is mostly isotropic, so a detailed description of the acceleration process of CRs is omitted here. The spectral shape and composition of the CRs as measured at Earth are of utmost importance however. The all-particle CR spectrum can be described as a broken power-law in energy $E^{-\gamma}$ with breaks at $\sim 10^6$ GeV and $\sim 10^9$ GeV, called the knee and the ankle. Up to the knee, the all-particle spectrum follows a power-law with index $\gamma \approx 2.7$, which steepens to a $\gamma \approx 3$ spectrum from 10⁶ GeV to 10⁹ GeV [3]. Above the knee, the spectrum flattens again, before dropping off exponentially around $\sim 10^{11}$ GeV. These breaks in the all-particle spectrum can be explained by assuming that there are different classes of CR sources that accelerate particles up to a maximum rigidity. For different nuclei, this translates to different maximum energies for the same class of sources. Fermi processes generally lead to particle spectra that follow a power-law in momentum, often with an exponential cutoff related to the limited size of the acceleration-region [4]:

$$\Phi(E_{\text{CR}}) = a_Z (E_{\text{CR}})^{-\alpha} \exp\left(\frac{-E_{\text{CR}}}{E_{\text{cut}} Z}\right), \quad (2.1)$$

where Z is the charge number and E_{cut} represents the cutoff energy. Breaks in the spectrum can indicate the transition between two classes of CR sources with different

2. Basic Concepts

maximum rigidity [4]. This power-law behavior is considered evidence that the diffusive shock acceleration is responsible for the acceleration CRs [5]. These stochastic processes require acceleration regions with strong magnetic fields (and field inhomogeneities) and possibly shocks to accelerate particles, but the acceleration regions are not necessarily the original production site of the CR particles.

The spectrum and composition of CR are generally measured in two different ways: Satellite based experiments and balloon-borne experiments. Balloon-borne experiments need to deal with the attenuation of the CR flux inside the atmosphere, although most of the atmospheric overburden has been cleared once the altitude reaches 30 km. At an altitude of about 36 km the flux of CR nuclei is about 10 % smaller than at the top of the atmosphere, due to CR interactions with the particles in the atmosphere [6]. Both types of experiments face restrictions in terms of weight and size, which limit the calorimetric energy resolution of direct observations. Higher energy CRs can be observed indirectly through the showers created by their interaction with particles in the Earth's atmosphere, see below. However, direct observations with spectrometers are necessary to determine the CR composition with high accuracy.

For indirect measurements, the energy of a CR particle has to be estimated from its secondary particles, which limits the energy resolution and can lead to systematic errors in the energy reconstruction. However, if certain characteristic features in the energy spectrum can be observed, data from different experiments can be cross-calibrated by shifting the energy of observations from different experiments up or down relative to each other. This has been done by e.g. Gaisser et al.[7], who also fitted a model with several populations of particles to the resulting spectrum. This model is explained in more detail in Section 2.1.2.

For inclusive fluxes of secondaries, the detailed composition of the cosmic rays is less important, the impact on the charge of secondary particles can be described sufficiently if the ratio of protons to neutrons in the CR flux is known, see Section 3.1. However, the influence of Earth's magnetic field on the trajectories of CRs can lead to a rigidity dependent cutoff that varies between 0.5 GV and 60 GV, depending on the position on the Earth, see Section 3.3.1.

2.1.1. CR experiments

In this section some of the CR experiment will be described in more detail. The CR spectra that have been obtained with the CREAM and PAMELA instruments are crucial for the CR model by Gaisser et al., the data from BESS and AMS will be used in complementary fashion in this work. Both CREAM and BESS are balloon-borne instruments. Because they both underwent upgrades between subsequent flights, only the configuration that took most of the data used in this work will be described.

During its second flight over Antarctica, CREAM measured the spectra of primary CR nuclei with Z ranging from 6 to 26 [8]. This includes the spectra of carbon, nitrogen, oxygen, neon, magnesium, silicon, and iron. The energy range varies for different elements, it covers roughly a few tens of GeV/n to a few TeV/n. At the bottom of the instrument is a sampling imaging colorimeter that consists of 20 tungsten plates

2.1. Cosmic Rays

alternating with layers of scintillating fiber ribbons. The plates measure $0.5\text{ m} \times 0.5\text{ m}$, while the ribbons are 0.5 m long and 1 cm wide. The ribbons are arranged so that the direction of the fibers is orthogonal in neighboring layers, in order to allow imaging the development of showers in the calorimeter in 3 dimensions. Atop the calorimeter sits a carbon target roughly half the interaction length in thickness. In order to pass during reconstruction, particles that shower in the detector need to pass through a pixelated silicon charge detector, consisting of two layers with 156 silicon sensors each, that sits above the carbon target. At the top end of the instrument is a timing-charge detector that consists of two orthogonal layers of plastic scintillator material and covers an area of $1.2\text{ m} \times 1.2\text{ m}$. It can determine a particle's charge with a resolution of $\leq 0.35e$ and it can also be used to identify CR particles that fail the calorimeter trigger condition, i.e. low-energy particles. During previous flights CREAM also measured the CR proton and helium spectra [9].

The BESS-TeV spectrometer was flown over Lynn Lake in Canada. Compared to previous flights of BESS, the BESS-TeV instrument was upgraded to increase the energy range covered [10]. BESS main feature is its cylindrical superconducting magnet (diameter 1 m), that creates a uniform magnetic field of 1 T in its center. The trajectory of a particle is measured by a central jet-type drift chamber, two inner and two outer drift chambers. The trajectory of the particle is reconstructed from 52 points, each measured with a resolution of 1 cm . In order to determine the particle's velocity and energy, the outermost layer of the detector consists of time-of-flight hodoscopes. The BESS-TeV spectrometer was operated at an altitude of 37 km where the residual atmosphere was 4.8 g/cm^2 . During the flight the spectra of CR protons and helium nuclei was measured in a range from 1 GeV to 540 GeV and 1 GeV/n to 250 GeV/n respectively. Observations on the ground were carried out in Tsukuba, Japan at an altitude of 30 m above sea level with an atmospheric overburden of 1032.2 g/cm^2 . While on the ground the flux of atmospheric muons was observed in the range from 0.6 GeV to 400 GeV.

The apparatus of the PAMELA experiment is installed on a Russian satellite in an elliptical orbit around Earth, with an altitude varying between 350 km to 600 km [11]. Its main components include a magnetic spectrometer over electromagnetic calorimeter, separated by layers of a time of flight and an anti-coincidence system. The magnetic spectrometer consists of 6 planes of silicon detectors around a permanent magnet of 0.43 T in strength. It is used to determine the charge and momentum of passing charged particles. Below the spectrometer an electromagnetic calorimeter is mounted to measure the energy of incident electrons and to discriminate between electromagnetic and hadronic showers. Layers of plastic scintillators below and above the spectrometer form a time-of-flight system and the main trigger. The charge of traversing particles can be determined by measuring the energy loss of particles in the scintillator of the time-of-flight system and the silicon layers of the spectrometer. The PAMELA experiment has measured the fluxes of CR protons and helium nuclei in the range from 1 GeV to 1.2 TeV and 1 GeV/n to 600 GeV/n respectively [12], as well as the fluxes of CR boron and carbon in the range from 0.44 GeV/n to 129 GeV/n in kinetic energy [13].

The apparatus of the AMS experiment is installed on the ISS, orbiting Earth at an altitude of about 400 km. Its central feature is a massive cylindrical permanent magnet

2. Basic Concepts

with a mass of about 1200 kg that produces a magnetic field of 0.14 T. The central silicon tracker consists of 9 layers of silicon strips that record the particles position and infer the particles rigidity from the bending of its trajectory. 6 of the layers are housed inside the bore of the magnet, with 2 layers above and one layer below the magnet. The maximum rigidity that can be resolved over all layers is 3.2 TV. Each layer measures the charge of the particle independently, leading to a charge resolution of 5 % for protons and 7 % for helium nuclei. Before its launch, AMS was calibrated at the CERN SPS using 180 GeV and 400 GeV proton beams, as well as beams of positrons, electrons and pions. In order to pass the event selection, a particle needs to pass through 3 of the 4 layers of time-of-flight scintillation counters (2 layers above and 2 layers below the tracker) and produce no signal in the anti-coincidence counters. AMS measured the spectrum of Cr protons in the energy range from 1 GeV to 1.8 TeV divided into 72 bins, with bin widths chosen according to the energy resolution [14]. The spectrum of CR helium nuclei from 3.8 GeV to 6 TeV in 68 bins corresponding to the energy resolution [15].

While the CR flux at energies probed by indirect measurements provide insight into the propagation of CRs, they do not contribute much to the lepton fluxes in the energy range studied in this work (see Section 3.2.1). They do however offer an opportunity to test the theoretical tools for the description of air showers. In particular, they allow testing hadronic interaction models in regions that cannot be effectively studied in accelerator experiments. The Pierre-Auger-Observatory located in Argentina near the Andes was designed to observe the CR flux above 10^9 GeV. It has two main components: A surface detector array that instruments an area of about 3000 km^2 with 1600 water Cherenkov detector and a fluorescence detector that consist of 27 optical telescopes, distributed across 5 buildings. These buildings are positioned on the outer edges of the surface detector, with the telescopes pointing inward. The surface detector samples the electrons, photons and muons produced in air showers while the optical telescopes detect the fluorescence emission of excited nitrogen molecules in the atmosphere, as well as the Cherenkov light emitted by charged particles in the shower. The spectrum of CRs above 3×10^9 GeV was measured using data from the surface detector, this measurement was extended to 1×10^9 GeV by using hybrid events, i.e. those that were observed by the fluorescence detector and also triggered at least on station of the surface array [16]. Measurements of the muon content of air showers were used to test the EPOS and QGSJET models [17].

2.1.2. Primary CR flux models

Fig. 2.1.1 shows the all-particle CR spectrum as measured by several different experiments. In this plot and for subsequent use with CORSIKA all CR energies have been converted to total energy. For the purposes of weighting simulation data, the energy range covered by a single experiment is often not sufficient and data from different experiments need to be combined. In addition to that, it is often preferable to use a continuous parametric model instead of discrete data points. The data collected by CREAM and PAMELA suggest that the spectra of individual particles are not well described by a single power-law [12] and can be harder than the all-particle spectrum

[8]. This is reflected in recent models that allow several populations with different a power-law index for every group of CR nuclei.

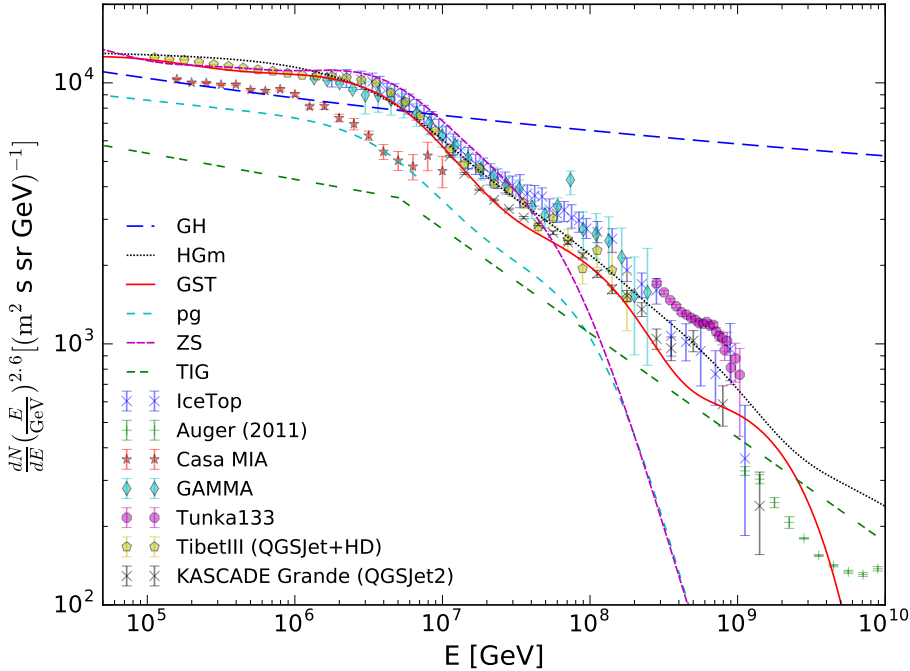


Figure 2.1.1.: Primary CR all-particle spectra: Data from IceTop [18], Auger (2011) [16], Casa MIA [19], GAMMA [20], Tunka133 [21], TibetIII (QGSJet+HD) [22], KASCADE Grande (QGSJet2) [23], all data taken from [24]. The models shown are GH [25], HGm (also called H3a) [4], GST [7], pg [26], ZS [27] and TIG [28].

Several parametric models have been used in the past. The model developed by Gaisser in [4] assumes three populations with five different mass groups of nuclei: H, He, CNO, MgAlSi and Fe. Each population shares a common rigidity-based cutoff E_{cut} , and individual normalization parameters for each mass group a_Z :

$$\Phi_Z(E_{\text{CR}}) = \sum_{i=1}^3 a_{Z,i} (E_{\text{CR}})^{-\alpha_{Z,i}} \exp\left(\frac{-E_{\text{CR}}}{R_{\text{cut},i} Z}\right). \quad (2.2)$$

The spectral index $\alpha_{Z,i}$ could be left to vary, but ends up being the same for each mass group in [4]. This model used to be the default CR flux model in IceCube, where it is referred to as H3a, in Fig. 2.1.1 it is labeled HGm. However, it has been replaced by an improved model by Gaisser et al. [7] called GST, which follows the same paradigm, but uses a more sophisticated approach to determine the parameters in each population and mass group. In particular, the cutoff rigidities in the GST model are much lower than in the H3a model: 120 TV, 4 PV, and 1.3 EV for GST compared to 4 PV, 30 PV, and 2 EV for H3a. This leaves room for a potential fourth population in GST. GST also splits the CNO group into separate contributions from C and O. However, because

2. Basic Concepts

those two elements are fitted with the same spectral shape in each population, they can be recombined into a single group for the sake of comparison. Both models share the property that individual spectra within a generation can be much harder ($\alpha \approx 1.4 - 1.6$) than the all-particle spectrum ($\gamma \approx 2.7$). However, they are meant as high-energy models: H3a is only valid above 10 TeV, while GST can be used down to energies above 1 TeV.

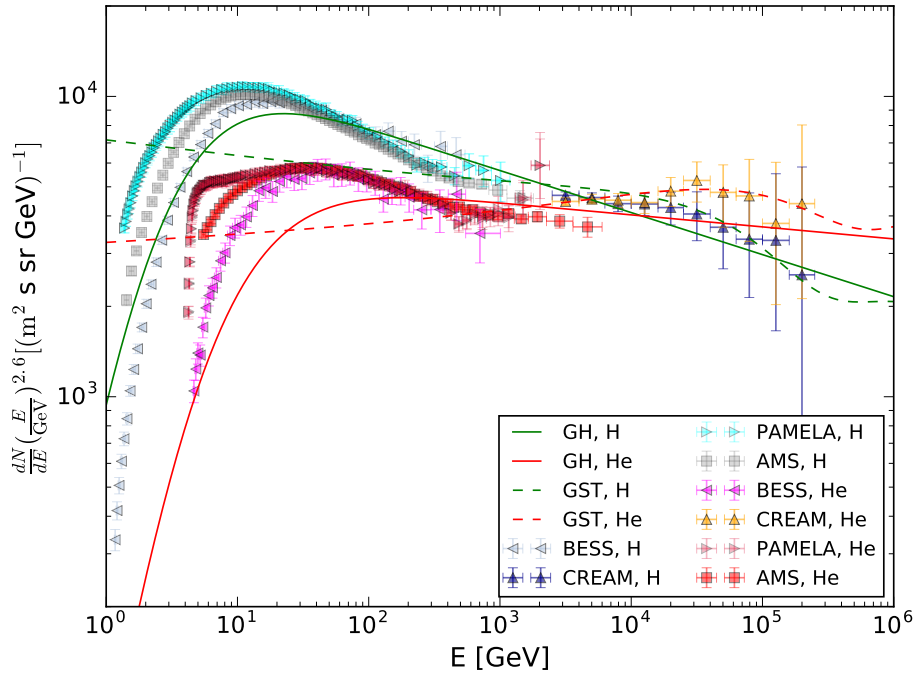


Figure 2.1.2.: Individual CR particle spectra for H and He according to the GST [7] and GH [25] models. Data taken from the Cosmic Ray Database [29]. Individual references: BESS [30], PAMELA [12], CREAM [9], and AMS [14, 15].

To compensate the limited energy range of H3a, Fedynitch et al. [2] combined the model with an earlier model by Gaisser and Honda [25], called GH throughout this work. As the intended CR energy range in this work is 5 GeV to 100 TeV, it would be possible to use GH on its own, because it agrees with the observed all-particle CR spectrum up to 1 PeV. GH uses a different fit-model to describe the individual particle spectra, because at energies below 50 GeV the solar modulation causes particles to deviate from a pure power-law behavior [31]. The mass groups are the same as in the other models; however, there is only one population per group described by

$$\Phi_Z(E_{\text{CR}}) = K \cdot \left(E_{\text{CR}} + b \exp(-c\sqrt{E_{\text{CR}}}) \right)^{-\alpha} \quad (2.3)$$

with the parameters K , b , c , and α fitted for each mass group. The individual spectra for Helium and protons are shown in Fig. 2.1.2, compared to the GH and GST model.

H3a is omitted here, because it is not supposed to cover the energy range below 10 TeV. GST shows slightly better agreement with the CREAM data than GH, but does not match the shape of the CR spectrum below 100 GeV. It would be possible to combine GST and GH in a similar fashion as used previously. On the other hand, it might be more interesting to combine GST with recent observations by AMS, as there appears to be room in GST for an additional population below 1 TeV.

There are several other CR flux models available, which will sometimes be used for comparison or to estimate the range of possible values for the CR flux, although the details of how the CR flux is modeled are of no consequence for this particular use. These models include the Zatsepin-Sokolskaya (*ZS*) model [27] and the polygonato (*pg*) model [26], which have been used in the past, but do not describe the spectrum above 10^8 GeV very well. The TIG model defined in [28] has been used in other simulations and is included here as a base of comparison. It follows a simple broken power-law; however it is a pure proton spectrum, and therefore not easily comparable to CR observations.

2.2. Extended Air Showers

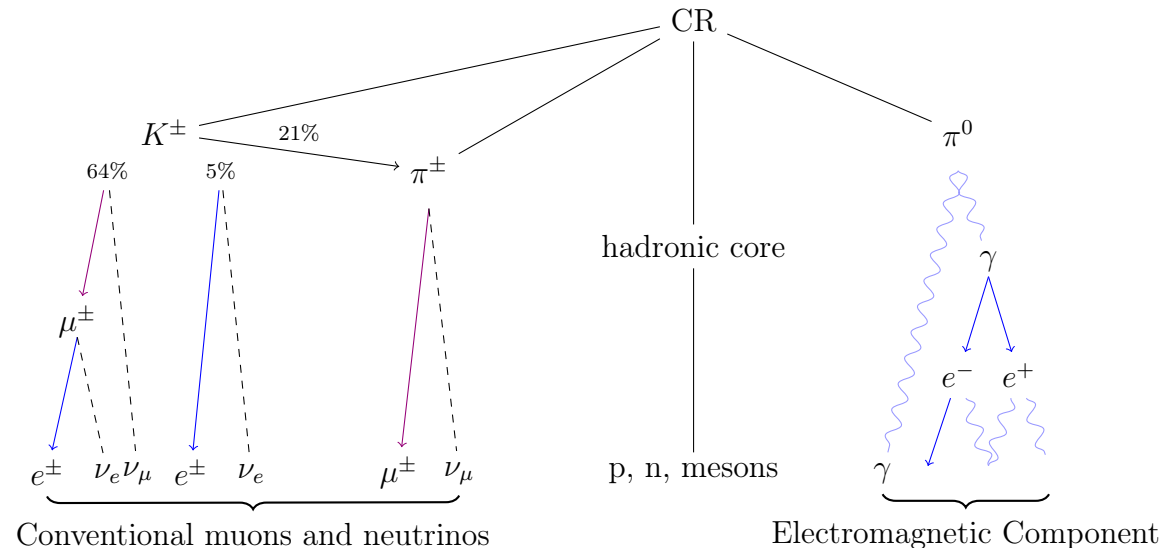


Figure 2.2.1.: Schematic depiction of an air shower.

When CR nuclei enter Earth's atmosphere, they will most likely interact with the nuclei of air molecules, i.e. oxygen or nitrogen nuclei. The particles produced in the first interaction travel on, and in turn have chance to either decay or interact. The products of these decays and interactions continue this process until they either reach the surface, or lose so much energy that they cannot produce any more particles. This cascade of interactions and decays distributes the energy of the incoming CR nucleus among a large number of secondary particles, traveling toward Earth in a cone around the axis defined by the trajectory of the initial CR with an opening angle $\propto \frac{1}{\gamma}$. This section describes

2. Basic Concepts

the most relevant particles, production processes and decay channels encountered in an air shower. A schematic depiction of the particles in an air shower is shown in Fig. 2.2.1.

Hadronic interactions at high energies generally involve only one nucleon from each nucleus. Because most CR nuclei are protons to begin with, the most fundamental interaction is inelastic proton-proton scattering. If the energy of the incoming CR proton exceeds the threshold energy of $E_{\text{thr}} = 1.22 \text{ GeV}$, a pion can be produced via the production of a Δ -resonance and its subsequent decay:

$$pp \rightarrow p \Delta^+ \rightarrow \begin{cases} n \pi^+ \\ p \pi^0 \end{cases} \quad \text{or} \quad pn \rightarrow p \Delta^0 \rightarrow \begin{cases} n \pi^0 \\ p \pi^- \end{cases} .$$

One important process at a somewhat higher energy is Λ -associated kaon production

$$pp \rightarrow p \Lambda K^+,$$

because there exists no corresponding production channel for K^- . Quarks are produced in pairs and the $s\bar{s}$ pair has to be distributed so that the s quark becomes part of the baryon, which means that the \bar{s} quark has to become part of the meson, which is only possible for K^+ . This asymmetry in the charge of produced kaons translates to the muons from kaon decay. The charge ratio of muons can be measured and used to probe the differing contributions from kaons and pions to the muon flux. This provides a handle on effects that cannot be observed directly due to the short life time of mesons.

At higher proton energies increasing numbers of different hadrons are produced, however most of the heavier baryons and mesons decay almost immediately. For relatively long-lived pions and kaons (with lifetimes on the order of 10^{-8} s) there is a chance to interact with other nuclei of the atmosphere before they decay, in this case they do not contribute to the flux of leptons. The decay of pions and kaons generally produces a muon and a muon neutrino:

$$\begin{array}{ll} \pi^+ \rightarrow \mu^+ \nu_\mu & \pi^- \rightarrow \mu^- \bar{\nu}_\mu \\ K^+ \rightarrow \mu^+ \nu_\mu & K^- \rightarrow \mu^- \bar{\nu}_\mu \\ \mu^+ \rightarrow e^+ \nu_e \bar{\nu}_\mu & \mu^- \rightarrow e^- \bar{\nu}_e \nu_\mu. \end{array}$$

The muons can decay into electrons and neutrinos, but due to the Lorentz boost most muons above $\sim 100 \text{ GeV}$ reach the surface of the Earth. The two-body decays of the mesons would occur with the leptons traveling in opposite direction in the rest frame, however due to the Lorentz boost of the mesons the secondary particles are emitted in a cone around the axis of the original CR particle. The particles with the highest energy inside the shower are closest to the core of the shower, whereas the outer part of the shower cone is generally populated by particles with lower energies. The contribution from kaons and pions to the resulting flux of muons and neutrinos is called the conventional flux.

In addition to kaons and pions, heavier mesons can be produced as well, albeit at a lower rate. All of the relevant heavier mesons have lifetimes below 10^{-10} s and therefore

decay almost immediately, without any chance to interact with other particles in the atmosphere. Therefore the contribution from those particles is called the prompt flux. There are two different classes of mesons that contribute to the prompt flux. One class consists of charmed mesons. Here charged D^\pm mesons are most relevant. The other class consists of neutral mesons whose quantum numbers charm C and strangeness S both equal $S = C = 0$, which are therefore called unflavored mesons. In the context of air showers the most relevant unflavored mesons are η , ρ^0 and ω . Strictly speaking pions are also unflavored, but as their role is central to the conventional flux they are considered separately. Unflavored mesons most often decay into pions, but they do have small ($\mathcal{O}(10^{-4})$) branching ratios to decay directly into $\mu^+ \mu^-$ -pairs. D^\pm mesons on the other hand have much larger branching ratios ($\mathcal{O}(10^{-1})$) to decay into μ^\pm or e^\pm . These decays generally include a corresponding neutrino, and in most cases at least one more meson. As unflavored mesons are more common than D^\pm mesons, their contributions to muon production are comparable, but only D^\pm mesons contribute directly to the production of neutrinos. An overview of the lifetimes, branching ratios and decay modes of the particles that contribute to the conventional and prompt fluxes is given in Table 2.1.

Apart from the hadronic interactions and weak decays described so far, there is also a contribution due to electromagnetic interaction. Gamma rays from the decay of π^0 can produce pairs of leptons, both $e^+ e^-$ and $\mu^+ \mu^-$, although the latter process occurs far less frequently. Due to their lower mass e^+ and e^- produced in pair-production or in the decay of muons are more likely to undergo electromagnetic scattering with atoms in the atmosphere or lose energy through radiative processes than other particles in the shower. The e^+ can also annihilate with the e^- in the atmosphere. In both cases additional photons are produced that often still carry sufficient energy to produce further $e^+ e^-$ pairs, which in turn can produce further photons. These photons and electrons are called the electromagnetic component of the cascade. The cycle of pair-production and scattering/annihilation can be repeated several times, whereas mesons are produced in strong interactions and only contribute leptons to the shower if they decay. This causes the electromagnetic cascade to distribute the energy over a larger number of particles, with a lower Lorentz boost factor. Due to the tendency of particles with lower Lorentz boost to deviate further from the original CR axis, air showers have a core which is mostly hadronic and become increasingly more leptonic toward the outer part of the shower cone.

2. Basic Concepts

Particle	Mean life τ [s]	Decay modes	BR
π^0	8.4×10^{-17}	2γ	98.8 %
π^+	2.6×10^{-8}	$\mu^+ \nu_\mu$	99.9 %
π^-	2.6×10^{-8}	$\mu^- \bar{\nu}_\mu$	99.9 %
K_S^0	0.9×10^{-10}	$2\pi^0$	30.69 %
		$\pi^+ \pi^-$	69.2 %
K_L^0	5.1×10^{-8}	$3\pi^0$	19.52 %
		$\pi^+ \pi^- \pi^0$	12.54 %
		$\pi^\pm e^\mp \nu_e$	40.55 %
		$\pi^\pm \mu^\mp \nu_\mu$	27.04 %
K^+	1.2×10^{-8}	$\mu^+ \nu_\mu$	63.56 %
		$\pi^+ \pi^0$	20.67 %
		$\pi^0 e^+ \nu_e$	5.07 %
K^-	1.2×10^{-8}	$\mu^- \bar{\nu}_\mu$	63.56 %
		$\pi^- \pi^0$	20.67 %
		$\pi^0 e^- \bar{\nu}_e$	5.07 %
η	5.0×10^{-19}	2γ	39.41 %
		$3\pi^0$	32.68 %
		$\pi^+ \pi^- \pi^0$	22.92 %
		$\mu^+ \mu^- \gamma$	3.1×10^{-4}
ρ^0	4.5×10^{-24}	$\pi^+ \pi^-$	$\sim 100 \%$
		$\mu^+ \mu^-$	4.55×10^{-5}
ω	7.8×10^{-23}	$\pi^+ \pi^- \pi^0$	89.2 %
		$\mu^+ \mu^- (\pi^0)$	2.2×10^{-4}
D^+	1.0×10^{-12}	$e^+ \nu_e$ semileptonic	16.07 %
		$\mu^+ \nu_\mu$ anything	17.6 %
D^-	1.0×10^{-12}	$e^- \bar{\nu}_e$ semileptonic	16.07 %
		$\mu^- \bar{\nu}_\mu$ anything	17.6 %

Table 2.1.: Relevant particles and their most important decay modes in extended air showers, all data taken from PDG [32]

2.3. Atmospheric lepton measurements

Leptons from air showers are plentiful, but only muons and electrons are easily detectable. However, electrons lose energy quickly and often catastrophically so that an atmospheric electron spectrum at the surface level is not very meaningful. Neutrinos interact too infrequently, rendering their detection more difficult. Historically, cloud chambers have been used to prove the existence of muons from CRs, although they have since been replaced with wire chambers. Scintillators can be used as well, although all these detector types are generally so small that only few particles from a given shower can be observed once they reach the ground. For the identification of muon charge a magnetic field needs to be present as well. In order to observe a shower in its entirety, Cherenkov radiation from the charged particles in the shower needs to be detected with (air) Cherenkov telescopes.

Due to their larger mass, atmospheric muons lose energy through radiation at significantly lower rates than electrons, and as they are not subject to hadronic interactions they can penetrate a large amount of material. For this reason atmospheric muons constitute a significant portion of the background for a number of particle physics experiments. It is perhaps not surprising that a large amount of the data on atmospheric muons that will be used throughout this work has been collected by experiments designed with a different main goal. Three of those experiments will be described in more detail in the following.

The balloon-borne BESS detector has been developed to measure the spectra of CR protons and helium as well as their corresponding anti-particles, however it has also been used to measure the flux of atmospheric muons at ground level [30].

The L3 detector on the Large Electron-Positron Collider (LEP) consisted of several subdetectors arranged cylindrically around the interaction point of the particle beams. Closest to the interaction point were the silicon strip microvertex detector and the time expansion chamber, used for tracking the vertex of the interaction and the trajectory of the particles produced in the collision. Farther outwards were the electromagnetic and hadronic calorimeters, which were separated by scintillation counters. The outermost layer of the detector consisted of muon chambers [33]. The entire detector was housed inside a magnet, which at that time was the largest magnet in the world. The magnet is currently being used for the ALICE experiment on the Large Hadron Collider. During normal operation the scintillation counters would be used to veto atmospheric muons, however for the L3+C experiment the L3 detector at CERN was used to measure the spectrum of atmospheric muons, with the LEP particle beam turned off [34].

The MINOS experiment was designed to measure neutrino oscillations, it consists of two detectors operating on a beamline produced at Fermilab. The near detector is located close to the starting point of the beamline, while the far detector is located in the Soudan mine in Minnesota, about 700 km to the north. Both detectors are sampling calorimeters made from alternating layers of magnetized steel and a plastic scintillator. The larger, far detector was completed in 2003 and used to measure the flux and charge ratios of atmospheric muons before the completion of the near detector [35].

The main difficulty in detecting neutrinos is their very low probability to interact

2. Basic Concepts

and only the products of their interactions can be detected. So the first challenge is to have a sufficiently large and massive target for neutrinos to interact with and then instrumenting said target. Historically this problem has been solved by choosing a target in which neutrinos create long-lived products that can easily be separated from the target material and then counted. In the Homestake experiment, located in the eponymous Homestake mine, a large tank of dry-cleaning fluid (perchloroethylene C_2Cl_4 or PERC for short) was used to detect electron neutrinos from the Sun. Neutrinos would interact with the ^{37}Cl atoms in the fluid and turn them into ^{37}Ar atoms, which would break the molecular bond in the PERC-molecules, so the gaseous and radioactive argon atoms could be separated and their decay counted using a Geiger-counter. At the depth of the Homestake experiment (about 4000 m water equivalent) the expected muon flux was $6 \times 10^{-9} (\text{cm}^2 \text{ssr})^{-1}$ which lead to an expected rate of ^{37}Ar production due to muon-nucleon interaction of 0.14 /day in 380 m^3 of PERC with an expected rate of 4 /day to 11 /day produced from solar neutrinos [36].

While the experiment was successful in the first detection of solar neutrinos, this approach does not allow to determine the energy of the neutrinos, so more modern experiments rely on different methods. The most popular approach relies on Cherenkov radiation in either water or ice, as those materials are cheap and readily available. The photons emitted by the products of the neutrino interaction – either a muon track or hadronic cascade – are detected by photo-multipliers either suspended inside the target material (as is the case in ANTARES or IceCube) or built into the wall of the container for the target material (in the case of SuperKamiokande). As the Cherenkov radiation is not produced by the neutrino itself, but rather by the products of neutrino interactions, all these experiments need to find ways to separate the neutrino signal from the background of atmospheric muons, and in case only a specific sort of neutrinos (e.g. astrophysical or prompt) is of interest, also from the atmospheric neutrino background. In the following IceCube and its low-energy extensions will be discussed in more detail.

2.3.1. IceCube

IceCube is a Cherenkov detector located at the geographic south pole. A schematic depiction is shown in Fig. 2.3.1. It instruments a km^3 volume of antarctic ice about 1 km below the surface with 5160 digital optical modules (DOMs) evenly spread across 86 strings. On each string the DOMs are spaced 15 m apart, the separation between the strings is about 125 m. six of these strings are DeepCore strings with a tighter DOM spacing. The DOMs used in DeepCore are more efficient and they are about 5 times as densely spaced as the rest of IceCube [38]. The purpose of DeepCore was to reduce the detection threshold of IceCube from $\sim 100 \text{ GeV}$ to $\sim 10 \text{ GeV}$ neutrino energy. This opens the possibility to study neutrino oscillations with IceCube, as the survival probability of muon neutrinos traveling through the Earth has a minimum at $\sim 25 \text{ GeV}$.

Being a Cherenkov detector IceCube does not detect neutrinos directly, only the light emitted by particles created by neutrino interactions in the surrounding ice. For muon neutrinos that undergo a charged current interaction the product is a muon. This muon travels at a velocity greater than the phase velocity of light in ice. As it is charged it

2.3. Atmospheric lepton measurements

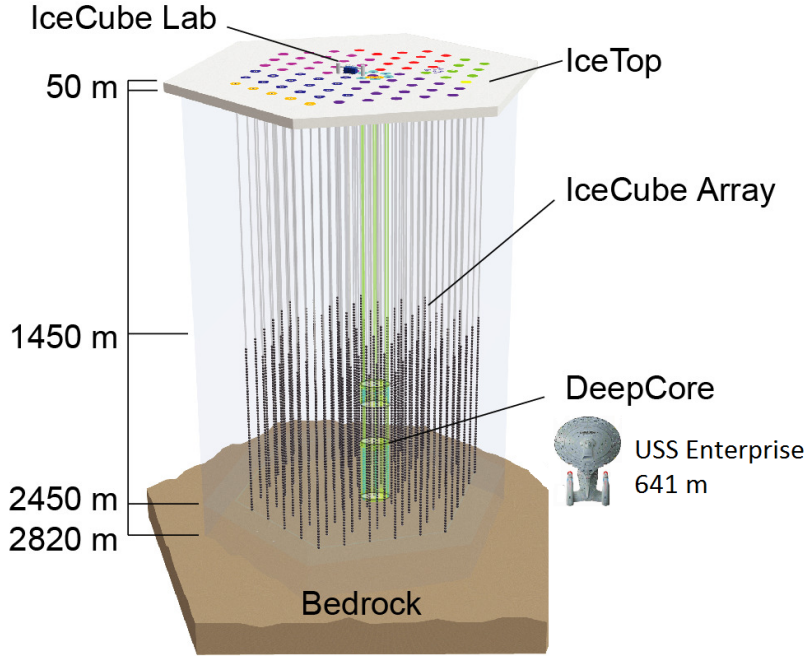


Figure 2.3.1.: Schematic depiction of IceCube and DeepCore adapted from [37].

polarizes the atoms along its trajectory. The energy contained in the polarization is then radiated as a coherent shock-wave in the wake of the muon. As the muon loses energy at a rate of ~ 1 GeV/m it leaves a track of Cherenkov light in the detector. At very high energies the muon track is no longer contained by the instrumented volume, which limits the maximum energy that can be resolved. At low energies the track becomes too faint to be detected. The lower threshold of detection can be improved by a more densely instrumented volume, as has been done with DeepCore and proposed for PINGU [39]. In order to improve the sensitivity to the events with the highest energy, a larger instrumented volume is necessary, as is planned for the next generation of IceCube. For electron or tau neutrinos, or for neutral current interactions of muon neutrinos, instead of a track there is a cascade of light produced in the detector. While the energy resolution for these events is better than it is for muon tracks, the direction can only be resolved to $\approx 15^\circ$.

In either case, there is a large background of atmospheric muons that needs to be suppressed. This can be done by using the Earth as a shield and selecting only muon tracks that point up through the Earth, however these only constitute about half of the muon neutrino events and selecting only up-going tracks effectively halves the field of view. A better way to suppress the atmospheric muon background is to use the outer layer of the detector as a veto and only select particles that interacted within the detector volume, which has been done in the HESE (high energy starting events) analysis [40]. Atmospheric neutrinos play a dual role: They constitute a background in the search for extraterrestrial neutrinos, but they can also be considered a signal, e.g. in studying neutrino oscillations or the production of charmed particles in the forward scattering

2. Basic Concepts

region, which is difficult to probe with storage ring type accelerators such as the LHC.

In order to ensure the optimal suppression of various backgrounds, it is necessary to ensure that the theoretical description agrees with the experimental findings. As the signature of neutrinos in the detector is the same for atmospheric and astrophysical neutrinos, they can only be distinguished by the spectral shape of their energy distribution or zenith distribution. The spectrum of atmospheric neutrinos has been studied with IceCube [41], and generally seems to agree with the simulation performed by [2]. For future studies with PINGU, the simulation needs to be extended toward lower energies. This is the goal of this work.

2.4. Atmospheric lepton fluxes

In cases where only the average flux of particles that arrive at the Earth's surface is of interest – for example because the shower cannot be resolved in its entirety – the longitudinal development of the shower can be neglected. There have been several analytical approaches to calculating the flux of muons or neutrinos from air showers, a few of these will be discussed here to explain some of the phenomenological qualities of the shower. One of the commonly used ones is the cascade equation, which describes the flux of leptons from the flux of primary CRs as a system of coupled integro-differential equations that follow the general shape of

$$\frac{dN}{dt} = -\frac{N}{\lambda_{\text{dec}}} - \frac{N}{\lambda_{\text{int}}} + S, \quad (2.4)$$

where N is the number of particles, or rather the flux, but the factors dE and dA are generally omitted. The slant depth t corresponds to the distance a particle travels in units of the number of particles (of the atmosphere) that it passes on its way. $\lambda_{\text{dec}} = \gamma\beta\tau c$ is the decay length, i.e. the distance a particle needs to traverse before its decay time τ has elapsed and the interaction length λ_{int} which corresponds to the average distance a particle travels before interacting with another particle:

$$\lambda_{\text{int}} = \frac{\rho(h)}{\sum_A \sigma_{jA} n_A(h)} \quad (2.5)$$

where ρ corresponds to the atmospheric density at height h and σ_{jA} to the cross-section between a projectile j and air nuclei of mass number A and $n_A(h)$ represents the number density of those nuclei.

There are three generations of particles in the cascade equation: the first generation corresponds to the flux of primary CR nucleons, the second describes the flux of mesons produced in interactions of the CR particles with air molecules and the third generation describes the flux of leptons produced in the decay of those mesons. In this fashion one of the loss terms in one generation provides the source term of the next generation. In the case of primary nucleons there is no decay. Primary neutrons may be considered separately, even when not bound in nuclei, their mean lifetime is so large that the length of their trajectory through the atmosphere is very small compared to their

2.4. Atmospheric lepton fluxes

interaction length. The primary CR interaction produce mesons according to the source term

$$S(NA \rightarrow m_K) = \int_E^\infty dE' \frac{\phi_{NA}(E')}{\lambda_{\text{int}}(E')} \frac{dn(NA \rightarrow m_k; E', E)}{dE} \quad (2.6)$$

Here NA is the incoming nucleus and m_k the meson produced in the interaction. The $d\phi/d\lambda_{\text{int}}$ term corresponds to the interaction term in the cascade equation, the dn/dE term represents the energy distribution of mesons produced in a hadronic interaction. It is possible for primary CRs to produce nucleons in interactions, this is called nucleon-nucleon regeneration. The calculation is analogous to the production of mesons, only the energy distribution of secondary particles is changed. In the case of mesons their decay contributes to the lepton flux, it can be calculated by replacing λ_{int} with λ_{dec}

$$S(m_K \rightarrow S) = \int_E^\infty dE_M \frac{\phi_{m_K}(E_M)}{\lambda_{\text{dec}}(E_M)} \frac{dn(m_K \rightarrow S; E_M, E)}{dE} \quad (2.7)$$

Here m_K is the decaying meson and S the lepton produced in the decay. As the decay length increases as a function of energy while the interaction length decreases, the equation is usually solved for the high-energy regime where only interactions are considered, and for the low-energy regime considering only particle decays. These two partial solutions are then combined to describe the whole energy range. A more detailed treatment of the solution of the cascade equation can be found in [42] or [28].

Another simplified to calculate the atmospheric lepton fluxes was developed by Gaisser in his book on astroparticle physics [3]. Gaisser gives the flux of atmospheric muons as

$$\frac{dN_\mu}{dE_\mu} = \frac{0.14 E_\mu^{-2.7}}{\text{GeV s cm}^2 \text{sr}} \left(\frac{1}{1 + \frac{1.1E_\mu \cos(\theta)}{115 \text{GeV}}} + \frac{1}{0.054 + \frac{1.1E_\mu \cos(\theta)}{850 \text{GeV}}} \right) \quad (2.8)$$

assuming an $E^{-2.7}$ power-law spectrum for the CR flux. The values of 115 GeV and 850 GeV in this equation correspond to the critical energies of pions and kaons respectively, i.e. the energy at which a particle is equally likely to decay as it is to interact with another particle in the atmosphere. Heavier mesons like unflavored (ω, ρ^0, η) or charmed (D^\pm) mesons have critical energies in the PeV range, which means their interactions inside the atmosphere can be safely neglected. In a less dense medium, the probability of interaction decreases. The Earth's atmosphere is several orders of magnitude more dense than than most astrophysical sources, which means that in most astrophysical sources the critical energies of most mesons exceed the maximum energy of protons. This makes neutrino and gamma emissions from these source almost exclusively dominated by pion production and decay. For example Saba et al. calculated the number density of proton targets for 33 FR-I galaxies that are neutrino source candidates to be on the order of 10^1 cm^{-3} to 10^3 cm^{-3} [43]. For comparison, inside Earth's atmosphere above altitudes of 30 km where most of the atmospheric overburden has been cleared the average number density of nuclei is still on the order of 10^{16} cm^{-3} .

The analytical solutions discussed in this section share several drawbacks, at high energies they do not accurately reflect the cross-sections for proton-proton interaction,

2. Basic Concepts

and they do not consider the contribution from heavier mesons. At low energies they do not consider muon decay or muon energy losses, which makes them less suitable for the goal of this work. As they do not include any information on the shower geometry, they are also unsuited to examine the effect of Earth's magnetic field on the muon direction or the path length of the neutrinos, which would be needed in calculating the oscillation probabilities. Therefore the fluxes of atmospheric leptons will have to be calculated numerically.

2.5. Neutrino Oscillations

In the previously discussed Homestake experiment the flux of neutrinos measured was found to be less than half of the theoretical predictions. This deficiency can be explained by neutrino oscillations. These oscillations occur because neutrinos possess small but distinct masses and their mass and flavor-eigenstates are mixed. Neutrinos are produced through weak interactions in a definite flavor-eigenstate, but their mass-state is a superposition of all three mass-states. Due to their slightly different masses, the mass-eigenstates propagate at slightly different rates. This means that the mixture of mass-eigenstates changes as a function of the distance traveled, which in turn leads to an altered mixture in the flavor-state of the neutrino. The relation between the mass and flavor states is given by the PMNS-matrix (Pontecorvo-Maki-Nakagawa-Sakata)

$$\begin{pmatrix} \nu_e \\ \nu_\mu \\ \nu_\tau \end{pmatrix} = U_{\text{PMNS}} \cdot \begin{pmatrix} \nu_1 \\ \nu_2 \\ \nu_3 \end{pmatrix}. \quad (2.9)$$

Here the ν_i correspond to the mass-eigenstates and the ν_α to the flavor-eigenstates. The PMNS-matrix can be parametrized by three different mixing angles θ_{12} , θ_{13} , and θ_{23} and a single phase δ . In the case of atmospheric neutrinos the oscillations of ν_e are less pronounced than for ν_μ , so for simplicity a scenario with two flavors and a single mixing angle θ_{23} is considered as an example:

$$\begin{pmatrix} \nu_\mu \\ \nu_\tau \end{pmatrix} = \begin{pmatrix} \cos \theta_{23} & \sin \theta_{23} \\ -\sin \theta_{23} & \cos \theta_{23} \end{pmatrix} \cdot \begin{pmatrix} \nu_2 \\ \nu_3 \end{pmatrix}. \quad (2.10)$$

According to [32] the probability $P(\nu_\mu \rightarrow \nu_\tau)$ of a ν_μ to turn into a ν_τ is given by

$$P(\nu_\mu \rightarrow \nu_\tau) = \sin^2(2\theta_{23}) \sin^2\left(\frac{\Delta m^2}{4E_\nu} L\right), \quad (2.11)$$

where L is the distance traveled by the neutrino and Δm the mass difference between the two eigenstates. The survival probability of a muon neutrino is obtained by taking the reciprocal value $P(\nu_\mu \rightarrow \nu_\mu) = 1 - P(\nu_\mu \rightarrow \nu_\tau)$.

In Fig. 2.5.1 the survival probability is shown for different distances: 15 km corresponds to the average height at which neutrinos are produced [32], 450 km corresponds

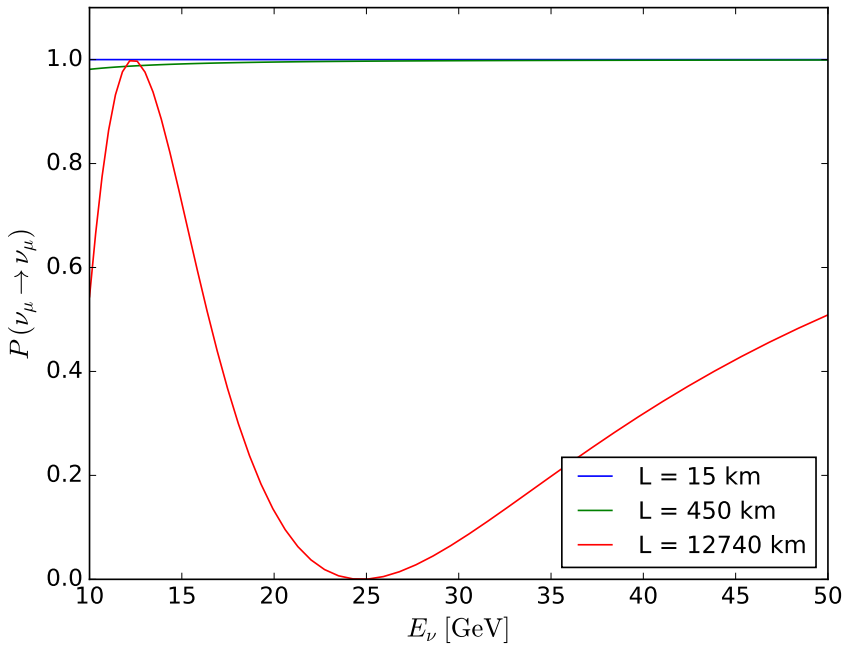


Figure 2.5.1.: Survival probability of a muon neutrino at different energies and distances. The length L corresponds to the average path traveled by down-going (15 km), horizontal (450 km) and up-going (12 740 km) neutrinos.

to the distance traveled by a neutrino arriving from a horizontal direction with the same production height, and 12 740 km corresponds to a neutrino traveling through the Earth. Here, the minimum in the survival probability for up-going neutrinos can be seen around 25 GeV, while there is very little effect for neutrinos that do not travel through Earth. Because of this most experiments study oscillations with neutrinos that travel at least partially through the Earth or at energies below 1 GeV. As the Earth's core is much denser than its mantle, it would be prudent to include matter effects in the calculation of the oscillation probabilities. There exist several numerical codes that include matter effects, as well as the full three neutrino flavors, and the option to add sterile neutrino flavors as well. In this work the NuSQUIDS tool will be used, which is described in more detail in Section 4.4.2.

2.6. Monte Carlo software

The Monte Carlo (MC) methods used in this work can be understood as a numerical solution of the cascade equation using a test-particle approach. The spectrum of CR particles is used as the distribution from which test-particles are drawn. For each CR particle the entire trajectory through the atmosphere is simulated in a probabilistic fashion, i.e. the probability of interaction at any given step along the trajectory is calculated

2. Basic Concepts

by a MC model of the interaction cross-section, which also handles the production of secondaries if an interaction occurs. The decay probabilities and energy spectra of decay products are handled in a similar fashion. Secondary particles produced in interactions or decays are propagated in turn as long as all particles have either reached the surface of the Earth or been removed due to interaction or decay. By keeping track of the particles that arrive at the surface, the spectra of secondaries from the CRs can be calculated. The accuracy in this case is no longer limited by the approximations necessary to solve the cascade equation but rather by the statistical uncertainty due to the number of simulated CR particles. Technically it is still limited by the accuracy of the models of the interaction cross-sections, but that limitation is shared by the analytical solution.

The propagation tool for CRs in Earth's atmosphere used in this work is CORSIKA, which has been originally designed to simulate muons from CRs for the KASCADE experiment in Karlsruhe [44]. For every particle in the shower, CORSIKA tracks the particle's current position and momentum as well as a limited history of the particle, e.g. how many interactions have occurred since the first interaction of the primary CR particle. For particle interactions CORSIKA utilizes several different models, the ones utilized in this work will be discussed in the following section. For the decay of particles CORSIKA relies on PYTHIA. Generally only decays with branching ratios above 1% will be considered, although a few exceptions have been made for the decay of unflavored mesons (see Section 2.2). For particle interactions CORSIKA combines a high-energy model with a low-energy model. Projectiles with an energy above a certain threshold are treated by the high-energy model, projectiles below the threshold by the low-energy model. The value of this threshold typically lies between 80–100 GeV, depending on the combination of models selected. In the following the different models used by CORSIKA will be described in more detail.

While there is a fundamental theory the cross sections for proton-proton interactions at typical CR energies cannot be calculated perturbatively. Therefore, interaction models rely on a phenomenological approach to determine cross sections.

For use with MC simulations event generators need not only to reproduce the empirically observed inclusive spectra, but the exclusive cross sections for all particles than can possibly be produced in the interaction. In order to accomplish this goal, FLUKA combines several different methods: At energies up to 3 GeV to 5 GeV, the resonances produced in the interaction are considered explicitly, but the energies of the primary CR particles in this work exceed that threshold. For hadron-nucleus interactions FLUKA employs the dual parton model (DPM). In this model hadrons are considered as pairs of quarks or diquarks connected by strings. In leading order the interaction corresponds to a Pomeron exchange that leaves two hadronic chains producing particles. Each colliding hadron splits in two systems carrying opposite color charge. Each of those systems combines with the complementary colored system in the colliding hadron. In the case of proton-proton interaction, each proton splits into a quark and a diquark, with the quark in one proton connected to the diquark in the other. This creates two colour-neutral chains that appear as back-to-back jets, that subsequently hadronize. The DPM approach is explained in more detail in [45].

In FLUKA inelastic hadron-nucleus interactions are derived as multiple interactions of

the projectile with a number of target nucleons. Each interaction contributes two chains to the process among which the projectile energy is distributed. Most of the hadrons produced from the chains of the collision escape the nucleus without further interaction [46]. For nucleus-nucleus interactions FLUKA includes an interface to DPMJET, a Monte Carlo model designed for hadronic interactions at CR energies $E_{\text{Lab}} \geq 5 \text{ GeV/n}$, based on a similar formalism. FLUKA has been used for the simulation of neutrinos from CRs in the atmosphere for CR energies up to 100 TeV in [47]. This work aims to improve on that by also considering muons to study the systematic uncertainty for different production channels, that is kaons and pions. As FLUKA covers projectile energies ranging from MeV to TeV, the threshold between high-energy and low-energy model can be set so high that FLUKA effectively covers the energy range in this work on its own, without using a separate high-energy model.

For comparison to FLUKA the EPOS model is used. EPOS is an event generator that calculates the inelastic cross-sections for hadron-nucleus and nucleus-nucleus interactions. EPOS uses parton ladders to describe multiple scattering, with parametrizations that are tuned to yield particle spectra and cross-sections that match experimental data [48]. The parametrizations used in EPOS have been updated to conform to LHC data [49]. This reportedly leads to better – though still not complete – agreement with the observed muon multiplicities at very high energies [17]. To cover the same energy range as FLUKA, EPOS needs to be combined with a low-energy interaction model in CORSIKA. As the GHEISHA model has been shown to not match experimental results very well [50] the only remaining choice is UrQMD. The cross-sections for nucleon-nucleon interactions in UrQMD are stored either in look-up tables or as parametrizations in the form of an algebraic function tuned to experimental data [51]. Inside CORSIKA, these event generators are only used for hadronic interactions, even if some of the codes can also describe particle transport and propagation. That means in each interaction the projectile, its energy and the type of target nucleus (i.e. an oxygen or nitrogen nucleus) are passed to the event generator and the particles produced in the interaction are then propagated further by CORSIKA. In this fashion, contributions from different mesons can be tracked, while the details of the hadronic interaction are treated as a black-box.

3. Phenomenological and Statistical Considerations

This chapter covers a range of phenomena and physical effects that need to be examined in order to determine the optimal parameters for the simulation. Before the main simulation can be started, a few test runs are needed to determine which effects need to be considered, which ones can be safely neglected, and which ones can be used to reduce the computing time necessary for the simulation. Apart from the physical side, the technical aspects need to be considered as well. One has to determine how to incorporate these effects into the simulation, i.e. is it necessary to modify CORSIKA or can the effects be added in post-processing. There are three broad categories that will be investigated here: The influence of the primary CR composition, the impact of the simulated primary and secondary energy range on the CPU requirements, and effects related to the geometry of the air showers and their observation.

With regard to the CR composition the question is if it is necessary to simulate nuclei from all mass groups, e.g. H, He, CNO, MgAlSi, and Fe, or if it is sufficient to simulate only nucleons, i.e. protons and neutrons. In the latter case the number of simulated showers and the necessary CPU time could be reduced to 2/5, with minimal loss of accuracy. This is discussed in Section 3.1.

For analyses of experimental data the showers simulated need to be as realistic as possible. For systematic studies of the fluxes and interaction models, sampling showers at natural frequency often leads to a waste of CPU time. In order to improve the efficiency of the simulation, most of the CPU time needs to be devoted to the most significant contributions. As CORSIKA runtime depends strongly on the primary CR energy and the energy range of secondary particles, efficient sampling can reduce CPU needs by over an order of magnitude. Therefore, this will be the focus of the optimization in Section 3.2.

Above 100 GeV the hadronic core of the shower can be approximated by a straight line, but at lower energies this is no longer the case. The shape of the shower cone, and the distribution of CR directions have to be accounted for. Fully 3D simulations tend to be CPU expensive, because a large number of simulated trajectories can miss the target. If 3D effects can be calculated from a 1D simulation this would drastically improve sampling efficiency. The influence of the Earth's magnetic field on the shape of the shower cone is discussed in Section 3.3, as well as technical details on how that shape is represented in the CORSIKA output.

3.1. Primary CR composition - Superposition approximation

For air showers from high-energy CRs the superposition approximation can be used, which means a primary nucleus ${}_Z^A Y$ with charge number Z , mass number A and an energy E_{CR} can be approximated by Z protons and $A - Z$ neutrons with energy E_{CR}/A each. At lower energies this assumption needs to be confirmed before using it. For this purpose a preliminary spectrum was simulated for only a single zenith angle $\Theta = 0^\circ$ and primary CR energies ranging from 5 GeV to 5 TeV per nucleon for 20 different primary energy bins. FLUKA was used as a low-energy model and QGSJET as the high-energy model. To determine the systematic error incurred by using the superposition approximation showers were simulated for different primary particles: protons, neutrons, and iron and helium nuclei. For each combination of particle and energy 50.000 showers were simulated. The particle yields from iron or helium nuclei of energy E_{CR} were compared against the sum of the yields for $A - Z$ neutron and Z proton yields and energy E_{CR} . While these yields appear to be similar there are some minor discrepancies, two example yields are shown in Figures 3.1.1 and 3.1.2. While the agreement at low energies is generally good, the high energy part is sampled less efficiently in the superposition approximation. This is reflected in larger statistical uncertainties for protons and neutrons compared to nuclei. In many cases the highest energy for nuclei is empty for the equivalent protons and neutrons.

When comparing the resulting fluxes at surface level, there seems to be an error of about 20 % muon neutrinos from helium compared to the superposition approximation, shown in Fig. 3.1.4. The error for muon neutrinos from iron nuclei is shown in Fig. 3.1.3. These errors appear to be relatively large considering the discrepancy at the level of individual yields. One possible explanation could be that the agreement for yields is best at low energies, where the yields are less significant, and the differences at higher secondary energies are where the yields would contribute most significantly to the flux, cf. Section 3.2.1. It appears odd that nuclei are more efficient in producing neutrinos than individual nucleons. While there is no obvious effect in physics that could account for this observation, it could simply be a consequence of the transition between the low-energy and high-energy model in CORSIKA, or of the switch from DPMJET cross-sections for nuclei to the FLUKA specific cross-sections for nucleons. To support this notion, the behavior of the muon flux from iron is shown in Fig. 3.1.5. At low energies, iron nuclei appear less efficient at producing muons, but around 20 GeV the trend reverses and more muons are produced from iron nuclei than the corresponding nucleons. The plots of the remaining lepton fluxes have been moved to the appendix, see Section A. The general deficit of the fluxes obtained with the superposition approximation could be explained simply by the inefficient sampling of the high-energy region of the yields, but the change in the behaviour of the iron fluxes strongly suggests that another effect contributes as well.

Whatever the reason for this behavior is, the effect on the resulting lepton fluxes is limited. When taking into account that helium nuclei constitute about 20 % of the

3.1. Primary CR composition - Superposition approximation

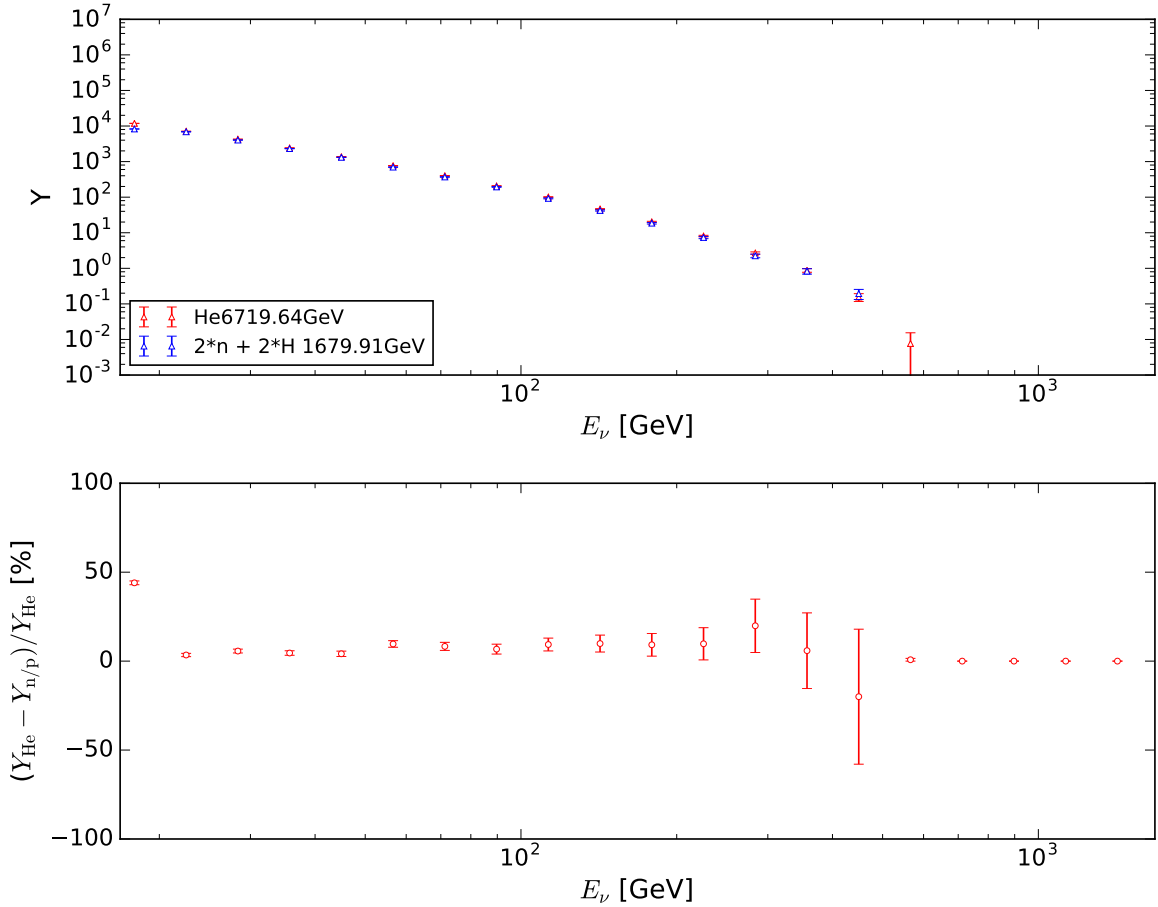


Figure 3.1.1.: Example comparison of the ν_μ yields for helium; superposition in blue, helium nuclei in red. Overall helium is only slightly more effective in producing neutrinos than the superposition suggests, but at the highest energies the contribution is no longer sampled efficiently.

primary flux, with protons making up about 80 % one would expect the cumulative error on the combined flux to be lower. This is shown in Fig. 3.1.6, the flux of muon neutrinos from hydrogen and helium combined is compared to the flux of hydrogen combined with helium represented by the superposition of protons and neutrons. The resulting error of the combined flux drops to about 5 %. As all heavier nuclei make up an even smaller fraction of the primary CR flux, the cumulative error due to the superposition approximation is estimated to be about 7 % to 10 %. While this error seems large compared to the statistical uncertainties, considering the potential uncertainty due to the interaction models and geometry it seems to be acceptable to use the superposition approximation.

3. Phenomenological and Statistical Considerations

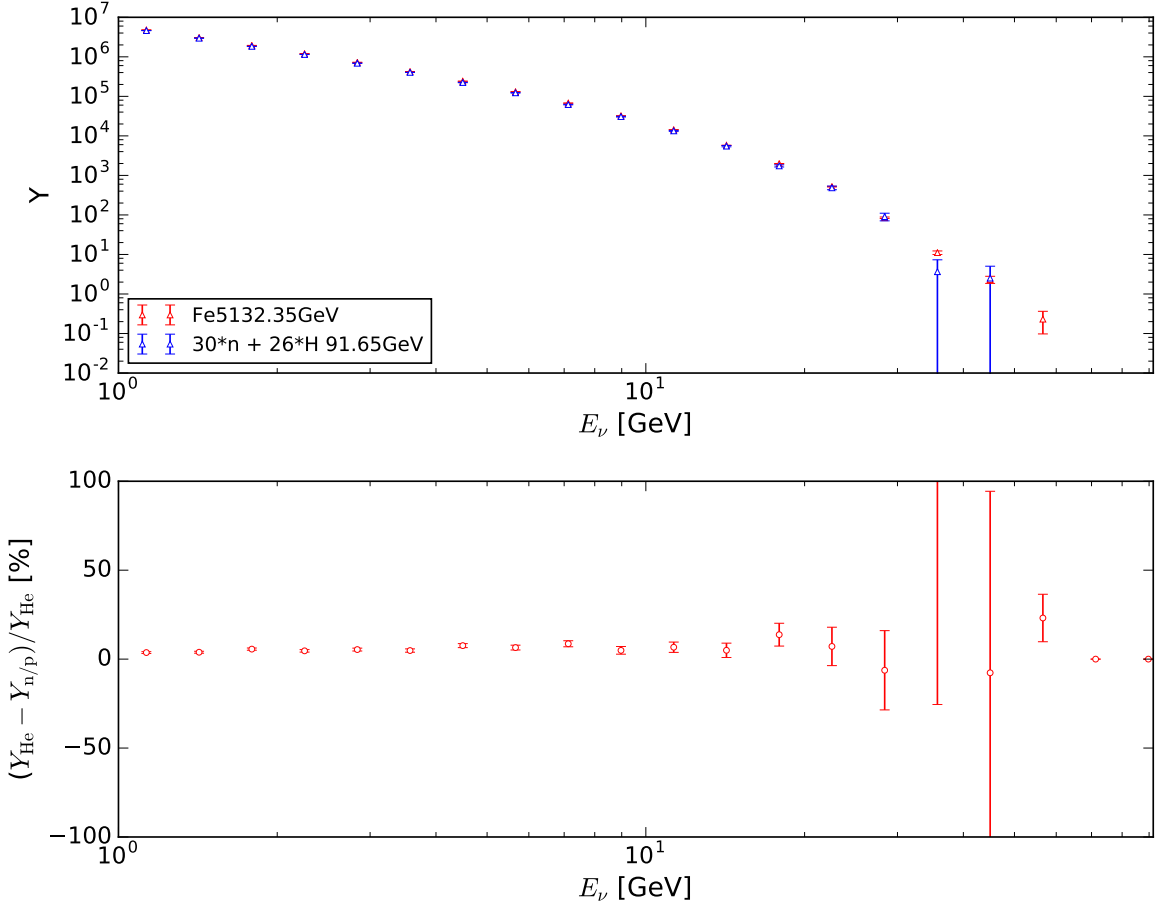


Figure 3.1.2.: Example comparison of the ν_μ yields for iron; superposition in blue, iron nuclei in red. While the overall differences are small, at the highest energies the contribution of iron is sampled more efficiently than the superposition of protons and neutrons.

3.1.1. Nucleon flux from CR nucleus flux

For use with the superposition approximation, the flux of CR nuclei has to be expressed as the corresponding flux of nucleons, keeping in mind that

$$\Phi(E_{\text{CR}}, Z) = \frac{dN_{\text{CR}}}{dE_{\text{CR}} dA dt}(E_{\text{CR}}), \quad (3.1)$$

although throughout the rest of the calculation the $dA dt$ part will be omitted for brevity. It is assumed that one CR nucleus ${}_Z^A Y$ with energy E_{CR} corresponds to A nucleons with energy $E_{\text{nucleon}} = E_{\text{CR}}/A$ each. When calculating the spectrum of protons with energy E_p it is important to take into account that the spectrum is differential, i.e.

$$\Phi(E_p, Z) = Z \frac{dN_{\text{CR}}(E_p)}{dE_p} = Z A \frac{dN_{\text{CR}}(E_{\text{CR}}/A)}{dE_{\text{CR}}}. \quad (3.2)$$

3.1. Primary CR composition - Superposition approximation

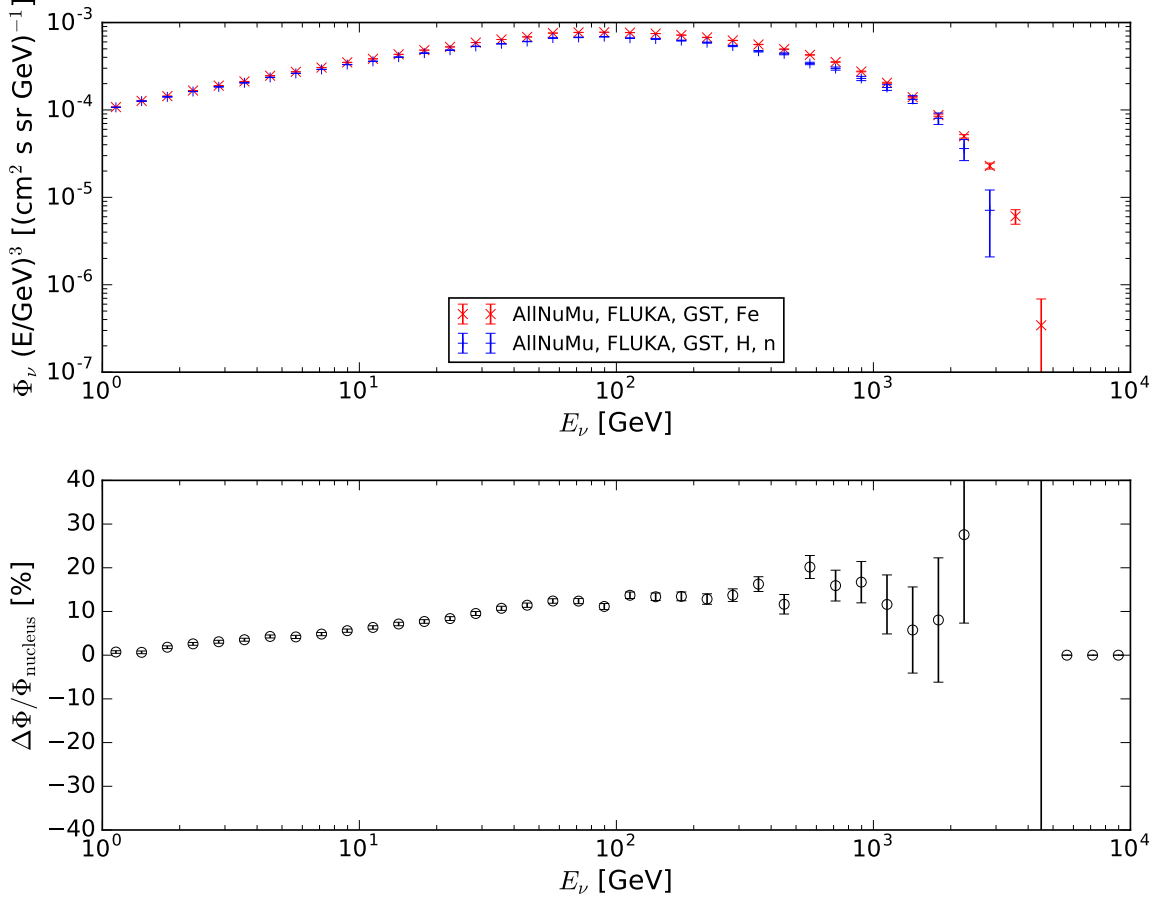


Figure 3.1.3.: Comparison of the muon neutrino flux from iron nuclei, superposition in blue, iron nuclei in red. Here, the deficit of the superposition approximation can be seen clearly rising with energy.

This yields the correct result when calculating the number of protons in a given energy range:

$$N_p = \int_{E_1}^{E_2} Z \frac{dN_{\text{CR}}(E_p)}{dE_p} dE_p. \quad (3.3)$$

Taking into account that most CR models give the flux as a function of E_{CR} , i.e. $\Phi(E_{\text{CR}}) = dN_{\text{CR}}/dE_{\text{CR}}$, the proton flux can be expressed by substituting $E_{\text{CR}} = A E_p$ in the CR flux term

$$N_p = \int_{A E_1}^{A E_2} Z A \frac{dN_{\text{CR}}(E_{\text{CR}}/A)}{dE_{\text{CR}}} \frac{1}{A} dE_{\text{CR}} = Z N_{\text{CR}}. \quad (3.4)$$

For calculating weights, the integral is evaluated as a function of E_p , and the proton flux is obtained from the CR models by using $\Phi_p(E_p) = Z A \Phi_{\text{CR}}(A E_p)$. The flux and number of neutrons can be calculated analogously by replacing Z with (A-Z) in the above calculation.

3. Phenomenological and Statistical Considerations

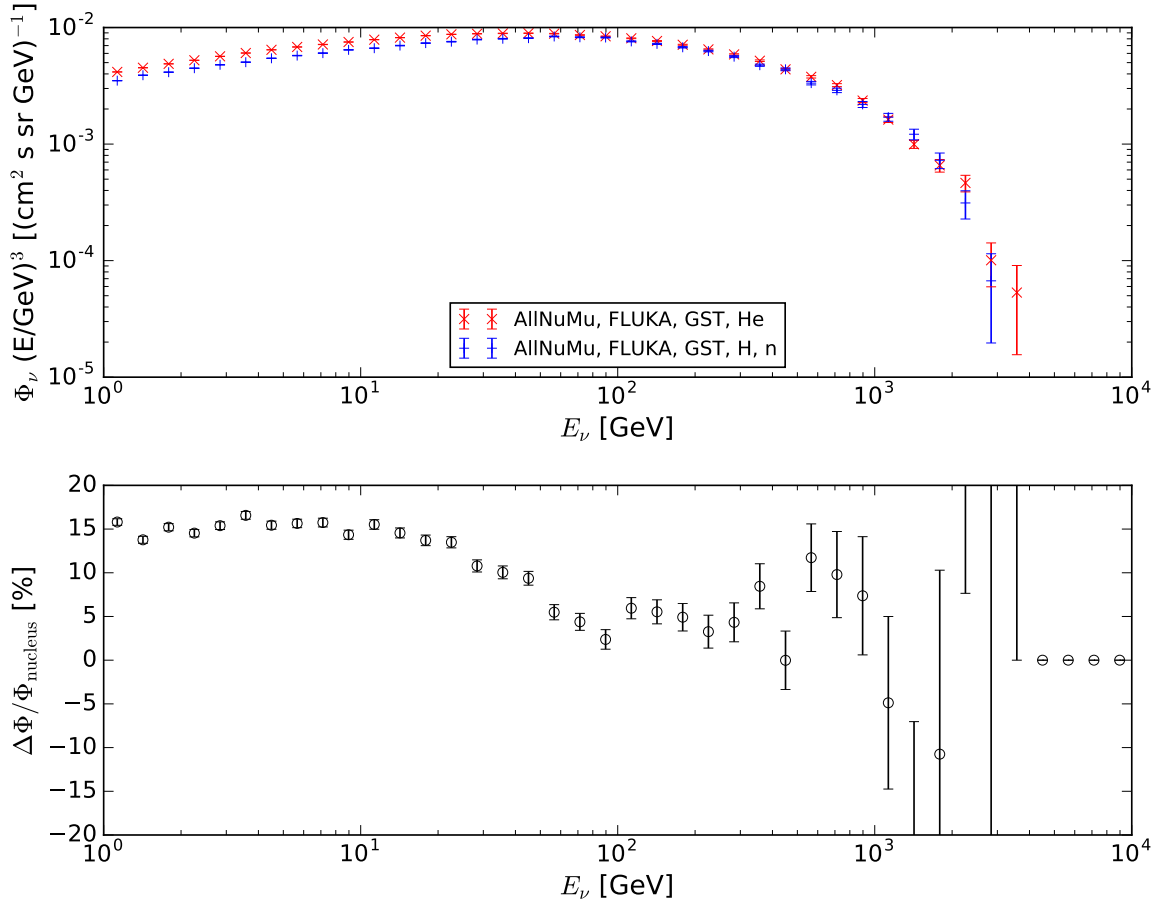


Figure 3.1.4.: Comparison of the muon neutrino flux from helium nuclei, superposition in blue, helium nuclei in red. The deficit of the superposition approximation decreases from 1 GeV to 100 GeV, but rises again at higher energies.

3.1. Primary CR composition - Superposition approximation

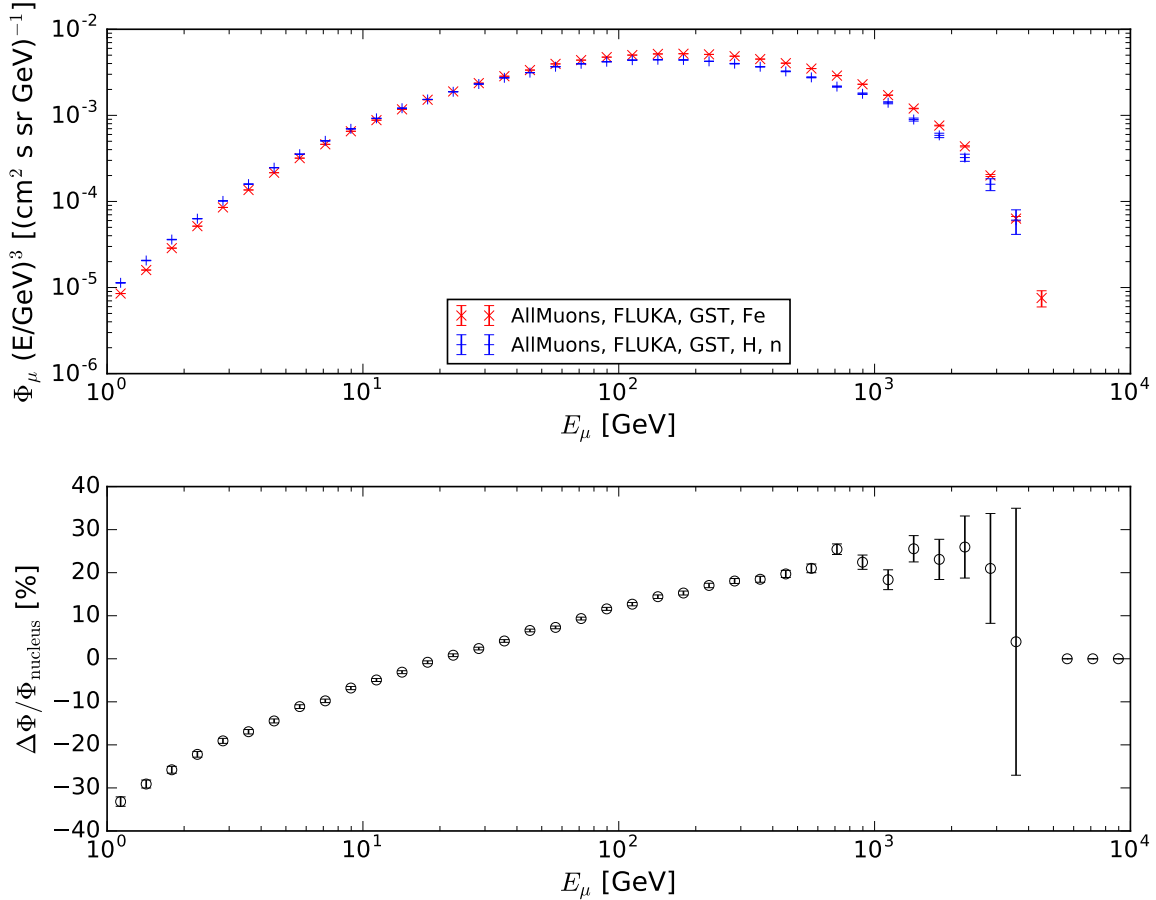


Figure 3.1.5.: Comparison of the muon flux from iron, superposition in blue, actual iron in red. The difference between iron nuclei and the superposition rises continuously, below 20 GeV the superposition shows a clear deficit, above that energy it produces more muons than a iron nucleus.

3. Phenomenological and Statistical Considerations

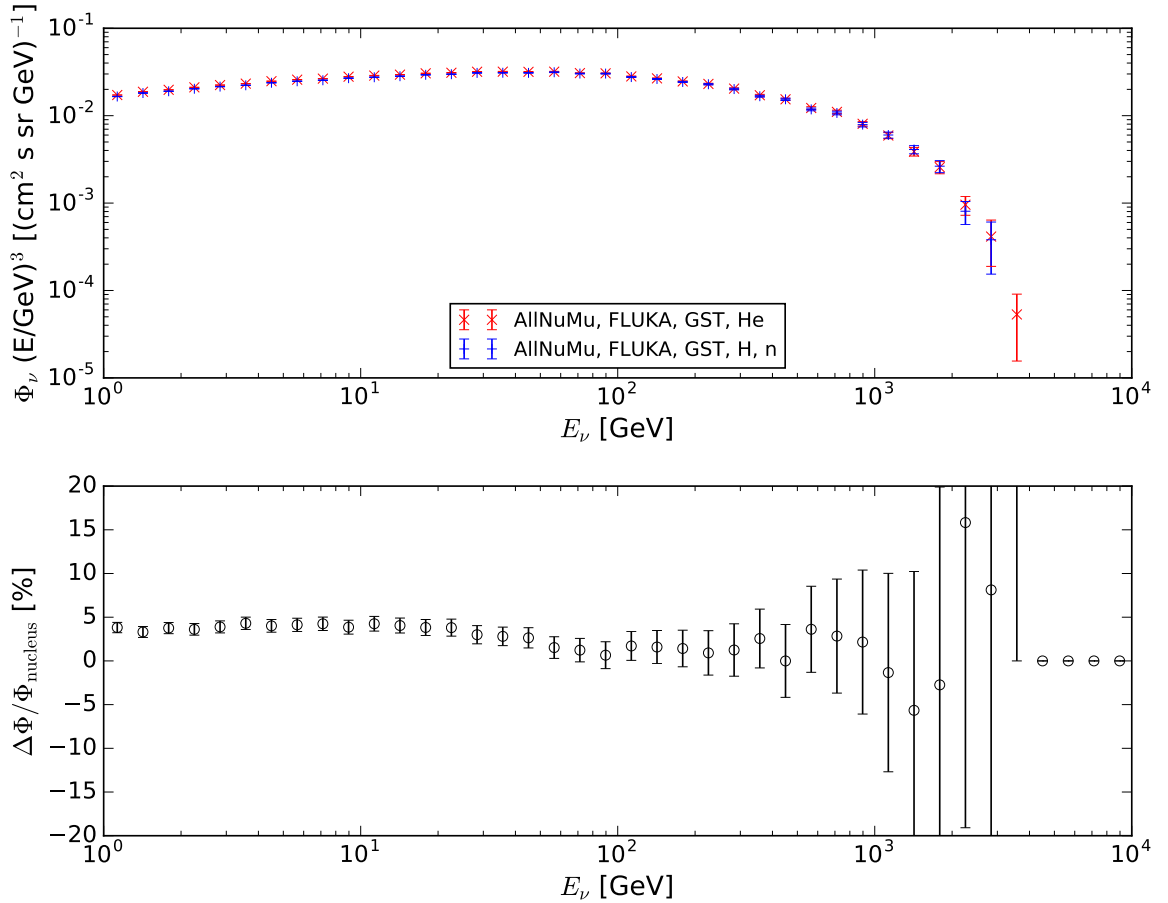


Figure 3.1.6.: Comparison of the muon neutrino flux from helium nuclei and protons combined, superposition in blue, helium nuclei in red. Due to the relatively small contribution of helium to the overall flux, the error of the superposition approximation is reduced.

3.2. Importance Sampling

3.2.1. Sliding low energy cutoff

The CORSIKA runtime scales roughly linearly with the primary CR energy, because the number of secondary particles produced in the shower increases with the primary CR energy. However, those particles are not evenly distributed in energy, instead the number of secondary particles as a function of energy E_S resembles a power-law. Therefore, usually secondary particles are discarded once their energy falls below a certain threshold. As the CR spectrum spans several orders of magnitude in energy, the CPU requirements of the simulation can become prohibitive if the highest CR energies are to be simulated, while keeping the low-energy threshold constant. However, the contribution of secondary particles to the inclusive flux is not equally significant from all primary CR energies. Showers can be sampled more efficiently.

A large portion of the computing time in CORSIKA simulations is spent on high multiplicity, low-energy particles, even though these particles contribute only very little to the flux at surface level. As an example, the relative contribution of yields for different CR energies to the electron neutrino flux is shown in Fig. 3.2.1. It can be seen that the largest contribution of a yield is close to the associated CR energy. The contribution of a yield increases with $x = E_S/E_{\text{CR}}$ up to a maximum $x_{\text{max}} < 1$. Note that for $x \leq 0.001$ the contribution to the resulting flux is less than 1 %, which is of the same order as the statistical uncertainty. Any secondary particles with $x \leq 0.001$ can therefore be discarded without significant impact on the resulting flux.

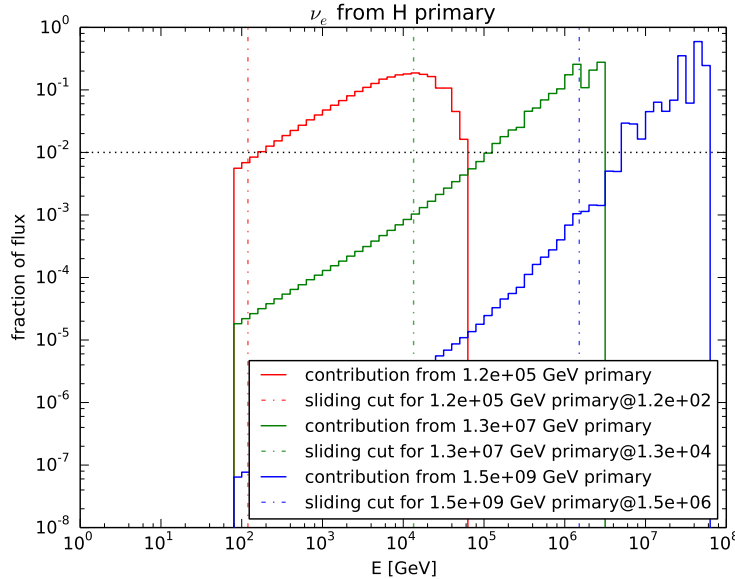


Figure 3.2.1.: Contribution of different yields to the secondary flux.

An alternative way of looking at this is to show the yields as a function of x , and weight them with x^3 , which corresponds to a generic E^{-3} CR spectrum. This has been

3. Phenomenological and Statistical Considerations

done in Fig. 3.2.2 for yields of $\bar{\nu}_\mu$ obtained with FLUKA and QGSJET-II. For FLUKA it is easy to see that the weighted yields are peaked around $0.1 \leq x \leq 1$. In the case of QGSJET-II the peak is not always visible, because at higher energies the high x region is not sampled efficiently, due to mesons interacting. When viewed as a function of x , the shape of the yields for different values of E_{CR} is very similar, as long as meson interaction can be neglected. The most significant contribution of a yield to the secondary flux will be around the peak in x . So, as long as the peak can be resolved clearly – with some tolerance to accommodate deviations of the CR flux from a pure E^{-3} power-law – the low- x tail can be neglected.

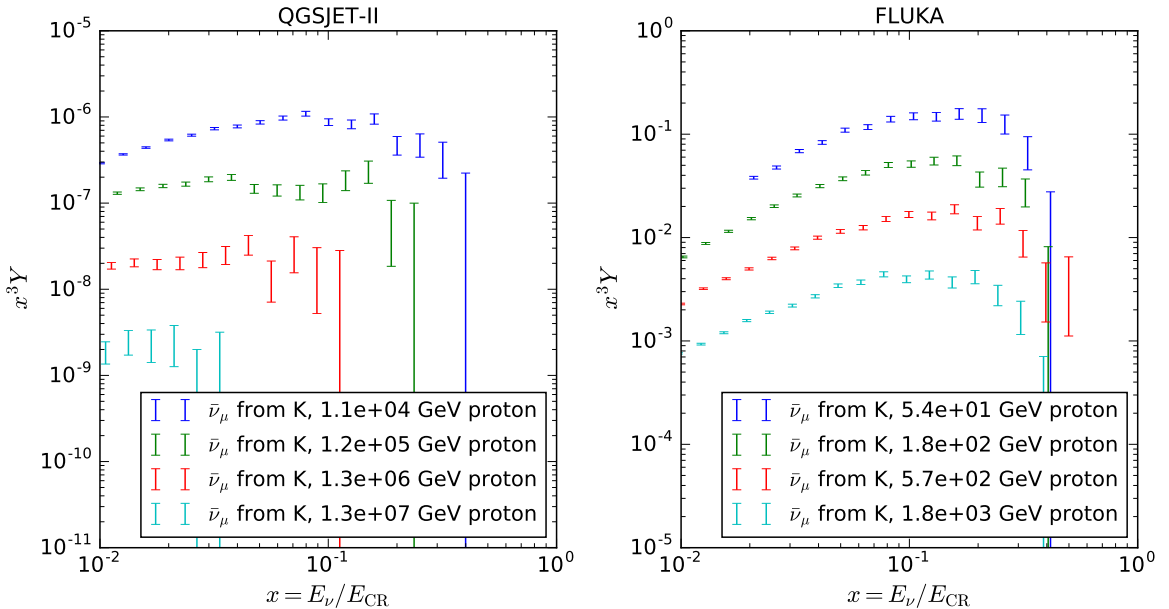


Figure 3.2.2.: Yields shown as a function of x , weighted with x^3 as a generic CR spectrum. FLUKA yields (right) from this work, QGSJET-II yields (left) from [2]. A peak can be seen around $x = 0.1$. Note that because a different number of showers has been simulated for each model, the normalization of the yields does not have to agree.

Discarding low- x particles changes the dependence of the CPU time on the primary CR energy. Because the FLUKA license discourages benchmarks, the principle is demonstrated using SIBYLL-2.3. Fig. 3.2.3 shows the runtime for CR proton showers with energies ranging from 10^2 GeV to 10^{10} GeV and 50.000 particles simulated in each run. The low energy cutoff was set to $x_{\text{cut}} = 10^{-4}$ or 100 GeV, whichever was higher. The absolute cutoff of 100 GeV ensures that only SIBYLL-2.3 is used. For primary energies up to 10^6 GeV, the runtime increases almost linearly with energy ($\propto E_{\text{CR}}^{0.86}$), because the energy range that has to be simulated increases continuously. Above that energy, the simulated energy range remains constant, and the runtime only increases slowly with energy, ($\propto E_{\text{CR}}^{0.16}$). Extrapolating from the increase in runtime before the cutoff takes effect, this method can save more than two orders of magnitude in CPU time, with only a very

3.2. Importance Sampling

minor $\leq 1\%$ systematic error. For nuclei E_{CR} would have to be replaced with E_{CR}/A and the cutoff for x be modified accordingly, but as the superposition approximation will be used, this is of no consequence here.

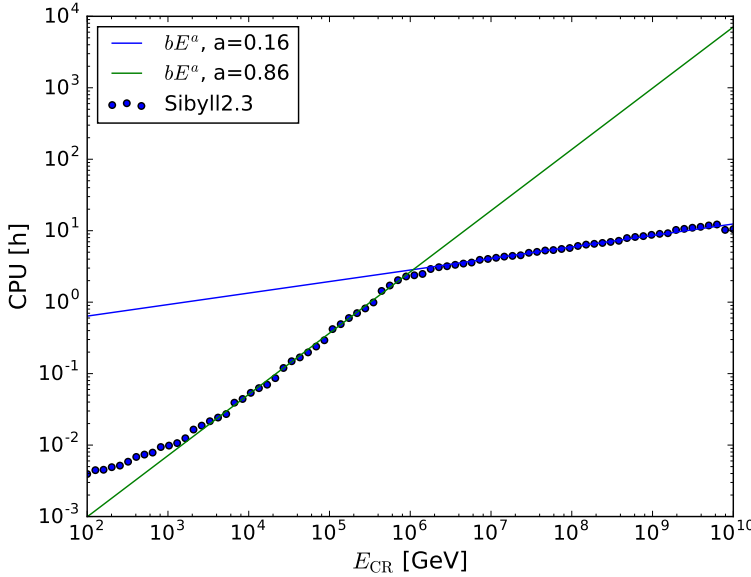


Figure 3.2.3.: Simulation runtime of SIBYLL-2.3 as a function of primary CR energy, shown here for CR protons.

For the purposes of experiments the sliding cutoff produces very unrealistic showers, so it cannot be used for event reconstruction. However, it is still possible to speed up the simulation for some models, as FLUKA is faster than both EPOS and QGSJET-II. For example, if a simulation of showers containing muons from the decay of unflavored mesons were desired, it would be possible to combine EPOS and FLUKA, with a relatively high transition energy from the high-energy to the low-energy model. This energy can be set in CORSIKA using the HILOW parameter. That way, the first and most significant interactions would be handled by EPOS, which is tuned to produce more η mesons, while FLUKA could provide a realistic low- x part of the shower in considerably less time than EPOS. The potential time saving is illustrated in Fig. 3.2.4. Here the runtime is shown for EPOS, SIBYLL-2.1, and QGSJET-II combined with FLUKA for different values of the transition energy HILOW between the two models. For SIBYLL-2.1 the performance is slightly better than FLUKA, so increasing HILOW causes no improvement. For QGSJET-II and especially for EPOS, increasing the HILOW parameter reduces the runtime. The improvement in performance is less than one order of magnitude, so for the purpose of this work, the sliding cutoff is preferable. For future studies that require complete, realistic showers to be simulated, using FLUKA with a HILOW parameter of about 10 TeV to 100 TeV – or possibly even a sliding HILOW parameter as a function of x instead of a constant – could improve performance.

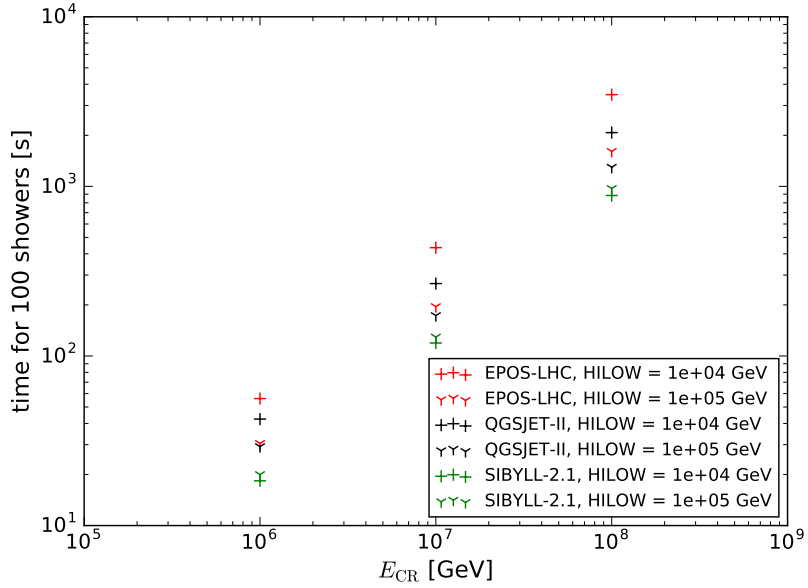


Figure 3.2.4.: Simulation runtime of EPOS, SIBYLL-2.1, and QGSJET-II as a function of CR energy. Each model is combined with FLUKA as the low-energy model and a varying transition energy HILOW. For each CR energy the vertical distance between two markers of the same color corresponds to the time saved by increasing HILOW by a factor of ten.

3.2.2. Forced meson decay

At high energies, secondary interactions of mesons with particles of the atmosphere lead to increased statistical uncertainties, as mesons that interact no longer contribute anything to the flux of muons and neutrinos. As the cross-sections for interaction increase with energy, this effect is particularly problematic for the mesons that carry the highest fraction of the CR energy, which contribute to the region where the yield is most significant. Forcing the decay of mesons that would normally interact can improve the sampling of the high- x region. However, their weight has to be reduced according to their interaction probability, to obtain a flux with the correct normalization. This option was implemented in CORSIKA by Jakob van Santen [private communication]. Fig. 3.2.5 shows the muon yields for 1.000 showers of 1 PeV protons, obtained with standard CORSIKA and the modified CORSIKA version. Note the smaller statistical uncertainty throughout, and better coverage of the region $x \geq 0.1$. This option offers the greatest benefits at the highest energies, whereas below the critical energy of pions and kaons the benefits are negligible. As the focus of this simulation is on the lepton energy range from 1 GeV to 1 TeV, this modification is not adopted and an unmodified CORSIKA version is used instead.

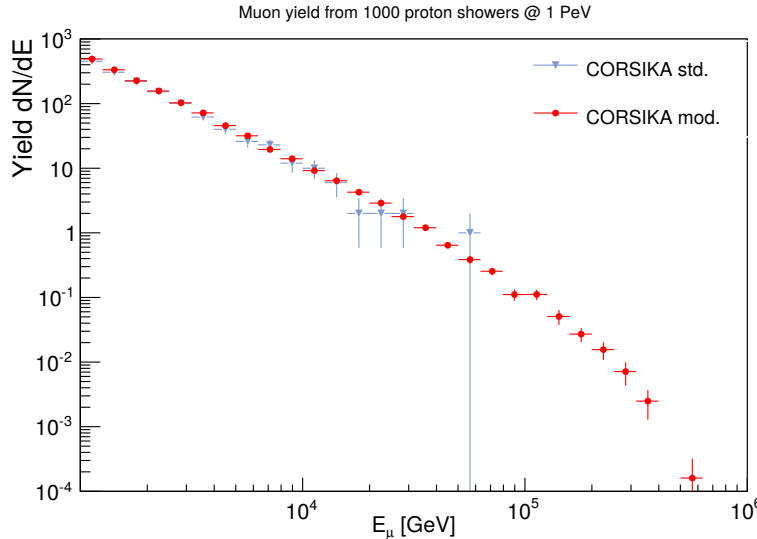


Figure 3.2.5.: Muon yields with standard CORSIKA and with forced decay of mesons. Note the much improved coverage of the region above 10^5 GeV with the modified version.

3.3. Geometric effects

3.3.1. Geomagnetic Cutoff

As CR particles approach the Earth they will be deflected by the Earth's magnetic field, in particular at low energies. The Earth's magnetic field can be approximated by a dipole, which means that the strength of the deflection of the CR particle depends on its direction as well as its energy. In some directions the deflection can become strong enough to prevent particles from reaching the atmosphere if they fall below a certain energy threshold. This threshold is called the geomagnetic cutoff, for vertical CRs its values range from 0.5 GV at the geographic poles to up to 15 GV above the equator [52]. For any particular experiment, the cutoff needs to be known not only in the vertical direction, but also for CRs that arrive from horizontal direction. In the latter case the cutoff value can be much larger, for example, at the south pole the cutoff for horizontal CRs ranges from 1 GV to 40 GV depending on the azimuth [53]. The calculation of the exact cutoff value for all directions is beyond the scope of this work, but the effects of the geomagnetic cutoff can be included without the need for additional CORSIKA simulation. It is sufficient to apply the cutoff to the primary CR model, effectively reducing the associated weights to 0 if E_{CR} is below the cutoff value. The CORSIKA yields can be weighted with the modified primary spectrum to obtain the flux at surface level.

3. Phenomenological and Statistical Considerations

3.3.2. Muons in the Earth's magnetic field

The effect of the Earth's magnetic field on the trajectories of muons needs to be considered. According to [54] the deflection of muons in the Earth's magnetic field is negligible compared to the geomagnetic cutoff for primary CR particles. This needs to be verified.

The gyroradius r_G of a particle can easily be calculated from its rigidity $R = pc/(Ze)$ according to [4]:

$$r_G = \frac{R}{B} \quad (3.5)$$

$$r_G = \frac{pc}{ZeB}, \quad (3.6)$$

where c is given in units of m s^{-1} , B in units of T , p in units of GeV/c . V T^{-1} is equivalent to $\text{m}^2 \text{s}^{-1}$ and for muons, pions or kaons $Z = 1$. This leads to:

$$r_G = \left(\frac{p}{\text{GeV}} \right) \left(\frac{B}{\text{T}} \right)^{-1} \left(\frac{c}{\text{m/s}} \right)^{-1} \text{m}. \quad (3.7)$$

The deviation $\Delta\theta$ from the original CR trajectory over a distance traveled d is then given by:

$$\Delta\theta = \frac{d}{r_G} \frac{180^\circ}{\pi}. \quad (3.8)$$

The effect of Earth's magnetic field on pions is negligible due to the short life time, for muons the angular deviation per decaylength $\Delta\theta/\lambda_{\text{dec}}$ is equal to a constant of $\approx 3.2^\circ$ for a magnetic field of $30 \mu\text{T}$, with a linear dependence on the magnetic field strength B . This means that larger deviations are suppressed by muon decay, and most of the surviving muons at low energies are still expected to arrive in a rather narrow cone. Assuming a production height of $\approx 15 \text{ km}$ the average angular deviation due to Earth's magnetic field can be calculated. This is shown in Fig. 3.3.1, even without considering the decay of muons the deviation is smaller than 10° for energies above 2 GeV , and drops to zero for energies above 100 GeV .

These results can be compared to muons simulated with CORSIKA. The lateral distribution for muons simulated in CORSIKA is shown in Fig. 3.3.2 and Fig. 3.3.3. As expected muons with higher energies have smaller deviations in their lateral distribution. These distributions are also slightly off-center. Depending on their charge muons exhibit a shift in their distribution along the East-West direction, which is to be expected for a magnetic field that is mostly aligned in the North-South direction. As shown in Table 3.1, this shift also decreases for higher muon energies, but independent of energy the shift is small compared to the standard deviation of the distribution. This suggests that the influence of Earth's magnetic field is small compared to the initial angle between lepton and primary CR particle due to the kinematics of the hadronic interactions and subsequent meson decays. As those processes are largely stochastic, information of the exact arrival location of the lepton on the Earth's surface with regard to the East/West and North/South direction is not strictly necessary. The distributions exhibit sufficient symmetry to be characterized by the radius of the shower footprint, or – more suitable for inclined showers – the opening angle of the shower cone.

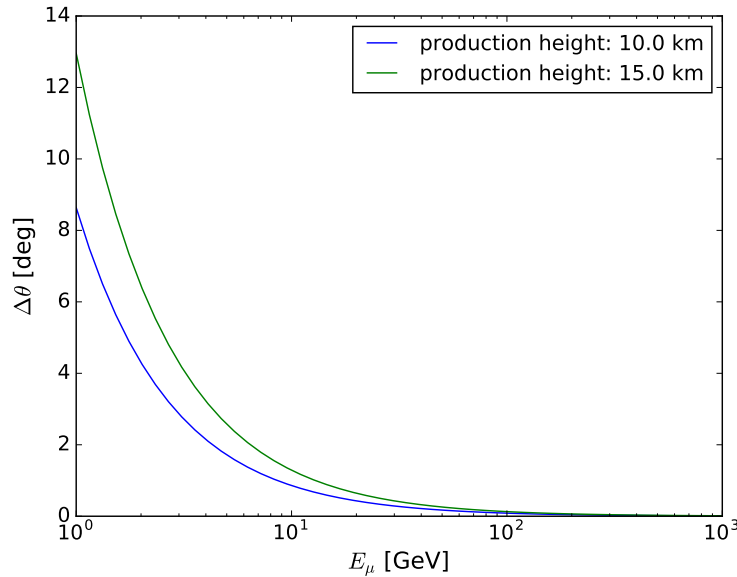


Figure 3.3.1.: Magnetic deviation of a muon in Earth's magnetic field for a shower from a vertical CR.

Particle	\bar{x} [km]	\bar{y} [km]
μ^- , 1 GeV	0.003 ± 1.032	0.167 ± 1.037
μ^+ , 1 GeV	0.001 ± 1.020	-0.196 ± 1.025
μ^- , 5 GeV	0.006 ± 0.620	0.109 ± 0.628
μ^+ , 5 GeV	0.001 ± 0.591	-0.118 ± 0.600

Table 3.1.: Average arrival location of muons, x corresponds to North-South direction, y to East-West direction. Along the East-West axis there is a noticeable difference between μ^+ and μ^- , but that difference is smaller than the standard deviation of each group.

3. Phenomenological and Statistical Considerations

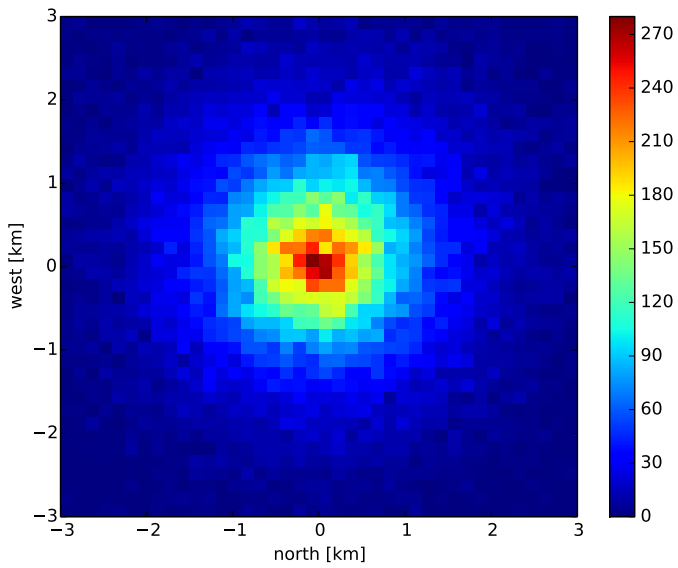


Figure 3.3.2.: Lateral Distribution of 1 GeV muons. While the center of the distribution is shifted slightly from the center of the coordinate system, the shift is barely visible due to the width of the distribution.

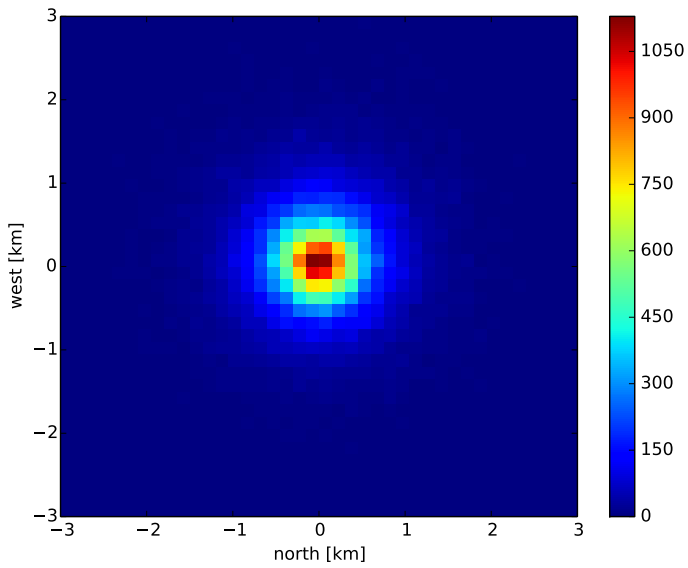


Figure 3.3.3.: Lateral Distribution of 5 GeV muons. While the center of the distribution is shifted slightly from the center of the coordinate system, this shift is smaller than the standard deviation of the distribution.

3.3.3. Geometry of CORSIKA output

Apart from the particle type and momentum, the standard output of CORSIKA also gives the (x, y) coordinates of all particles that intersect with the observation plane(s). The angle between the surface normal and the direction of the CR particle is θ . The CR trajectory intersects the observation level at the point $(0, 0)$, which corresponds to the location of the detector. The height h at which the particle was produced can be extracted from the particles ancestors, which are available through the EHIST option. The modified ROOT output only considers leptons, so the hadronic part of the shower is not recorded, but the leptonic part of the shower cone can be reconstructed. An example of this is shown in Fig. 3.3.4.

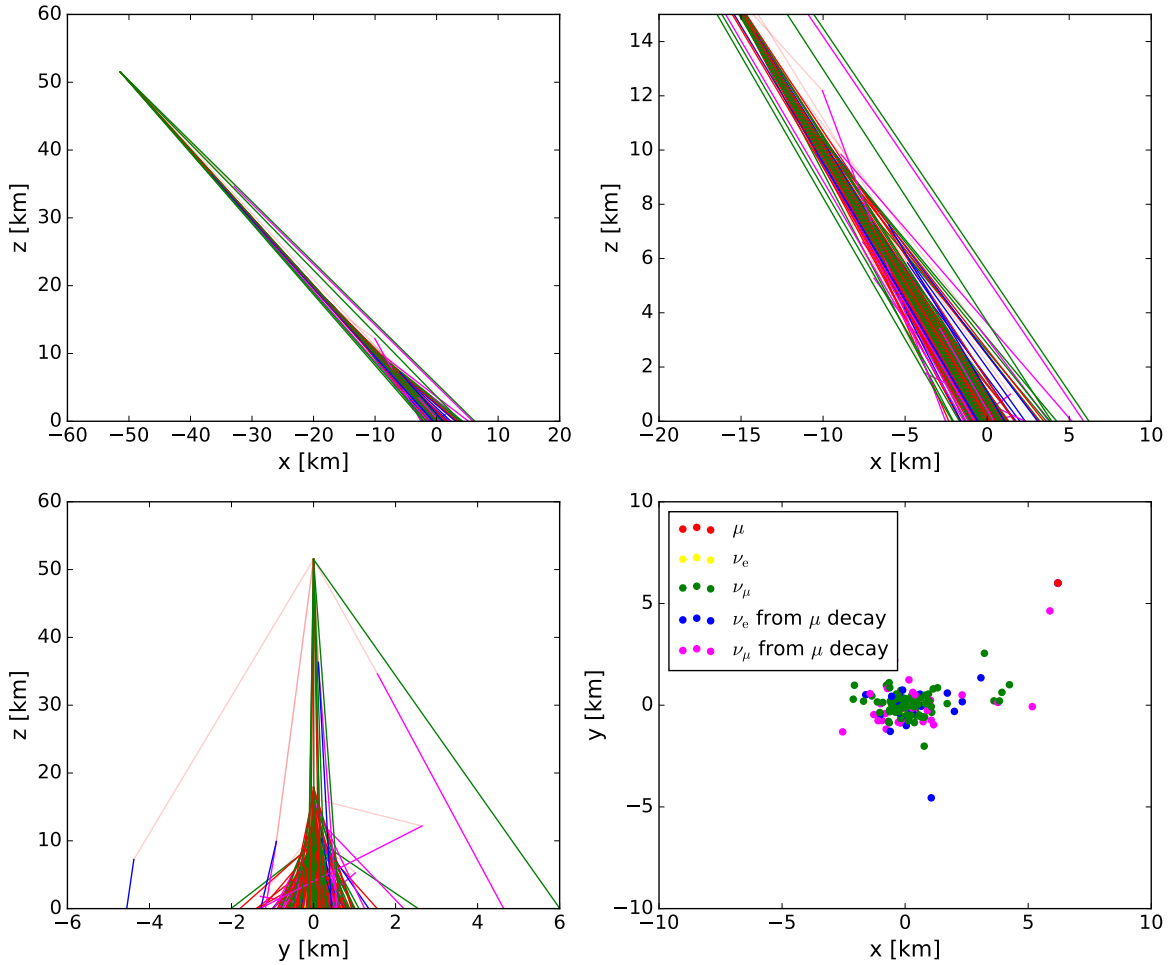


Figure 3.3.4.: Example CORSIKA shower of a 20 TeV proton at $\theta = 45^\circ$. Projection in three planes, from top-left to bottom-right: x-z, x-z magnified, y-z and x-y.

The geometry of the CORSIKA output poses a problem for inclined showers, in particular at energies below 10 GeV. The CURVED option in CORSIKA forces the output to project the x and y coordinates of the particles onto the surface of the Earth for zenith

3. Phenomenological and Statistical Considerations

angles greater than 85° . For consistency this projection will be used for all showers, not just those showers close to the horizon, by explicitly activating the CURVOUT option. In this case the cartesian coordinates (x, y) are replaced with (x', y') , which can be used to calculate the zenith angle θ^* and azimuth angle ϕ^* of the point on the Earth's surface using the following expressions:

$$\theta^* = \frac{\sqrt{x'^2 + y'^2}}{R_{\text{Earth}}}$$

$$\phi^* = \text{atan2}(y', x').$$

This definition is described under the CURVED and CURVOUT options in the CORSIKA manual [55]. For values close to the shower core the new coordinates are approximately equal to the standard cartesian coordinates, i.e. $(x, y) \approx (x', y')$, but at energies below 10 GeV the separation between the particle and the main shower axis can exceed 10 km and $(x, y) \neq (x', y')$. For the purpose of this work it would be preferable to use the height h at which the particle was produced and the opening angle α between the original CR axis and the trajectory of the lepton instead of (x, y) . These quantities can be extracted, assuming a cylindrical symmetry of the shower cone. In addition to that, it is assumed that mesons do not deviate significantly from the symmetry axis of the shower, as their trajectories are much shorter than the trajectories of leptons. The height h above sea level at which a meson was produced can be extracted using the EHIST output in CORSIKA. For the mother or grandmother particle of a lepton the EHIST option replaces the time since first interaction by the altitude above sea level h in the CORSIKA output. Using this altitude it is possible to calculate the opening angle of the shower cone α from the (x', y') coordinates where the lepton reaches the observation level. First of all, the altitude above ground h of the meson is converted to the length l along the CR axis:

$$\rho = \arcsin \left(\frac{R_{\text{Earth}}}{(R_{\text{Earth}} + h) \cdot \sin \theta} \right)$$

$$\lambda = \theta - \rho$$

$$l = (h + R_{\text{Earth}}) \cdot \frac{\sin \lambda}{\sin \theta},$$

where θ is the angle between the primary CR direction and the surface normal of the Earth, as per the standard CORSIKA output. In the next step, the coordinates (x', y') are converted back into cartesian coordinates

$$\theta^* = \frac{\sqrt{x'^2 + y'^2}}{R_{\text{Earth}} + o}$$

$$\phi^* = \text{atan2}(y', x')$$

$$d = (R_{\text{Earth}} + o) \cdot \sin \theta^*,$$

following the definitions in the CORSIKA manual [55], where o is the height of the observation level and the starred angles θ^* and ϕ^* correspond to the spherical coordinates

of the lepton. The cartesian coordinates \vec{x} of the lepton are then given by:

$$\begin{aligned}x &= d \cos \phi^* \\y &= d \sin \phi^* \\z &= (R_{\text{Earth}} + o) \cdot \sin \theta^*. \end{aligned}$$

Similarly, the coordinates \vec{m} of the meson can be calculated:

$$\begin{aligned}m_x &= l \sin \theta \\m_y &= 0 \\m_z &= l \cos \theta. \end{aligned}$$

With the two vectors \vec{x} and \vec{m} the opening angle α can be expressed as:

$$\alpha = \arccos \left(\frac{(\vec{m} - \vec{x}) \cdot \vec{m}}{\|\vec{m} - \vec{x}\| \|\vec{m}\|} \right) \quad (3.9)$$

For neutrinos from muon decay the calculation is analogous, only the height h of the meson is replaced with the height at which the muon decayed.

3.3.4. Mirroring

In the course of the preliminary CORSIKA studies a fundamental problem was discovered: For those secondary particles where $\alpha \geq 90^\circ - \theta$ (θ in this case is the zenith angle of the original CR, as in the cartesian CORSIKA coordinate system) the cylindrical symmetry of the shower cone is broken. If the particles' trajectories deviate from the CR direction toward Earth they will reach the observation plane, if they deviate away from Earth they might never intersect with the Earth's surface and will therefore never be written to the CORSIKA output. Instead, after a certain time has elapsed, those particles are simply discarded. This problem is illustrated in Fig. 3.3.5. While the CURVOUT option complicates the situation slightly, the fundamental issue is also present for a plane observation level, as shown in the figure. It should be noted that the absolute number of particles in the green shaded region is roughly equal to the number of particles in the red and blue shaded regions combined. Particles in the blue shaded region are distributed over a much larger area on the ground compared to those in the green shaded region, which is not reflected in this projection.

While this projection does give a correct image of events in an individual shower – as needed for experiments – it causes the zenith dependence of the inclusive fluxes calculated with CORSIKA to deviate from the expected results. As shown by Lipari [56] the neutrino flux should be enhanced toward the horizon due to geometric considerations. In Fig. 3.3.6 the fluxes calculated with CORSIKA are shown compared to the fluxes from the Honda simulation [57]. It is obvious that the CORSIKA fluxes drop toward the horizon, and that this trend becomes worse for lower energies. For 1.8 GeV the horizontal flux actually is lower than the flux from vertical direction, which is in clear contradiction

3. Phenomenological and Statistical Considerations

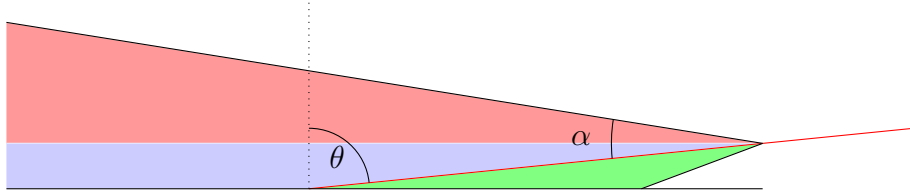


Figure 3.3.5.: Schematic of shower cone projection onto observation level: Lepton trajectories in the red shaded regions never reach the observation level, trajectories in the blue shaded region could potentially reach the observation level, those in the green shaded region will definitely reach the observation level.

to other simulations, as well as experimental data and geometric principles. Above ≈ 30 GeV, the effect seems to disappear, also showers with $\theta \leq 70^\circ$ seem unaffected.

To remedy this problem the CORSIKA output is modified for leptons from zenith angles $\theta \geq 70^\circ$ and energy $E \leq 31.62$ GeV. This energy value has been chosen because it coincides with one of the boundaries of the energy bins. For leptons inside this energy and zenith range, those leptons from the part of the shower cone facing toward Earth are counted with a weight of 2, whereas those from the part of the shower cone facing away from Earth are discarded, effectively mirroring one half of the shower cone to replace the other. This weighting scheme is illustrated in Fig. 3.3.7. Since this only applies to particles with low energies of which there are plenty, the statistical uncertainty is not affected severely. However, this approach introduces a few systematic effects: As leptons from the part of the cone facing Earth need to travel shorter distances to reach Earth, the decay of muons may be underestimated. In addition to that, the Earth-facing part of the shower propagates in a part of the atmosphere that is denser than the part of the cone facing away from Earth, which may lead to increased production of mesons and therefore leptons. The net effect of this mirroring method and the distributions of α and h are presented in detail in Section 5.6.

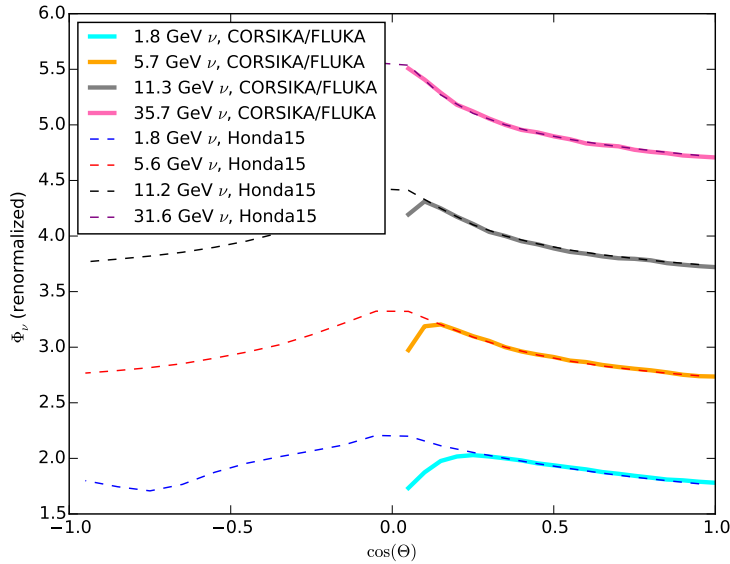


Figure 3.3.6.: Zenith distribution of the neutrino flux of unmodified CORSIKA compared with Honda results [57]. The fluxes have been normalized to the same value at $\cos \theta = 0.5$. There is a clear deficit for horizontal fluxes, which increases toward lower energies. Above 30 GeV the FLUKA zenith distribution agrees with the Honda data.

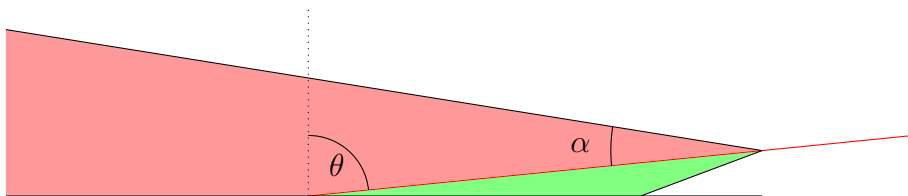


Figure 3.3.7.: Illustration of new weighting scheme

Schematic of the new weighting scheme, particles in the red shaded region are discarded, particles in the green shaded region receive a weight $w = 2$. In this schematic the angles $\theta \approx 85^\circ$, $\alpha \approx 15^\circ$ correspond to leptons with the lowest energies considered in this simulation ≈ 2 GeV.

4. Method: Implementation and Execution

The simulation of the hadronic interactions of CR particles inside the Earth's atmosphere is carried out using CORSIKA [44] (version 7.4003), a program originally developed for the KASKADE experiment. CORSIKA uses a test-particle approach, i.e. individual CR particles are tracked on their trajectory through the atmosphere as they interact with other particles, thereby producing mesons and baryonic resonances. Those particles decay and in turn produce leptons that can be observed on the Earth's surface. The probabilities of particle interactions in CORSIKA are handled by several different interaction models, any given run can use two different interaction models for different energy ranges.

In general this work follows the approach of Fedynitch et al. [2], however some modifications were made because a different energy range is considered. As the standard CORSIKA binary output tends to produce very large files when all secondary particles from several thousand showers are written to the output, it has been replaced by a complete rewrite of the COAST output routine, specifically the ROOTOUT option. This new version produces ROOT histograms, instead of outputting individual particles. This version of COAST was designed and originally implemented by Fedynitch et al., but there are considerable changes made in this work: First of all, the identification of the mother particle has been adapted to use the CORSIKA EHIST option instead of the HADGEN parameter. This offers a more reliable and versatile identification of the mother particle, which is necessary, because the version based on HADGEN could not identify neutrinos from muon decay. This change also makes it easier to separate the contribution from unflavored mesons. In addition to that, several new histograms have been added to the output to account for the geometry of the shower.

The use of CORSIKA in this work differs from the default in another aspect: instead of sampling primary particles from a distribution of primary energies E_{CR} and different nuclei ${}^A_Z X$, each run in this simulation uses a single fixed primary energy and nucleus, as well as a fixed zenith angle θ and azimuth angle ϕ . This makes it possible to estimate the time to simulate a certain number of showers and optimize energy cuts to reduce the necessary CPU time while keeping the most significant information intact. This method also makes it easy to simulate enough primary particles in any given energy range to achieve sufficient statistical accuracy, independent of the steepness of the E_{CR} spectrum. The output from all CORSIKA runs is then combined with weights corresponding to the primary CR flux to calculate the flux of atmospheric leptons. The changes to CORSIKA and details of the simulation are discussed in this chapter.

4.1. CORSIKA Output

The modified version of COAST, the CORSIKA ROOT output routine, produces yields, i.e. one-dimensional histograms of the energy distribution of the secondary particles created in a CORSIKA run. Individual yields are created for each kind of lepton – ν_e , $\bar{\nu}_e$, ν_μ , $\bar{\nu}_\mu$, μ^+ , and μ^- – and for each class of parent meson, K , π , charm (mostly D mesons), and unflavored (η , ρ^0 , ω). As the unflavored mesons generally don't decay into neutrinos, the corresponding yields are omitted. There are, however, yields for neutrinos produced from decaying muons. All yields are further sorted by primary energy E_{CR} , zenith angle θ and the primary nucleus ${}^A_Z X$. The notation for yields used in this work is

$$Y_{\text{parent} \rightarrow \text{lepton}}(E_{\text{CR}}, \theta, X). \quad (4.1)$$

The parent of the lepton is determined from the EHIST option in CORSIKA, this allows for a more precise distinction between parent particles, in particular neutrinos produced from meson decays as opposed to neutrinos from muon decay. CORSIKA's EHIST option had to be extended from muons to neutrinos, as the neutrino version was not yet available in version 7.4003, which is used in this work. The necessary modifications to the CORSIKA code were generously provided by Jakob van Santen [private communication]. One drawback here is that neutrinos from muon decay are listed with the meson that produced the decayed muon as their parent. For example, if a meson decays into a ν_μ and μ^+ which in turn decays into $e^+ + \nu_e + \bar{\nu}_\mu$, all three neutrinos would be listed with the same parent meson. So in order to assign the correct parent, the modified version of COAST keeps track of the most recently decayed muon and uses the charge of the muon to infer whether the neutrino was produced in the meson decay or the muon decay.

Fedynitch et al. used the HADGEN parameter instead of the EHIST option, which does not allow to distinguish between neutrinos from meson decay and those from the subsequent decay of the muon. For example in the chain decay of $\pi^+ \rightarrow \mu^+ \nu_\mu \rightarrow e^+ \nu_e \nu_\mu \bar{\nu}_\mu$ all resulting neutrinos would have been counted as produced in pion decay [2]. The yields for ν_e and $\bar{\nu}_e$ from pion decay are kept to maintain compatibility, even though pions do not directly decay into electron neutrinos. The energy binning of the yields covers the range from 1 GeV to 10 PeV with ten bins per decade, above 100 GeV it is identical to the binning used by Fedynitch et al., to allow for direct comparison.

In addition to the yields there are also 2D histograms representative of the shower geometry, recording the height h at which a particle was produced, and the opening angle α between the trajectory of the secondary particle and the trajectory of the primary CR particle. These histograms use the same energy binning as the yields, to allow for easy post-processing. However, the maximum energy in the histograms of α was limited to 10 TeV, as particles above that energy are always parallel to the shower axis. As there are no expected differences in production height depending on charge or flavor, neutrinos and their corresponding anti-neutrinos are stored in the same histogram, the same goes for μ^+ and μ^- . The production height histograms use a binning of 1 km wide bins, up to 100 km maximum height. The histograms of α cover the range from 0° to 90° in 50 bins. As even 1 GeV muons still have a Lorentz boost factor of almost 10 in the direction of the CR axis, they are not emitted perpendicular to the shower axis, and angles above

50° are rare outliers. Therefore, the binning was chosen to be equidistant in $\sin(\alpha)$, meaning that the bins are smaller for almost parallel angles, and very wide at larger angles.

4.2. Simulation Parameters

This simulation relies primarily on the FLUKA interaction model, which is described in [46]. While nominally used as a low-energy interaction model in CORSIKA, FLUKA has been used previously in simulations of primary particles of up to TeV energies [47]. The HILOW parameter in CORSIKA allows to set the energy at which CORSIKA switches from the high-energy interaction model to the low-energy model. In this simulation it is set to an energy of 100.1 TeV, slightly above the highest E_{CR} of 100 TeV to make sure that all runs use FLUKA exclusively. For comparison, the simulation also uses EPOS (in the version tuned for LHC results) [48] as the high-energy model and UrQMD [51] for the low-energy part, with a HILOW setting of 50 GeV. Electromagnetic interactions were switched off, focusing on the hadronic part only. The only primary particles considered were protons and neutrons, heavier nuclei will be represented using the superposition approach. The energy range covered in this simulation ranges from 1 GeV to 100 TeV with ten energy bins per power of ten. The primary energies below 5 GeV were omitted because they produced so few secondary particles as to be irrelevant. The energy cuts (ECUTS) at which CORSIKA discards secondary particles were set to $E_{\text{CR}}/1000$ (or 0.6 GeV, whichever was higher) to make sure that a sufficient energy range is covered, while minimizing CPU time spend on high-multiplicity, low-significance secondaries. See Section 3.2.1 for a more detailed discussion.

The zenith range only covered down-going showers, from $\theta = 0^\circ$ to $\theta = 90^\circ$. The binning was chosen to be equidistant in $\cos(\theta)$, covering the range from 1 to 0 in 0.05 increments, for a total of 21 zenith bins. This binning was chosen because the zenith dependence of the flux is approximately $\Phi(\theta) \propto 1/\cos(\theta)$. The binning also ensures that the distance between the point at which the primary particle enters the atmosphere and the center of the CORSIKA observation plane differs by less than 15 % between different zenith bins. For all but the last 4 horizontal bins it differs by less than 10 %. The difference of the pathlength $\Delta L/L$ from the center to the boundaries of a zenith bin is shown in Fig. 4.2.1. This means that the atmospheric density profile sampled in each bin does not differ too much, making it possible to reliably interpolate the flux between different bins if necessary and possibly introduce corrections for the 3D effects. Only one atmosphere model was used in this work, the US standard atmosphere (USSA). For each permutation of E_{CR} , $\cos(\theta)$, and primary particle 50000 showers were simulated. All the parameters of the simulation have been summarized in Table 4.1.

4. Method: Implementation and Execution

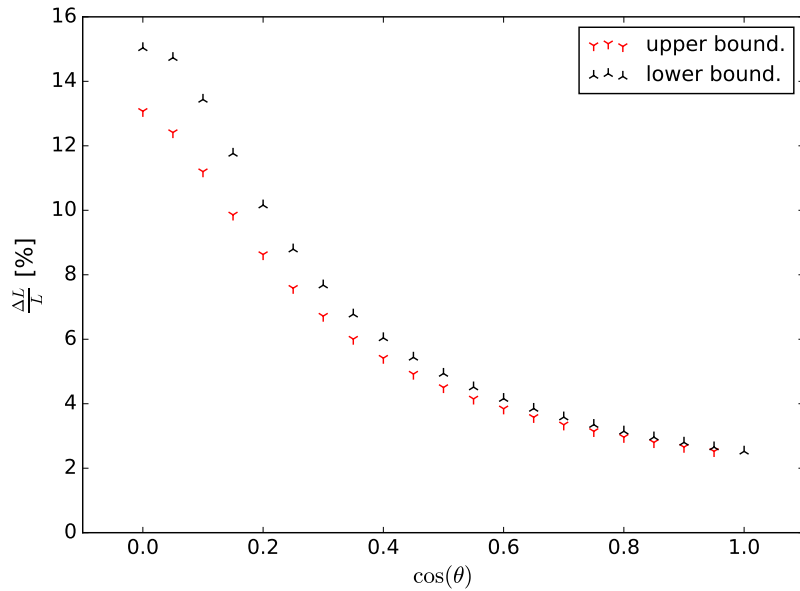


Figure 4.2.1.: Relative difference of the pathlength $\Delta L/L$ from the center to the boundaries of a zenith bin. The upper boundary of a bin corresponds to more vertical directions. As the pathlength increases toward the horizon, so does ΔL .

Interaction Model	EPOS + UrQMD, FLUKA
Atmosphere Model	USSA
$\cos(\theta)$	0 to 1 in 0.05 increments
Primary particle	H, n
Leptons	$\mu^+, \mu^-, \nu_\mu, \bar{\nu}_\mu, \nu_e, \bar{\nu}_e$
Parent Particles	π, K, μ , unflavored (η, ω, ρ^0)
E_{CR}	5.18 GeV to 100 TeV at ten bins per decade

Table 4.1.: Summary of the simulation parameters.

4.3. LiDong Cluster

The CORSIKA simulation runs were carried out on the LiDong cluster at the TU Dortmund. The LiDong cluster has 432 nodes with 3584 CPU cores in total, 256 of those nodes are so-called standard nodes with a 3 GHz Quad-Core CPU and 16 GB of memory. An overview of the different types of nodes in LiDO is shown in Fig. 4.3.1. This simulation was carried out on standard nodes exclusively.

As the FLUKA interaction model is considerably faster than EPOS, the simulation runs had to be distributed differently. 50000 showers can be simulated with FLUKA inside the 8 hour time frame allotted by a job on the medium queue at LiDong even at the highest energies simulated. As the runtime increases with E_{CR} , each FLUKA job contained four CORSIKA runs picked from the upper end of the simulated energy range, and four from the lower end. The four long runs were executed in parallel, followed by the four short runs. For EPOS the runs had to be split amongst more jobs, with four parallel CORSIKA runs at 25000 showers each. In total 90.3 million showers were simulated with each interaction model. The FLUKA simulation was done in about 400 CPUhours at 3 GHz, whereas the EPOS simulation required about 6200 CPUhours.

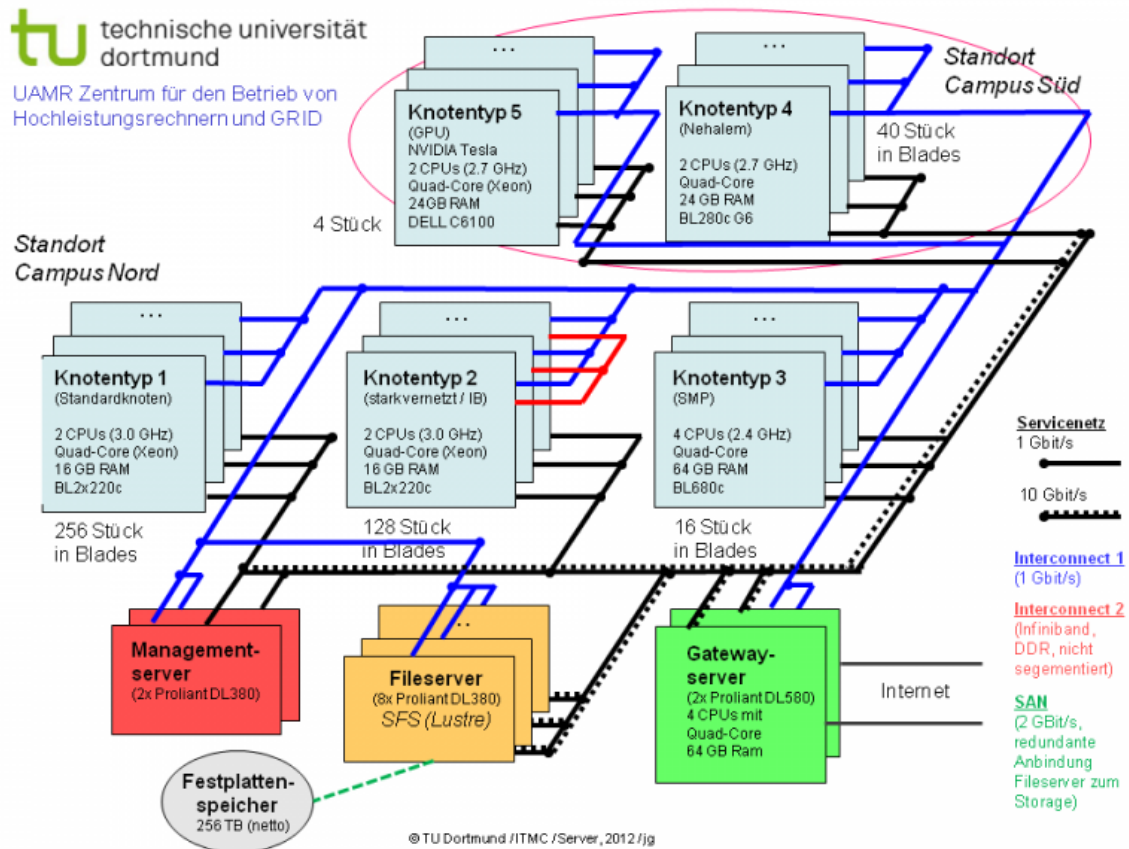


Figure 4.3.1.: Overview of the different types of nodes of the LiDong cluster [58].

4.4. Post-processing

After all CORSIKA simulation runs had finished, the resulting ROOT files were aggregated into a single file and sorted into a tree-like structure, according to the parameters of the simulation run. Histograms with identical parameter sets were summed up. This structure was then converted into a python dictionary for ease of use, with every ROOT histogram converted to a custom python histogram class. The structure of the dictionary is illustrated in Fig. 4.4.1. At the top level of the hierarchy are the different interaction models, followed by the atmosphere model and zenith angle (in $\cos(\theta)$). The dictionary is further subdivided by the primary particle, and the different permutation of leptons and their parents, e.g. ν_μ from π or ν_e from μ . For each of those different observables, the yield histograms are stored according to the energy of the primary particle.

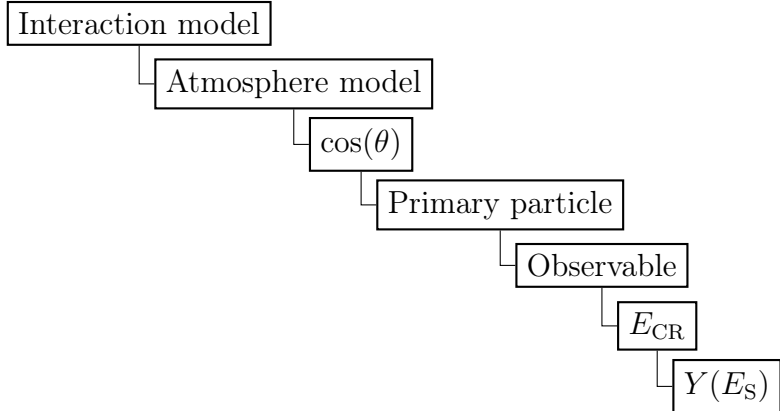


Figure 4.4.1.: Schematic of yield storage tree structure.

This granularity of stored data allows to systematically probe the details of different models. For example, separating the contribution from kaons and pions allows to study the uncertainties in the respective cross sections, which cannot be observed directly in air showers, but are nonetheless an important factor for the spectral shape of lepton fluxes. Moreover, this method of storage means that for every secondary particle the energy, type, and direction of the primary particle are implicitly known, so it is possible to invert the yield histograms, and obtain the contribution from different primary energies to a given secondary energy, according to any possible model of the primary flux.

To calculate the flux Φ_S of secondary particles, the dictionary has to be traversed and all relevant yields summed up, weighted according to the spectrum of primary particles:

$$\Phi_S(E_S, \Theta, \Phi_{CR}) = \sum_{Z_j} \sum_{E_{CR}} \sum_{m_K} w(E_{CR}, \Phi_{CR}(Z_j)) \times Y_{m_K \rightarrow S}(E_S, \Theta, E_{CR}, Z_j) \quad (4.2)$$

here m_K stands for the parent particle, Z_j for the different primary nuclei and Φ_{CR} for the corresponding primary flux. In case the superposition approximation is used, the fluxes CR nuclei have to be converted to the corresponding nucleon flux for the

calculation of the weights w :

$$\begin{aligned}\Phi_S(E_S, \Theta, \Phi_{CR}) = & \sum_{n/p} \sum_{E_{CR}} \sum_{m_K} w(E_{CR}, [\sum_{Z_j} \Phi_{CR}(Z_j)]_{n/p}) \\ & \times Y_{m_K \rightarrow S}(E_S, \Theta, E_{CR}, n/p).\end{aligned}\quad (4.3)$$

In addition to the fluxes, it is also possible to calculate the transfer function, i.e. a histogram of the contributions of different CR energies E_{CR} to the flux at a specific lepton energy E_S . Because these histograms are not stored explicitly, calculating them is more time intensive than calculating the flux. To evaluate the transfer function for a single value of the energy E_S the entire dictionary of yields needs to be traversed. For every yield histogram $Y_{m_K \rightarrow S}(E_S, E_{CR})$, the value of the yield at E_S needs to be stored in a tuple together with the value of E_{CR} associated with this histogram $(E_{CR}, Y(E_S, E_{CR}) \cdot w(E_{CR}))$. The histogram of all these tuples corresponds to the transfer function at a given energy E_S .

As the full collection of 2D histograms for production height and opening angle would be prohibitive to hold in memory at once, only the average and standard deviation are stored in 1D histograms. The structure of the corresponding dictionary is very similar, except that the distinction between particle and antiparticle has been dropped for the observables. This is only used for plotting purposes, for the calculation of the oscillation weights the 2D histograms are used.

4.4.1. Calculation of CR flux weights

Calculating the CR weight associated with a yield $Y(E_S, E_{CR})$ and the resulting contribution to the secondary flux requires to normalize the yield with the number N_{sim} of simulated primary CR particles and then multiplying it by the weight factor $w(E_{CR})$:

$$\phi(E_S) = \frac{dN}{dE_S} = \overbrace{\frac{Y(E_S, E_{CR})}{N(E_S)}}^{\Delta E_S} s_A \frac{1}{N_{sim}} \overbrace{\int_{E_0}^{E_1} \Phi(E_{CR}) dE_{CR}}^{w(E_{CR})}.\quad (4.4)$$

The surface scaling factor s_A is necessary to correct for the difference in area between the top of the atmosphere relative to area of the detector at surface [50]. The value used in this work of $s_A \approx 1.018$ is the same as used by Fedynitch et al. [2]. Technically s_A would be part of the weight w , but it is omitted in the following for brevity. The weight factor $w(E_{CR})$ corresponds to the number of CR particles in a certain energy range $\Delta E = E_1 - E_0$, which can easily be verified by inserting the definition of the differential CR flux $\Phi(E_{CR}) = dN_{CR}/dE_{CR}$ and invoking the mean value theorem:

$$\int_{E_0}^{E_1} \Phi(E_{CR}) dE_{CR} = \left\langle \frac{dN_{CR}}{dE_{CR}} \right\rangle \Delta E_{CR},\quad (4.5)$$

4. Method: Implementation and Execution

where $\langle dN_{\text{CR}}/dE_{\text{CR}} \rangle$ denotes the mean CR flux in the given energy range. Substituting this expression back into equation 4.4 gives the correct dimensions for a differential flux:

$$\underbrace{\frac{dN}{dE_S}}_{[E]^{-1}} = \underbrace{\frac{N(E_S)}{\Delta E_S}}_{[E]^{-1}} \frac{1}{N_{\text{sim}}} \underbrace{\left\langle \frac{dN_{\text{CR}}}{dE_{\text{CR}}} \right\rangle}_{[E]^{-1}} \underbrace{\Delta E_{\text{CR}}}_{[E]}. \quad (4.6)$$

For practical purposes, the weights are calculated by integrating numerically over the flux as described by one of the CR models for every primary CR energy bin. The boundaries of the integral E_0 and E_1 are chosen to coincide with the bin boundaries. The same weights are used for the fluxes of muons and neutrinos, and all related quantities, e.g. charge ratios or flavor ratios. Because of this, the weights associated with a selection of CR models are pre-calculated and stored in a table, instead of calculating the weights on the fly. For use with the superposition approximation, the CR flux $\Phi(E_{\text{CR}})$ of CR nuclei is replaced with the nucleon flux as described in Section 3.1.1.

4.4.2. Oscillation Weights

Neutrino oscillations can be added to the fluxes as well. In order to do so, the oscillation probabilities need to be provided by an external program. The oscillation probabilities need to be calculated for all different zenith angles and neutrino energies, as well as for all production heights. The calculations are done using NuSQuIDS [59], although any program could be used, provided it can generate tables of the probabilities for all given parameters. NuSQuIDS uses the Quantum Integro-Differential Solver (SQuIDS) [60] to solve the Schrödinger equation numerically in the interaction base and includes treatment of matter effects as well.

To calculate the oscillation weights w for the flux, the oscillation probabilities p for a given neutrino energy need to be averaged using the distribution of the neutrino production height h as weights:

$$w_{(m_k \rightarrow \nu_S \rightarrow \nu_j)}(E_S) = \sum_j p_{\nu_S \rightarrow \nu_j}(h_j, E_S) \frac{n_{(m_k \rightarrow \nu_S)}(h_j, E_S)}{N(E_S)}, \quad (4.7)$$

where $\frac{n_{(m_k \rightarrow \nu_S)}(h_j, E_S)}{N(E_S)}$ represents the fraction of neutrinos with energy E_S produced at a height h_j .

As the weighting process requires both time and considerable amounts of memory for the production height distributions, the oscillation probabilities are weighted beforehand, and only the resulting 1D oscillation weights are stored and loaded when needed. In order to facilitate this process the oscillation probabilities are calculated once for each zenith angle from $-1 \leq \cos(\theta) \leq 1$ in increments of 0.05. For each zenith angle and neutrino flavor the probabilities are stored in a 2D histogram with the same energy and production height binning used for the geometry histograms. An example of both types of histogram is shown in Fig. 4.4.2. Each of those histograms is treated as a matrix of

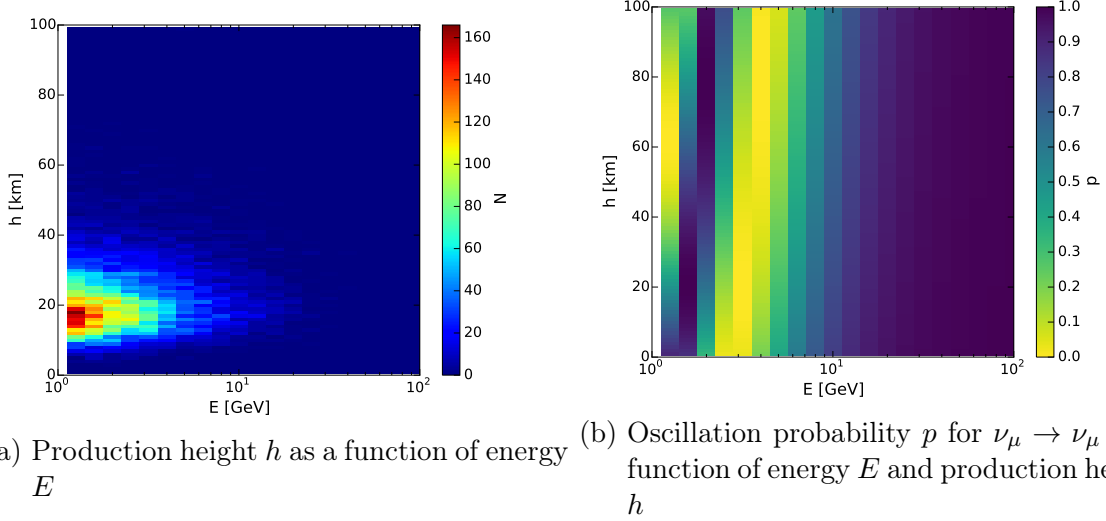


Figure 4.4.2.: Example distributions for the oscillation probability weighting scheme. The oscillation weight is calculated by averaging the oscillation probabilities in each energy bin, weighted according to the distribution of the production height.

column vectors:

$$P = \begin{pmatrix} \vec{p}_1 & \vec{p}_2 & \dots & \vec{p}_{-1} \end{pmatrix}$$

$$H = \begin{pmatrix} \vec{n}_1 & \vec{n}_2 & \dots & \vec{n}_{-1} \end{pmatrix},$$

with P representing the oscillation probabilities and H representing the histogram of production heights, and the components of the vector \vec{n} representing the bin contents of each column. The oscillation weights w_j correspond to the weighted average of the oscillation probabilities over the production height. The resulting 1D histogram of oscillation weights \vec{w} is calculated using

$$w_j = \frac{\vec{p}_j \cdot \vec{n}_j}{N_j},$$

with $N_j = \sum_i n_{ji}$, i.e. the sum of all the bin contents in the j -th column. The vectors containing the oscillation weights are calculated for all combinations of simulation parameters and stored in a dictionary of 1D histograms that mimics the structure of the yield dictionary, as shown in Fig. 4.4.1. As the energy binning for weights and yields is identical, applying the weights to a specific yield only requires to look up the corresponding weight histogram from the oscillation weight dictionary and multiply it with the yield component-wise. The resulting flux can then be calculated as described in

4. Method: Implementation and Execution

Section 4.4, modified with the oscillation weights as follows:

$$\begin{aligned}\Phi_{\nu_S \rightarrow \nu_j}(E_S, \Theta, \Phi_{\text{CR}}) = & \sum_{Z_j} \sum_{E_{\text{CR}}} \sum_{m_K} w(E_{\text{CR}}, \Phi_{\text{CR}}(Z_j)) \\ & \times w_{(m_k \rightarrow \nu_S \rightarrow \nu_j)} Y_{m_K \rightarrow S}(E_S, \Theta, E_{\text{CR}}, Z_j).\end{aligned}\quad (4.8)$$

5. Results

5.1. Selection of reference CR model

As discussed in Section 2.1.2, there have been several observations of CR fluxes above the pion production threshold, most recently the fluxes published by AMS, CREAM, and PAMELA. Recent CR models have been focused on the high-energy part of the spectrum. The former default model used within IceCube, h3a [4], was only valid for energies above 10 TeV, even the more recent GST model, calibrated using CREAM data, seems to leave room for another CR population in the energy range from 1 GeV to a few 100 GeV [7]. It would be possible to extrapolate the power-law description used in GST, but at energies below 50 GeV the CR spectrum deviates from a strict power-law behavior due to solar modulation. For this reason, h3a is not used in this work, and instead the older GH model [25] is used for comparison with GST. A comparison of both models with data points from CREAM, PAMELA, AMS and BESS is shown in Fig. 2.1.2. The GST model is in very good agreement with the CREAM data points, but fails to describe the shape of the spectrum below a few 100 GeV, while the GH model does match the general shape of the data, but does not agree with any particular dataset. In particular the helium flux lies below most of the data points.

To investigate the impact of the primary model on the systematic uncertainty, a modified version of the GST model is defined as well. The spectra reported by AMS and others are relatively smooth but can no longer be described by a simple power-law – as used in GST – due to the solar modulation. For the variant of GST developed in this work, the low-energy part of the spectrum is represented by a spline through the data points that replaces the GST proton flux at energies below 350 GeV. This method creates a discontinuity in the spectrum, which is undesirable in a model of the differential flux, however, for the weighting method used in this work only the integral flux over a specific CR energy bin or range is relevant. Thus the introduction of a small, finite discontinuity does not affect the results negatively. The spline interpolation also reproduces most of the statistical fluctuations in the experimental data, so it works better with the stronger regularization of the unfolded AMS spectrum.

This tuned model is shown in Fig. 5.1.1, compared to the unmodified GST model, and data from CREAM and AMS. The same approach is also used for BESS data, shown in Fig. 5.1.2. As BESS observed both CR fluxes at altitude and muon fluxes at surface level, this creates a unique opportunity to check the interaction model while minimizing the impact of the uncertainty due to the primary flux. While the fluctuations in the spline interpolation of the BESS flux may appear detrimental, the integral weights are not affected strongly and the resulting flux is relatively smooth. The muon flux for GH,

5. Results

unmodified GST and GST tuned to BESS CR data is shown in Fig. 5.1.3 compared to the fluxes measured by BESS, CAPRICE and L3+C. While the GH model still shows slightly better agreement at energies below 100 GeV, it does fall short of the L3+C data at higher energies. The unmodified GST model yields fluxes so far below the data that it is unsuitable for the energy range below 100 GeV. Because the focus of this work is on the low-energy part of the spectrum, the GH model is adopted as the default. While the modified GST version will be used for comparison when necessary, the unmodified version will be omitted. As soon as more recent measurements of the atmospheric muon flux become available, it would be prudent to reconsider the GST version tuned to AMS data.

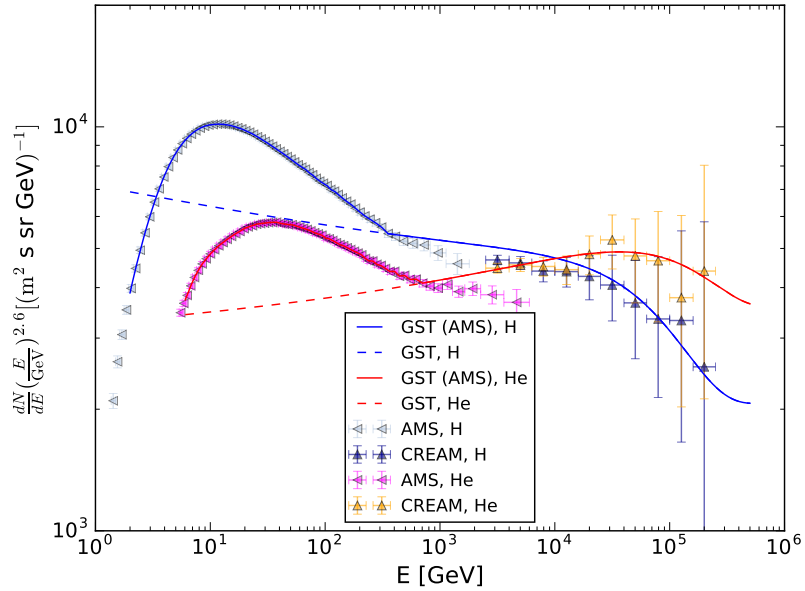


Figure 5.1.1.: GST model tuned to the AMS helium and proton spectra. Data taken from CREAM [9] and AMS [14, 15].

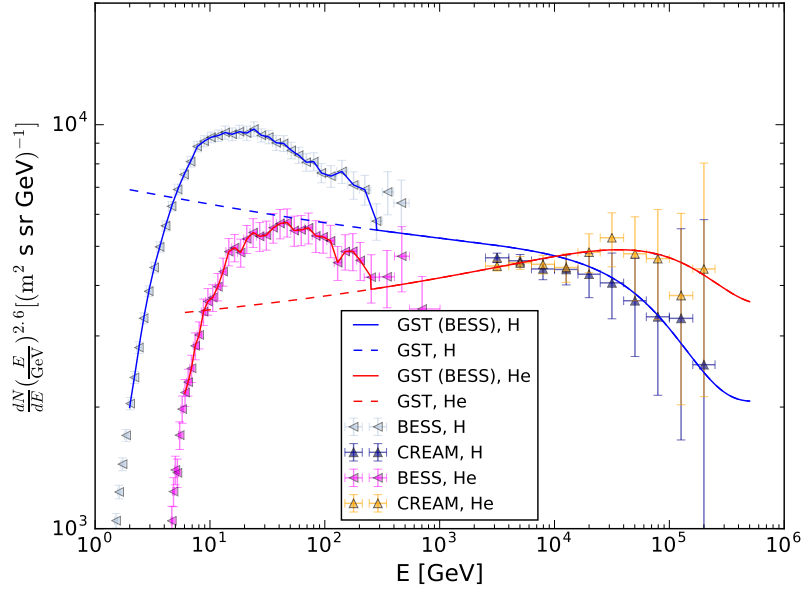


Figure 5.1.2.: GST model tuned to the BESS-TeV helium and proton spectra. Data taken from CREAM [9] and BESS [10].

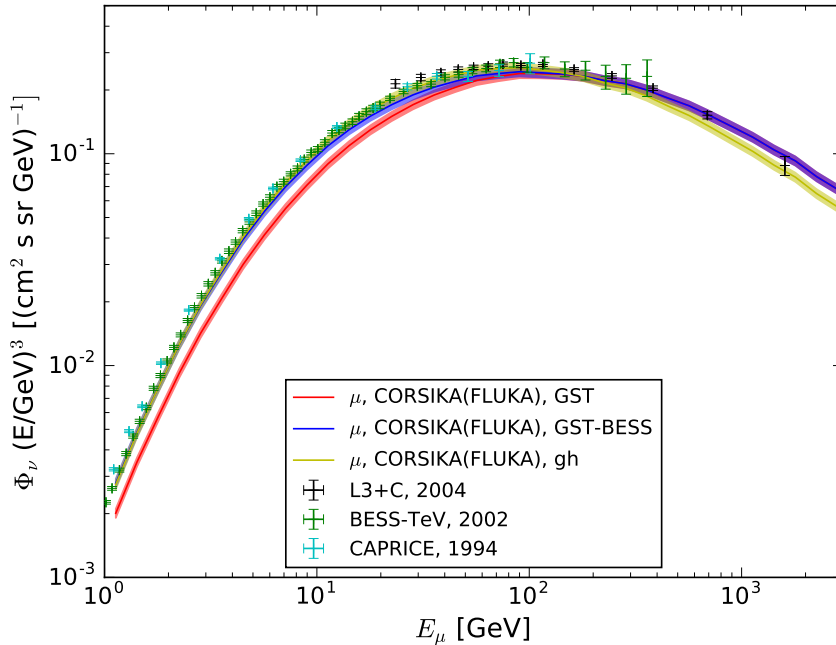


Figure 5.1.3.: Vertical muon flux obtained using FLUKA, with GST model tuned to BESS proton and helium fluxes, compared to GH and unmodified GST. Data points taken from BESS [10], CAPRICE [6] and L3+C [34].

5.2. Impact of interaction models in different energy ranges

The comparison of the different interaction models is not completely straightforward, as one dataset was obtained using FLUKA exclusively, but the other dataset uses EPOS and UrQMD with the HILOW parameter set to 50 GeV. This means that interactions with a projectile energy above 50 GeV are handled by EPOS, whereas those below that threshold are handled by UrQMD. It is possible that in a given shower, the initial CR particle has an energy above that threshold and is therefore handled by EPOS, but some or all of the secondary interactions fall below the threshold and are therefore treated by UrQMD. This makes it difficult to trace the boundary between the two interaction models. Obviously all secondary particles with an energy above 50 GeV are exclusively the result of EPOS, but those below that threshold are not exclusively UrQMD. Instead they are partly the result from cascades treated by both EPOS and UrQMD, while only those secondaries from primary particles with energies below 50 GeV are handled solely by UrQMD.

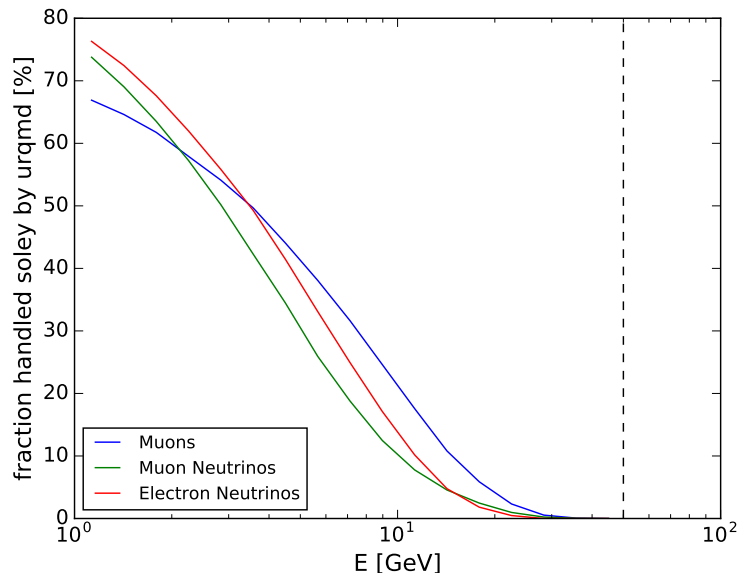


Figure 5.2.1.: Fraction of secondary particles from showers handled exclusively by UrQMD. All particles with energies above 50 GeV – indicated by the dashed line – are purely handled by EPOS. The area between the dashed line and any of the solid lines contains contributions from both interaction models.

The contribution from each interaction model can be quantified, the result is shown in Fig. 5.2.1. This plot has been created using the transfer function: For each secondary energy below 50 GeV the distribution of the contributing primary energies is calculated. All showers with primary energies below 50 GeV are handled solely by UrQMD, those

5.3. Comparison with observed fluxes

above can have contributions from both primary models. As shown in Fig. 5.2.1, the fraction of particles from showers handled exclusively by UrQMD never exceeds 80 % and is already below half at 10 GeV. Between 30 GeV and 50 GeV all secondary particles originate from showers that were treated by both EPOS and UrQMD. In the following sections the combination of EPOS + UrQMD will be labeled as EPOS because UrQMD only plays a subordinate role.

5.3. Comparison with observed fluxes

To verify that this simulation provides a consistent description of the spectra of atmospheric leptons, the fluxes obtained need to be compared with available data for muon and neutrino fluxes. Fig. 5.3.1 shows the muon fluxes for both EPOS and FLUKA using the GH primary model. In the region around 100 GeV EPOS consistently lies below the experimental data, whereas FLUKA agrees with the data. Toward lower energies the EPOS fluxes rise above the FLUKA prediction, possibly due to the influence of UrQMD. The fluxes of EPOS and FLUKA intersect at ≈ 10 GeV and the contribution of UrQMD to the muon flux rises from 20 % at 10 GeV to above 60 % at 1 GeV (see Fig. 5.2.1). This suggests that the cross-sections for pion production in UrQMD are larger than those in EPOS and FLUKA. Muon data are also available for μ^+ and μ^- separately, Fig. 5.3.2 shows this more detailed comparison, which suggests that the differences between EPOS and FLUKA are independent of the muon charge.

For neutrinos, shown in Fig. 5.3.3, the difference between FLUKA and EPOS is a lot less pronounced, together with the larger uncertainties of the observations this cannot be used to rule out either interaction model. Toward higher energies, both neutrino and muon fluxes seem to lie systematically below the observed fluxes, this is to be expected due to the limited range of primary CR energy, and will be discussed in Section 5.5. The muon deficit of EPOS and the differences between the two models will be discussed in more detail in the following sections.

To verify that not only the energy spectrum is described correctly, but the zenith dependence as well, the FLUKA muon fluxes are compared to the L3+C data as a function of $\cos(\theta)$. This is shown in Fig. 5.3.4 for different muon energies. L3+C does not cover the entire zenith range, and the energy binning of the simulation does not coincide with the binning chosen by the experiment, so only energies which correspond closely are shown. There is good agreement in both the normalization and the slope of the flux. From the results of the vertical flux (Fig. 5.3.1) it is already clear that the normalization of EPOS is too low. This can also be seen in Fig. 5.3.5, where the simulated flux lies systematically below the measured flux. However, the angular distribution appears consistent with the data.

In addition to the total fluxes, more fine grained information needs to be considered as well. While there are no experimental data available for distinct neutrino flavors, muons can be separated by their charge. Instead of individual fluxes, the muon charge ratio, i.e. the ratio between the flux of μ^+ and μ^- is shown in Fig. 5.3.6. As this was one of the major issues with the interaction models used by Fedynitch et al. [2], data from

5. Results

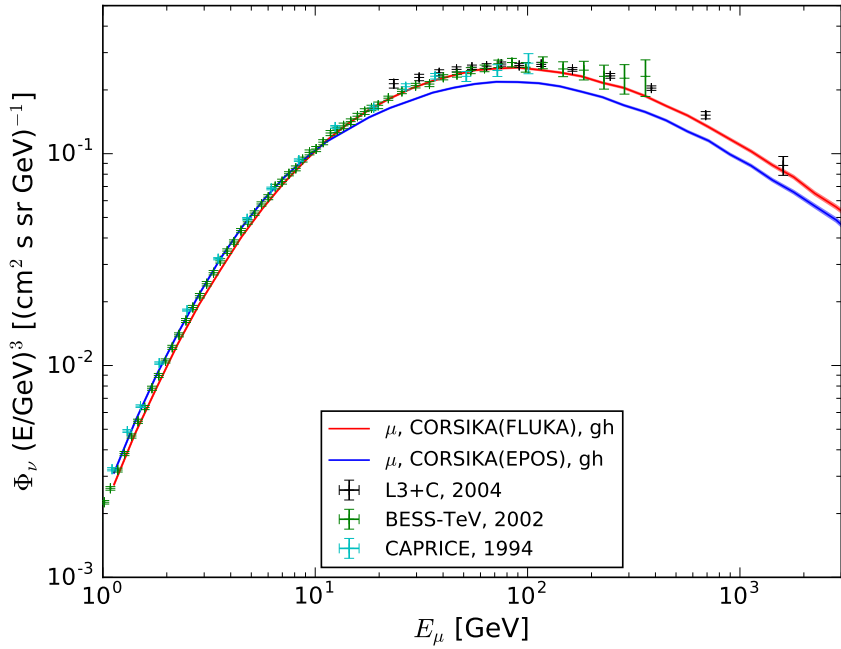


Figure 5.3.1.: Muon flux using EPOS and FLUKA with the GH primary model. Data points taken from L3+C [34], BESS [30], and CAPRICE [6]. The thickness of the lines corresponds to the statistical uncertainty of the flux.

this previous simulation is shown for comparison. It is immediately clear that neither simulations with SIBYLL-2.1 nor QGSJET-II (version 3) agree with the observed muon charge ratio. In the energy region around 100 GeV both EPOS and FLUKA show almost perfect agreement with L3+C data and the MINOS model. Toward lower energies both models exhibit a lower charge ratio with EPOS even further below FLUKA, possibly due to the influence of UrQMD. In the region between 1 TeV and 10 TeV the statistical uncertainties grow too large to determine which model fits better.

So far, all available data show good agreement with FLUKA and except for the muon fluxes also with EPOS. For a more detailed discussion of the systematic effects that influence this behavior, the available observations are no longer sufficient. Therefore the results need to be compared to simulated data, which allows to probe aspects that are not accessible to experiments, such as the flavor of neutrinos, or the parent mesons of the observed leptons.

5.3. Comparison with observed fluxes

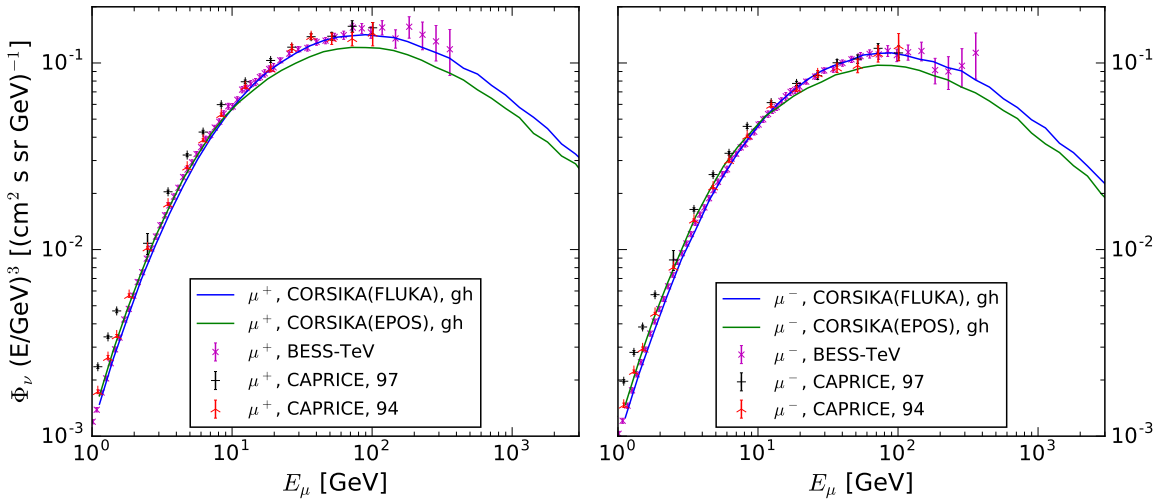


Figure 5.3.2.: Fluxes of μ^+ (left) and μ^- (right) using EPOS and FLUKA with the GH model. Data from BESS [30] and CAPRICE [6].

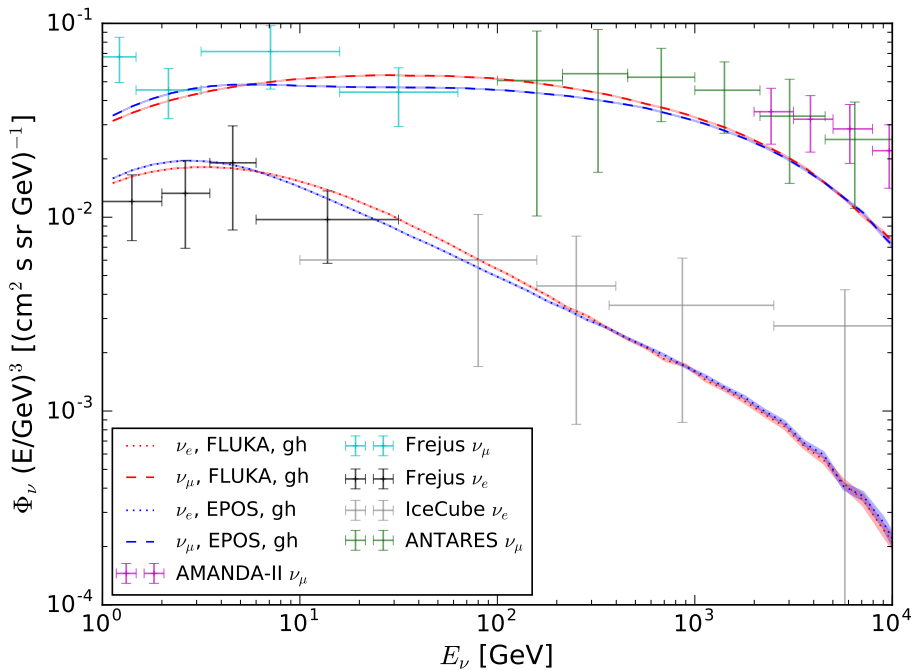


Figure 5.3.3.: Neutrino flux using EPOS and FLUKA with the GH model compared to measurements from Frejus [61], AMANDA [62], ANTARES [63], and IceCube [64].

5. Results

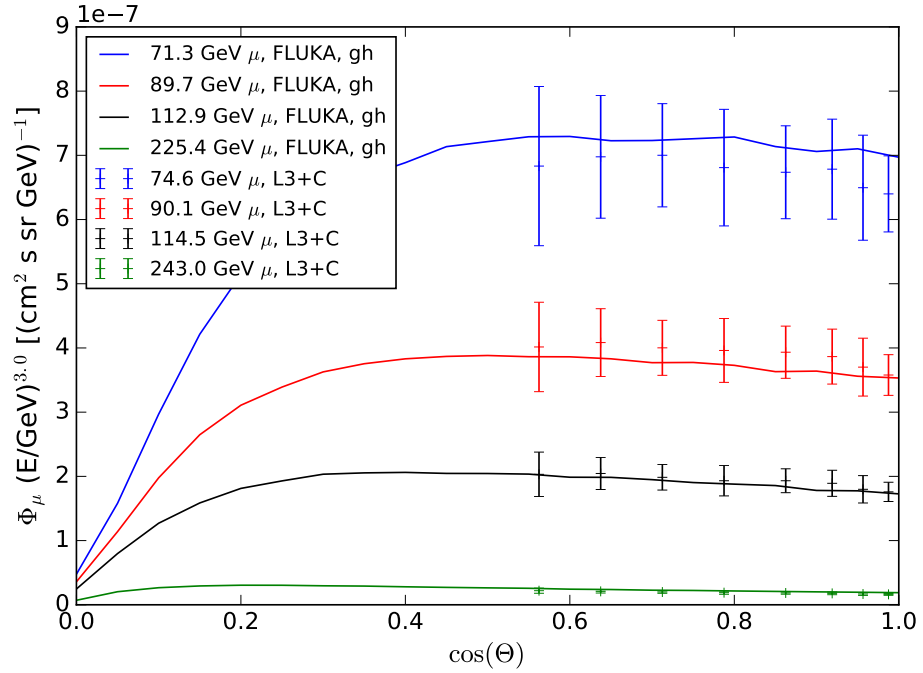


Figure 5.3.4.: Muon flux calculated with FLUKA and GH as a function of $\cos(\theta)$ for different muon energies compared to L3+C [34] data.

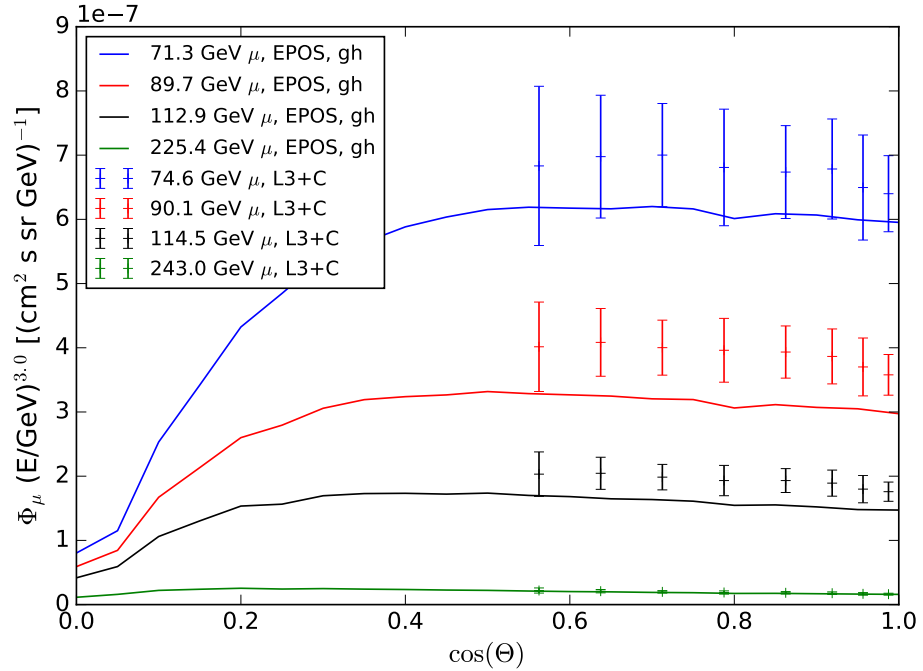


Figure 5.3.5.: Muon flux calculated with EPOS and GH as a function of $\cos(\theta)$ for different muon energies compared to L3+C [34] data.

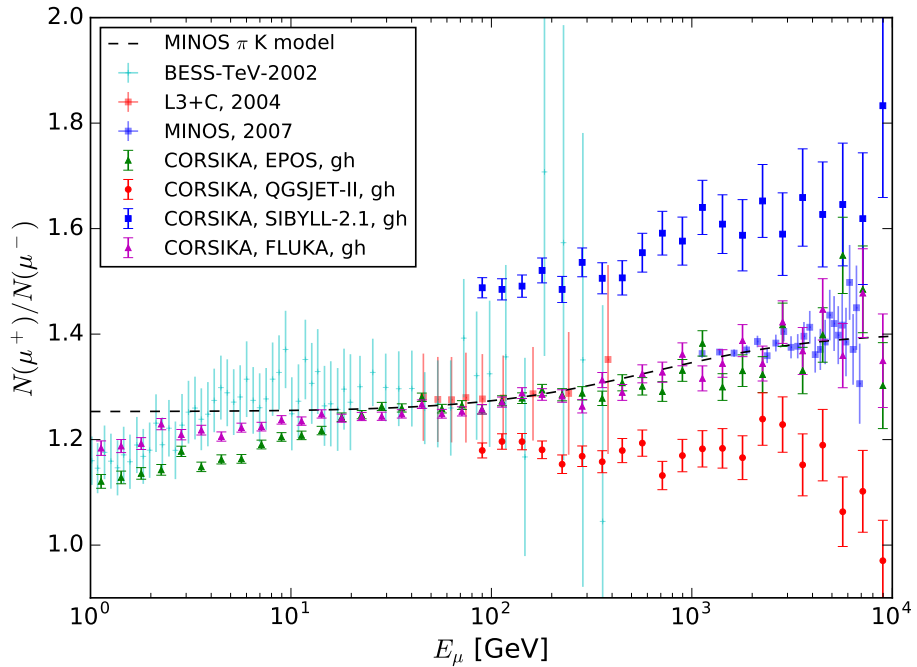


Figure 5.3.6.: Muon charge ratio according to simulation and experiment. FLUKA and EPOS data from this work, SIBYLL and QGSJET from [2], all weighted with GH. MINOS π K model and data points from [35], remaining data from BESS-TeV [30] and L3+C [34].

5.4. Comparison with simulation

5.4.1. EPOS vs. FLUKA

To further examine the differences between EPOS and FLUKA, the different contributions to the lepton flux need to be studied separately. As shown in Fig. 5.4.1, the two main sources of the lepton fluxes are kaons and pions. The decay of muons also contributes significantly to the neutrino fluxes, whereas the contribution of unflavored mesons to the muon flux is negligible, indistinguishable from 0 on a linear scale. Pions do not contribute directly to the flux of electron neutrinos at all, which is a good cross-check for the correct tagging of the parent particle using the CORSIKA EHIST option. For all leptons the relative contribution of kaon decay increases toward higher energies. Due to the higher critical energy of kaons, they interact with particles of the atmosphere less frequently than pions and their contribution starts to drop off at higher energies than the contribution of pions. See Section 2.2 and Section 2.4 for a more detailed description.

While pions dominate the muon flux over the entire energy range, the situation is more complicated for neutrinos. For electron neutrinos the flux is dominated by muon decays at low energies. However the energy at which the kaon and muon contributions are equal shifts from around 100 GeV for vertical showers to about 1 TeV for horizontal showers. This is due to the much longer baselines (about 100 km vs. 1000 km) that cause most muons from horizontal directions to decay, whereas vertical muons with the same energy have a chance to survive until they reach the surface. For muon neutrinos, the high-energy part is dominated by kaons, but the low-energy part depends on the direction: Vertical low-energy muon neutrinos are pion dominated, whereas the predominant source of horizontal muon neutrinos transitions from muons to pions and then to kaons as the neutrino energy increases.

For all leptons and arrival directions FLUKA shows a higher fraction of pions than EPOS does. Fig. 5.4.2 shows the relative difference between the muon fluxes for EPOS and FLUKA. It appears that EPOS produces about 20 % less pions than FLUKA does, independent of the pion charge. For kaons, the differences are more striking, while the K^+ flux does not differ much between the two interaction models, for K^- the difference increases with energy, up to about 60 %. This is surprising, as the models used in the simulation by Fedynitch et al. [2] differed mostly due to the Λ -associated K^+ production, which should not affect K^- . A similar picture emerges for the muon neutrino flux, shown in Fig. 5.4.3. However the resulting difference on the total flux is less pronounced, because the neutrino flux is not dominated by pions for the most part. It should be noted here that the EPOS-LHC version has been tuned to produce more muons from unflavored mesons, and indeed produces more than ten times as many muons from those mesons as FLUKA does, but at these relatively low energies the unflavored contribution is not sufficient to compensate for the deficit in pions. This is shown in Fig. 5.4.4.

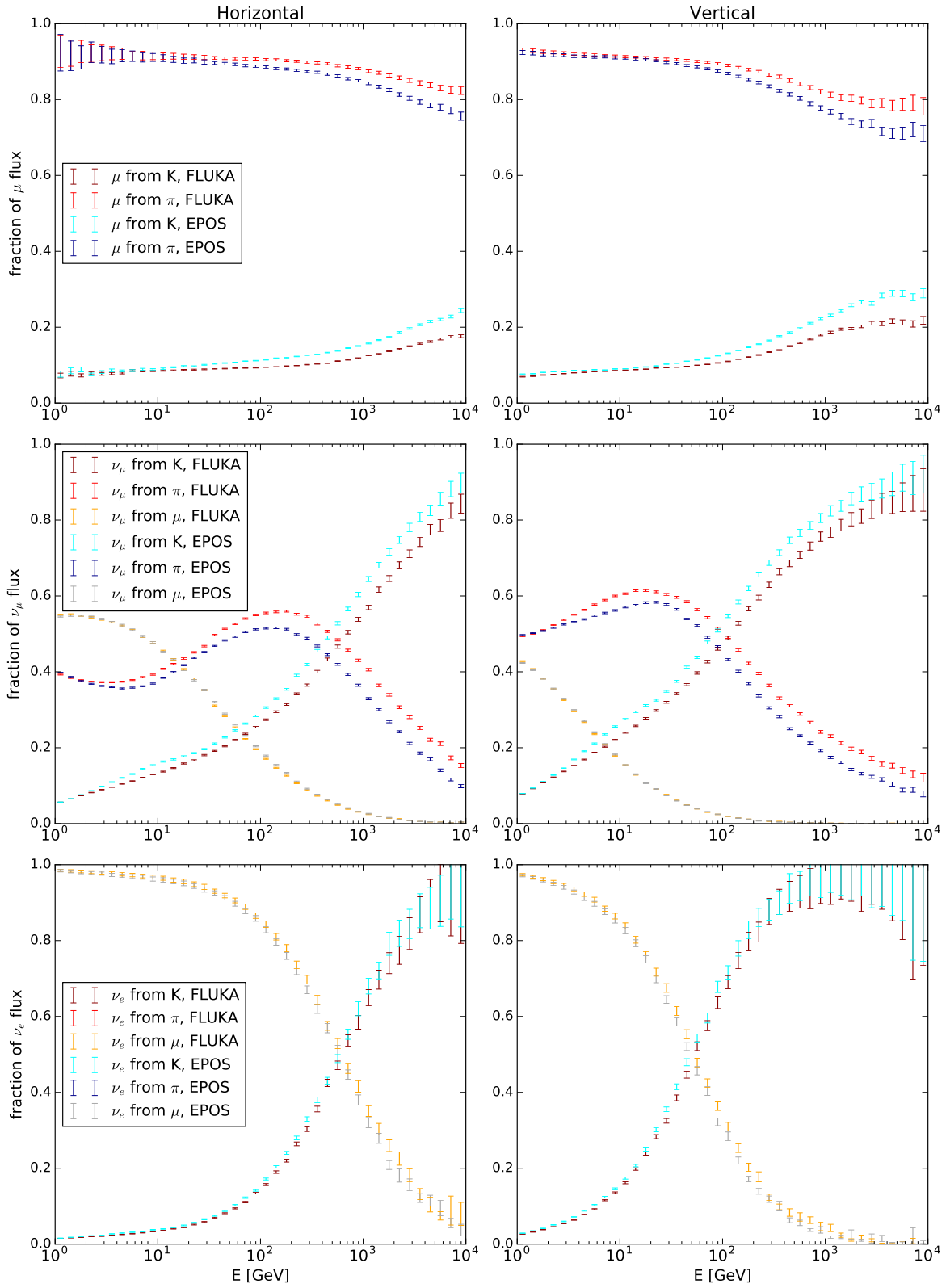


Figure 5.4.1.: Fraction of conventional flux by parent meson, horizontal flux on the left, vertical on the right. From top to bottom: Muons, muon neutrinos and electron neutrinos. Note that there is no expected contribution of pions to electron neutrinos, but the corresponding (empty) histograms are still included to verify the correctness of the tagging of the parent meson.

5. Results

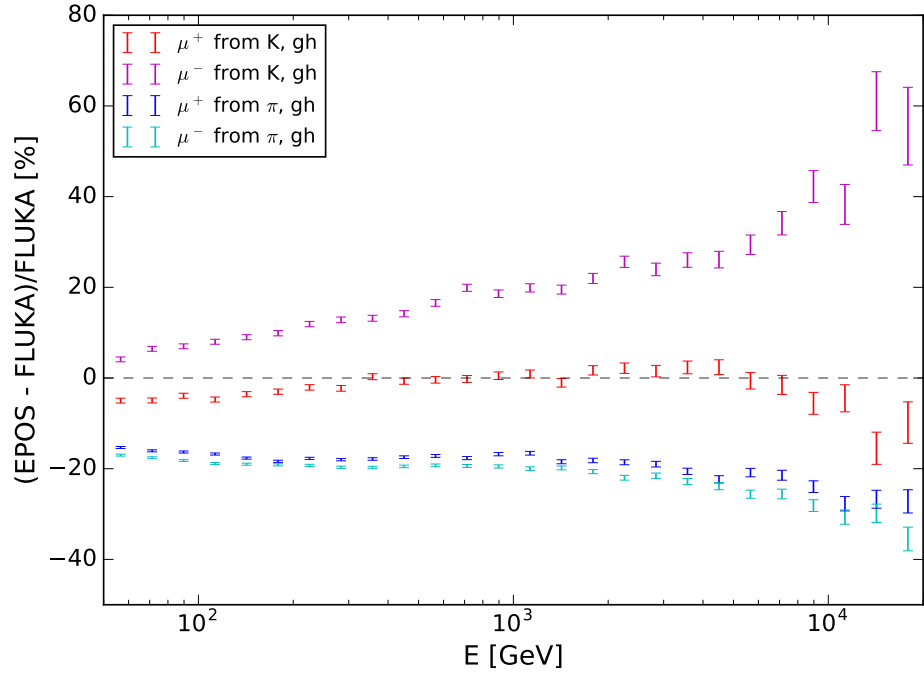


Figure 5.4.2.: Muon flux from kaons and pions, relative difference between EPOS and FLUKA. Note the large difference for μ^- compared to μ^+ .

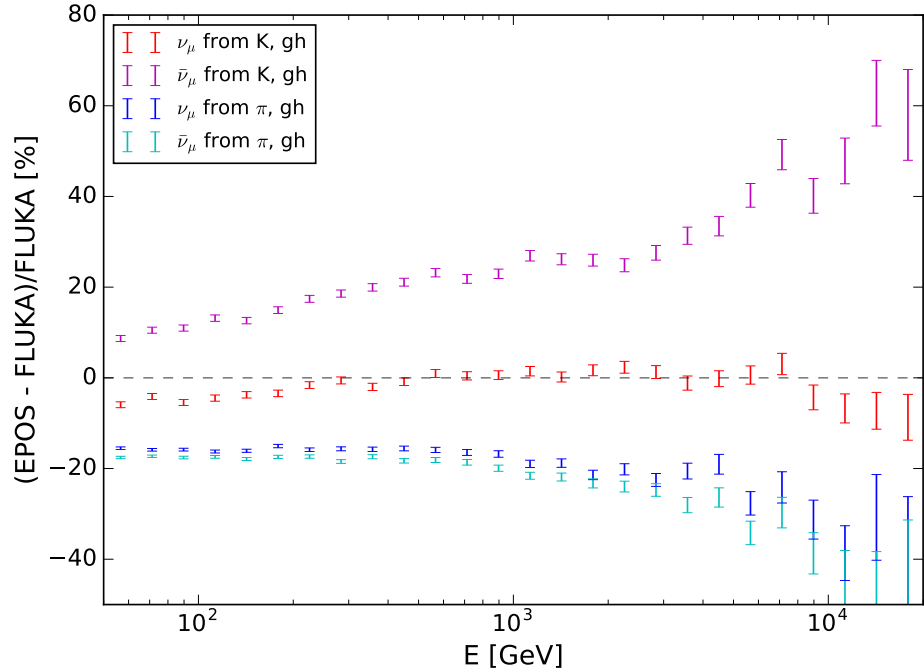


Figure 5.4.3.: Muon neutrino flux from kaons and pions, relative difference between EPOS and FLUKA.

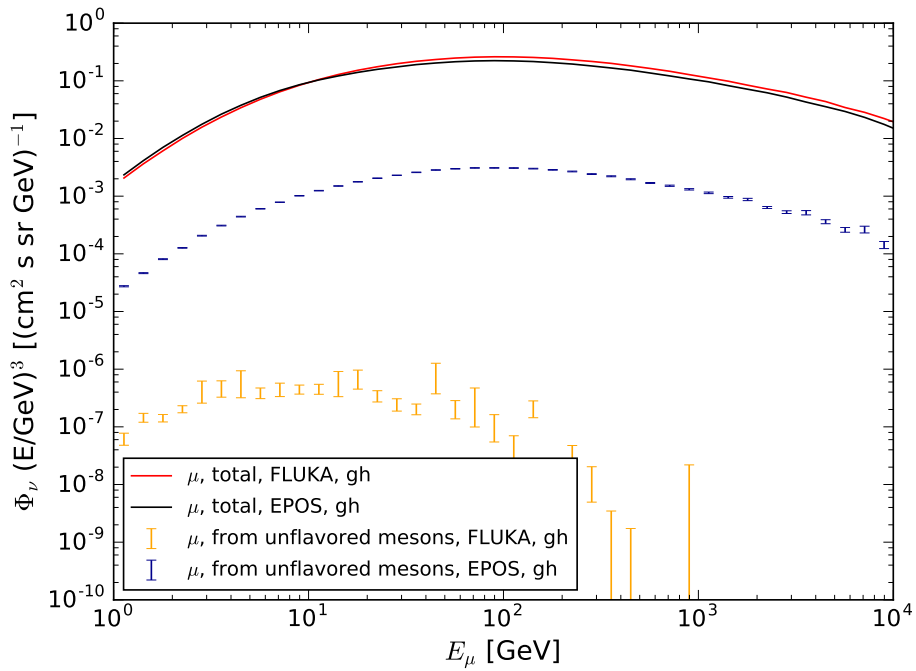


Figure 5.4.4.: Total muon flux and contribution from unflavored mesons. While the contribution to the total flux is negligible in this energy range, it can be seen that unflavored mesons are very rare in FLUKA and only efficiently sampled in EPOS.

5.4.2. Meson charge ratios

As most reference simulations do not explicitly state the relative strength of the contribution from kaons and pions, the only possible comparison is with the simulation by Fedynitch et al. Because of the different handling of neutrino parents, this comparison will be limited to muons. Fig. 5.4.5 show the charge ratio of kaons and pions, for EPOS and FLUKA as well as SIBYLL-2.1, QGSJET-II, and QGSJET01c. Both versions of QGSJET have almost flat kaon charge ratios, which suggests a lack of the Λ -associated K^+ production. Both EPOS and FLUKA show a rising trend in the charge ratios, whereas SIBYLL-2.1 has a flat charge ratio for pions and a steeply falling charge ratio for kaons. This contradiction is not easy to resolve, as FLUKA and EPOS results are affected by systematic errors in the energy range above 1 TeV due to the limited CR energy range of this simulation, although this error should affect both positively and negatively charged particles equally. As EPOS and FLUKA agree with the muon charge ratio much better than SIBYLL-2.1 does, this could also suggest that the treatment of kaons is not completely correct in SIBYLL-2.1.

The charge ratio of kaons and pions is not the only parameter that effects the muon charge ratio, but the ratio of pions to kaons has to be considered as well. The ratio of pions to kaons is shown in Fig. 5.4.6 for both muons and muon neutrinos. Here, the differences are not as pronounced as in the charge ratios. For muons SIBYLL-2.1 and EPOS seem to agree, however this is most likely a coincidence, as SIBYLL-2.1 yields the highest kaon fluxes of all the models, while EPOS yields the lowest pion fluxes. The fact that the kaon to pion ratios show generally similar trends for all models, while the charge ratios show opposite trends for SIBYLL-2.1 and FLUKA, demonstrates that the systematic uncertainty is not sufficiently described by either ratio.

5.4.3. Neutrino flavor ratios

While other simulations are generally not published with the contributions from kaons and pions available separately, their influence can still be compared indirectly. Muons predominantly originate from mesons with identical charge with a few exceptions due to the decay of unflavored mesons. Similarly, mesons with positive charge produce neutrinos, and mesons with negative charge produce anti-neutrinos. The mapping from neutrinos back to mesons is not as straightforward, due to the influence of neutrinos produced from muon decay, but the influence of the charge ratios of mesons can be seen here as well. As the fraction of K^+ to K^- increases, so should the ratio of ν_μ to $\bar{\nu}_\mu$.

The ratio of pions to kaons is reflected in the ratio of muon neutrinos to electron neutrinos, because muon decay always produces one neutrino of each generation, and pions decay exclusively into muon neutrinos. At the lowest energies this ratio approaches two, because virtually all muons decay, and therefore every charged meson contributes two muon and one electron neutrino in total. As energy increases so do the ratio of kaons to pions and the fraction of surviving muons. Muons contribute equally to electron and muon neutrinos, but about two thirds of kaons produce a muon and a muon neutrino. The direct decay of kaons into electron neutrinos is too small to compensate for the

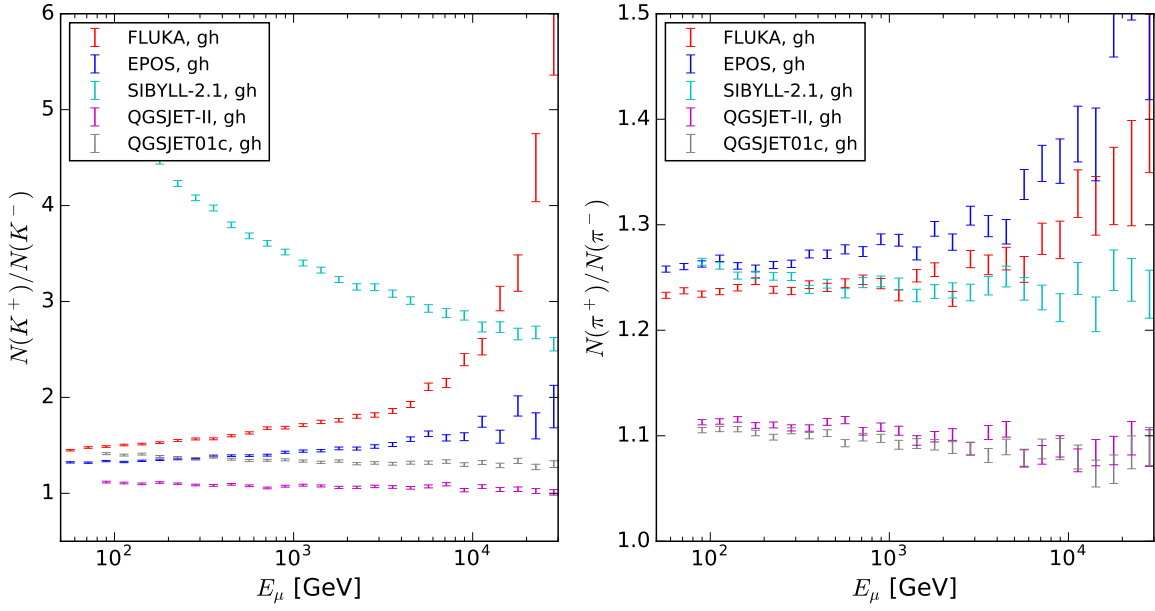


Figure 5.4.5.: Charge ratios of kaons (left) and pions (right), FLUKA and EPOS from this work, SIBYLL and QGSJET from [2].

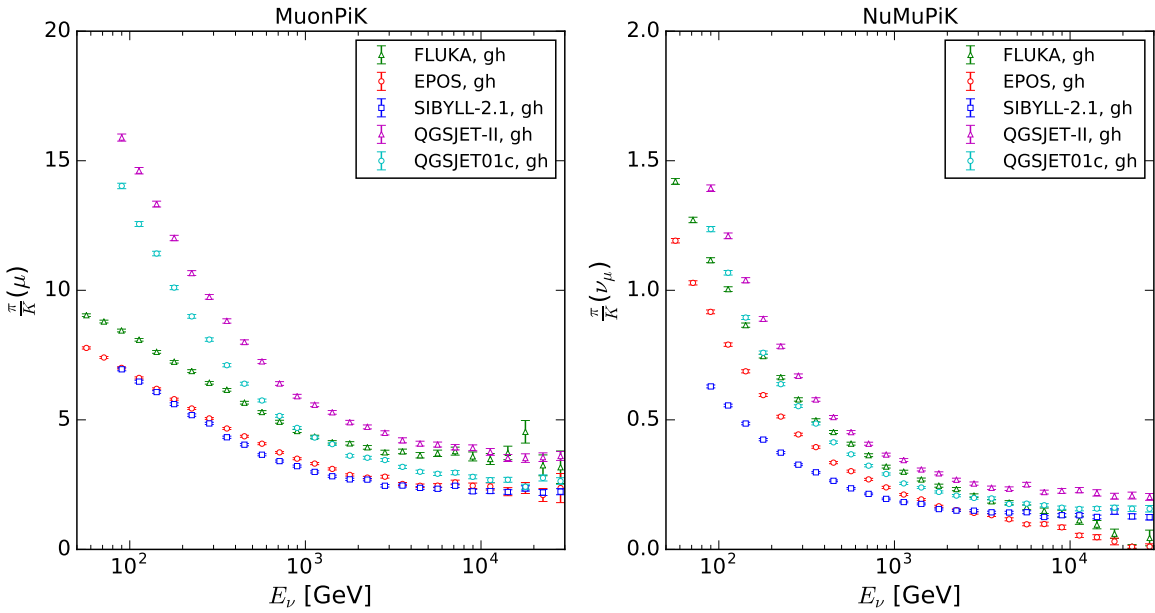


Figure 5.4.6.: Ratio of pions to kaons for muons (left) and muon neutrinos (right), FLUKA and EPOS from this work, SIBYLL and QGSJET from [2].

5. Results

reduction in muon decay, leading to a rising fraction of $(\nu_\mu + \bar{\nu}_\mu)/(\nu_e + \bar{\nu}_e)$.

Fig. 5.4.7 shows the ratio of muon neutrinos to electron neutrinos for FLUKA and EPOS compared to reference simulations from [2, 57]. At low energies FLUKA, EPOS, and the Honda simulation seem to be in good agreement, at higher energies EPOS starts to deviate from the other two. While SIBYLL-2.1 consistently predicts the highest ratio, both versions of QGSJET fall in between FLUKA and SIBYLL-2.1. The flavor ratios of $\nu_\mu/\bar{\nu}_\mu$ and $\nu_e/\bar{\nu}_e$ are shown in Fig. 5.4.8 and Fig. 5.4.9, respectively. For these flavor ratios the differences between interaction models are more pronounced than in Fig. 5.4.7. The ratios again reflect the kaon charge ratios, with SIBYLL-2.1 consistently producing the highest ratio of neutrinos to anti-neutrinos and both versions of QGSJET predicting very low and almost flat ratios. The ratios for FLUKA, EPOS and Honda are grouped more closely together and similar in shape. They exhibit a more steeply rising trend for FLUKA than for EPOS, with the Honda simulation in between the two interaction models. This trend is consistent with the difference in the K^- channel between EPOS and FLUKA, as $\bar{\nu}_\mu$ are mostly produced from K^- and with K^+ production almost equal, a higher fraction of $\nu_\mu/\bar{\nu}_\mu$ is to be expected. However, this is no proof of correctness for either model. While the muon data seems to be in better agreement with FLUKA, this is mostly due to the pion channel and does not constrain kaon production as tightly. The only way to study this matter in more detail is to resolve the statistical and systematic uncertainties of the muon charge ratios between 1 TeV and 10 TeV, which are more strongly influenced by kaons.

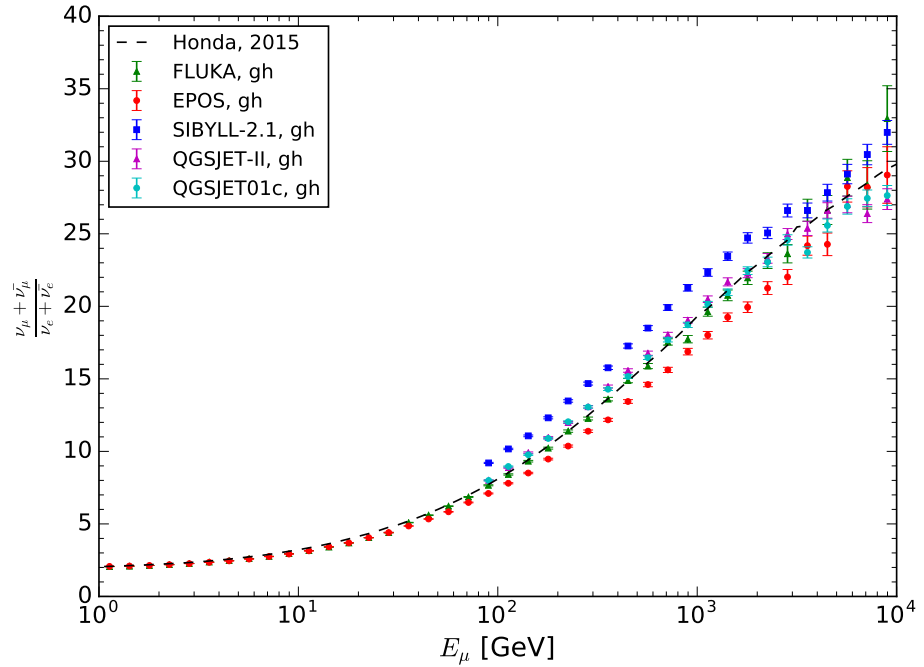


Figure 5.4.7.: Ratio of $\nu_\mu + \bar{\nu}_\mu$ to $\nu_e + \bar{\nu}_e$ for FLUKA and EPOS, as well as Honda [57], and the models used in [2].

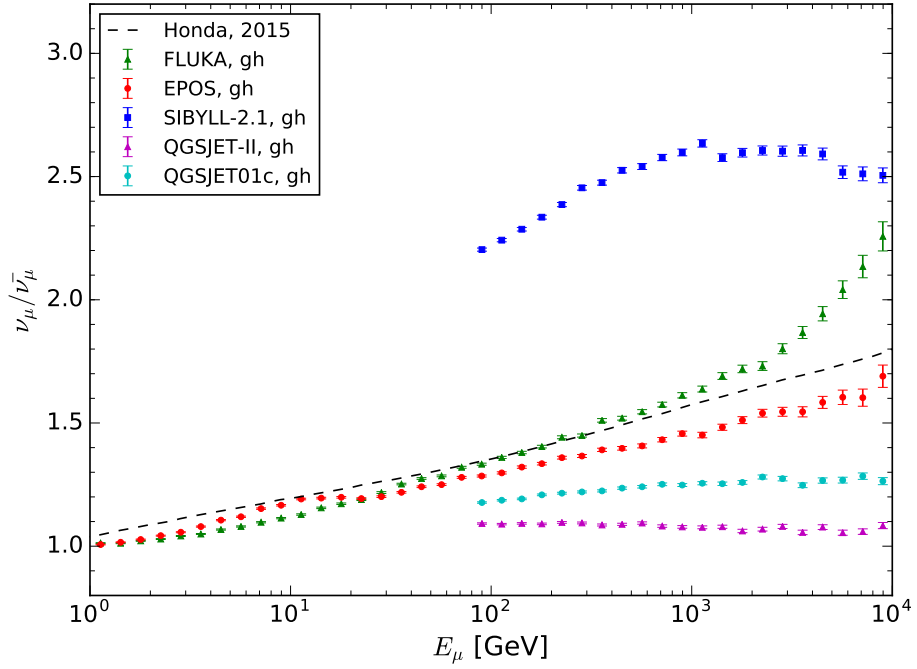


Figure 5.4.8.: Ratio of ν_μ to $\bar{\nu}_\mu$ for FLUKA and EPOS, as well as results from [57], and the models used in [2].

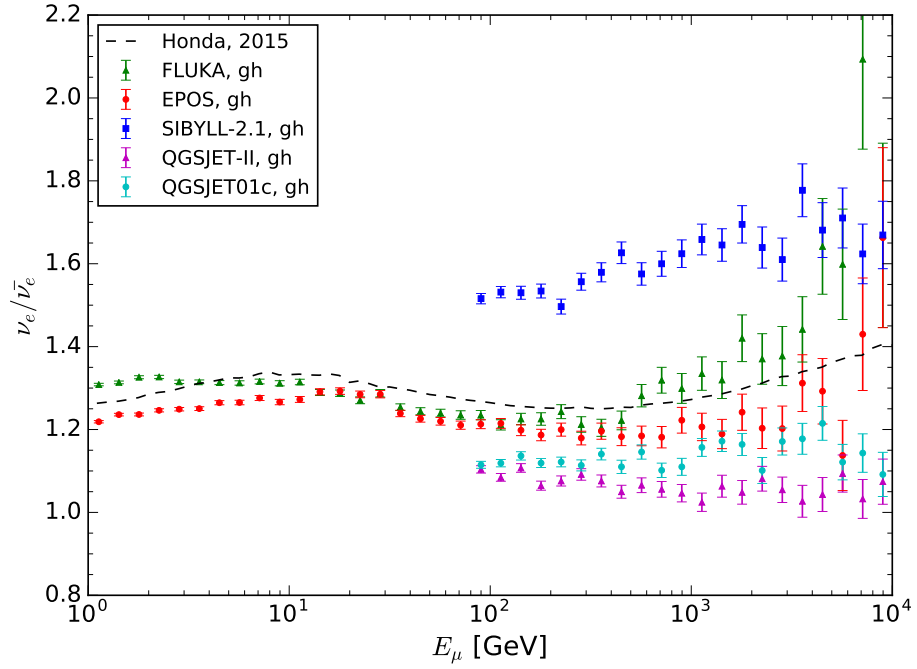


Figure 5.4.9.: Ratio of ν_e to $\bar{\nu}_e$ for FLUKA and EPOS, as well as results from Honda [57], and the models used in [2].

5.5. Discussion of Uncertainties

For the discussion of the theoretical uncertainties of this simulation, the combination of FLUKA with the GH primary model is used as a reference flux because it shows the best agreement with the available experimental data. All the uncertainties are presented as the maximum deviation from this flux. There are two main sources of systematic uncertainty, all of which are larger than the statistical uncertainties of the data sample. The first source lies in the hadronic interaction model itself, in particular the cross sections for the production of kaons and pions, which have been discussed extensively in the previous section. The second source is the primary CR spectrum, or rather the CR model being used. For both these sources the flux is calculated several times using different primary or different interaction models, and the maximum relative difference to the reference flux is recorded. The only other interaction model being used is EPOS, the primary models used for comparison are the TIG model [28], the polygonato model [26], the Zatsepin-Sokolskaya model [27], and the modified version of GST for AMS proton fluxes.

There are also systematic errors due to the limited primary CR energy range and the usage of the superposition approximation. Both these errors are unidirectional, the superposition causes an underestimation of the flux at the low-energy end of the spectrum, whereas the limited energy range leads to the fluxes being underestimated toward the high-energy part of the spectrum. The error due to superposition is discussed in more detail in Section 3.1, it is assumed to be 10 % for energies up to 20 GeV and drops to zero above a few 100 GeV. The error due to limited energy range cannot be estimated from the data simulated in this work, but it can be estimated using the data from [2] as it contains data for CR energies up to the EeV range. This is done using the inverse of a yield or transfer function, i.e. the distribution of primary CR energies for a given secondary energy. An example of this is shown in Fig. 5.5.2. For each of the secondary energies, the fraction of the transfer function that lies over 100 TeV is calculated. This is the contribution that will be missing from the simulation with a limited energy range. As this fraction depends on both the primary model and the interaction model, it is calculated using the GH model and averaged over the interaction models used in [2], viz. SIBYLL-2.1, QGSJET-II, and QGSJET01c.

Fig. 5.5.1 shows all systematic error sources together. Despite the previously discussed disagreement between EPOS and the muon data, the influence of the hadronic model does not constitute the largest source of uncertainty. At high energies the error due to the limited energy range dominates over all others, in principle this is also the easiest to fix, by simply extending the simulated energy range. While abandoning the superposition approximation in favor of a more detailed composition would be feasible, the uncertainty due to the primary model is still the more significant contribution. Even if one assumes no correlation between those two uncertainties, the improvement by a more accurate simulation of the composition would still be limited by the uncertainty of the primary spectrum. There is also a notable asymmetry in the uncertainties, generally the fluxes in this simulation appear more likely to be underestimated.

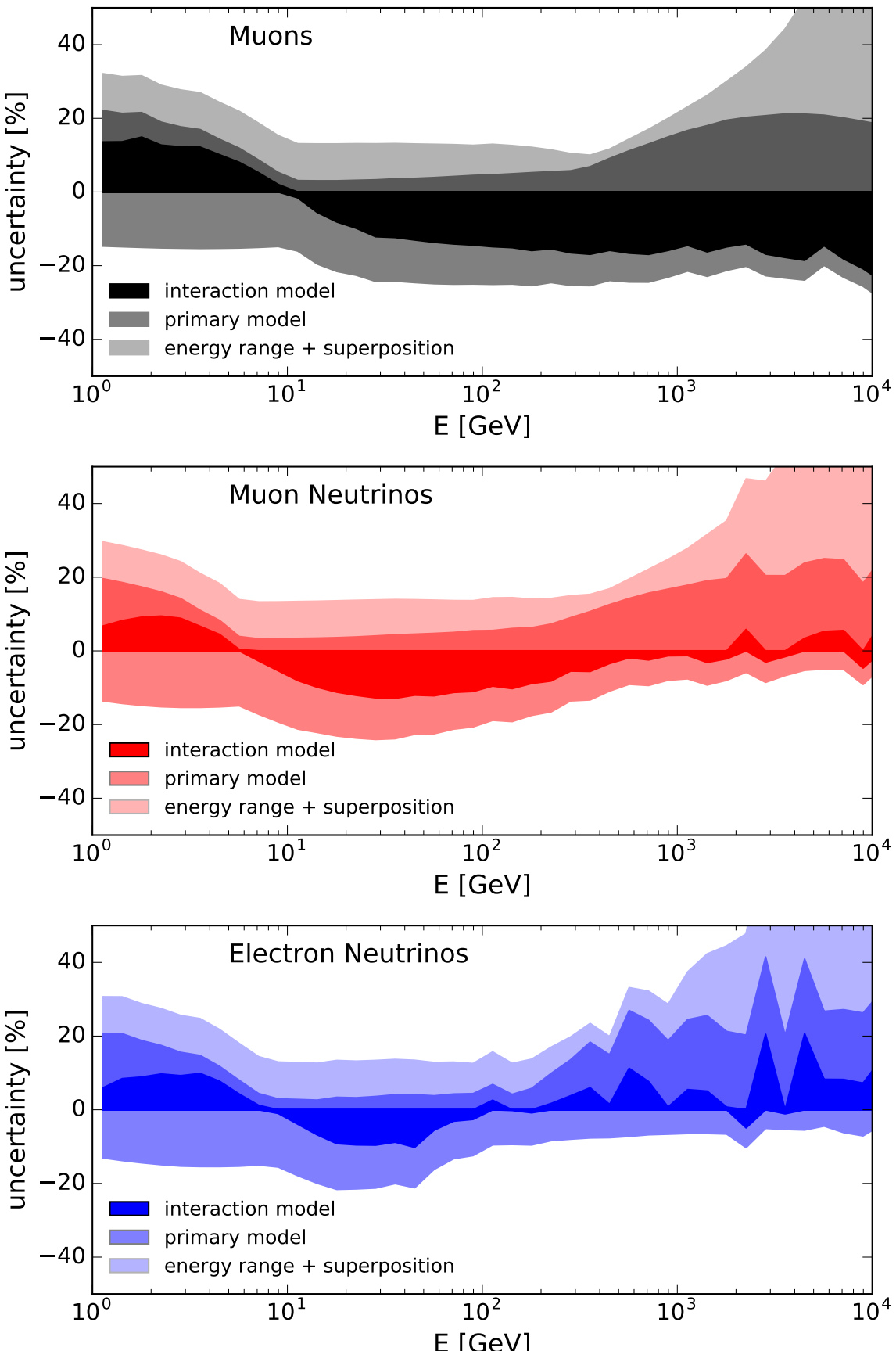


Figure 5.5.1.: Systematic uncertainties: Muons on top in black, muon neutrinos in the middle in red and electron neutrinos on the bottom in blue; central dark-shaded region represents uncertainty due to interaction model, medium shaded region uncertainty due to primary model, and light-shaded outer region error from superposition and limited CR energy range.

5. Results

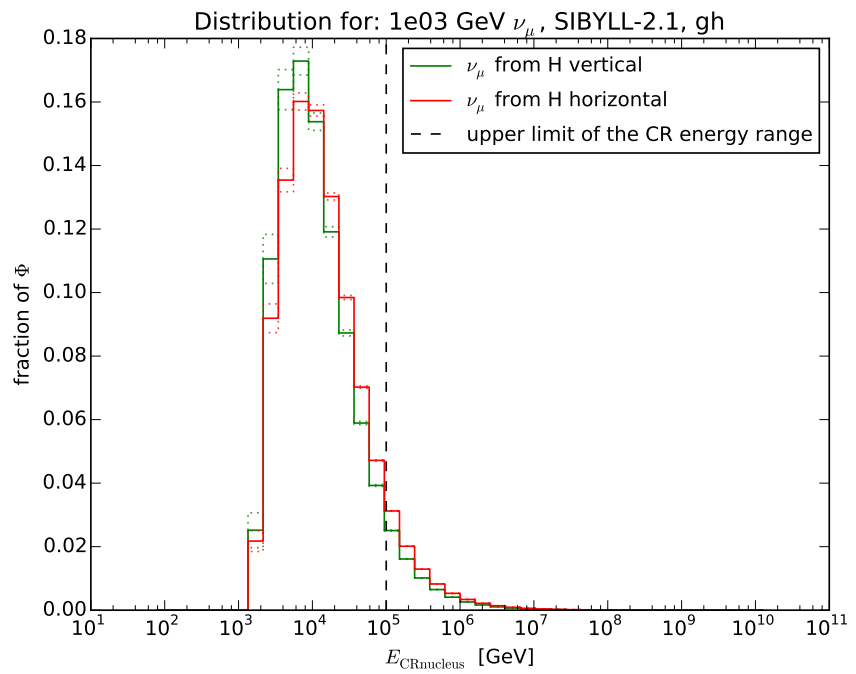


Figure 5.5.2.: Example of a transfer function for 1 TeV neutrinos for SIBYLL [2]. The dashed line corresponds to the upper limit of CR energies in this work (100 TeV), the contribution of higher CR energies is used to estimate the systematic error.

5.6. Geometry

For energies below 30 GeV the 1D approximation no longer holds and 3D effects become apparent [65]. For the purpose of 3D corrections to the 1D yields, the distributions of the height h at which the leptons were produced, as well as the opening angle α between the lepton and the CR axis have been recorded. In general α and h depend on the energy of the lepton as well as the energy E_{CR} and zenith angle $\cos(\theta)$ of the CR particle, although not in equal measure. Above TeV primary energies α depends mostly on the Lorentz-factor γ and hence the secondary energy of the leptons, and toward higher values of $\cos(\theta)$ (i.e. more vertical showers) the dependence on the primary energy is even less pronounced. An example distribution is shown in Fig. 5.6.1. For lepton energies above 100 GeV α should approach 0, here it approaches a constant value, which corresponds to the lowest bin in α . For the production height h there is a rising trend with the secondary energy, but a falling trend as E_{CR} increases. However, when shown as a function of $x = E/E_{\text{CR}}$, as in Fig. 5.6.2 on the left, the trend appears to be reversed. This can be explained by the fact that high-energy CR particles penetrate less far into the atmosphere than lower energy CR particles, and therefore the first interaction takes place at higher altitudes. However, particles with lower x are generally not produced in the first interaction but rather in the younger part of the shower, which corresponds to lower altitudes.

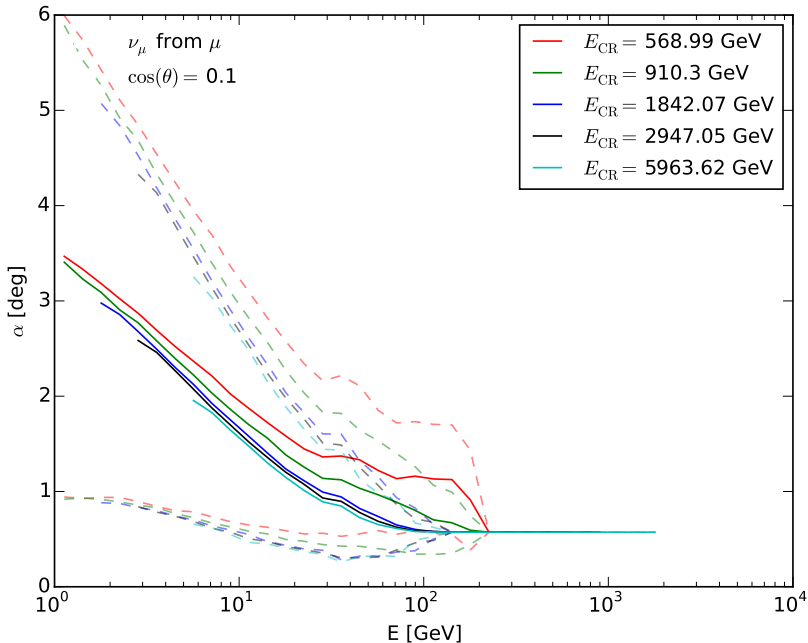


Figure 5.6.1.: Example distribution of the average opening angle α for different primary energies; dashed lines correspond to one standard deviation.

This constitutes a dilemma, as the natural choice of variable for α seems to be E , whereas it is x for h . As these distributions are intended to be used for neutrino oscilla-

5. Results

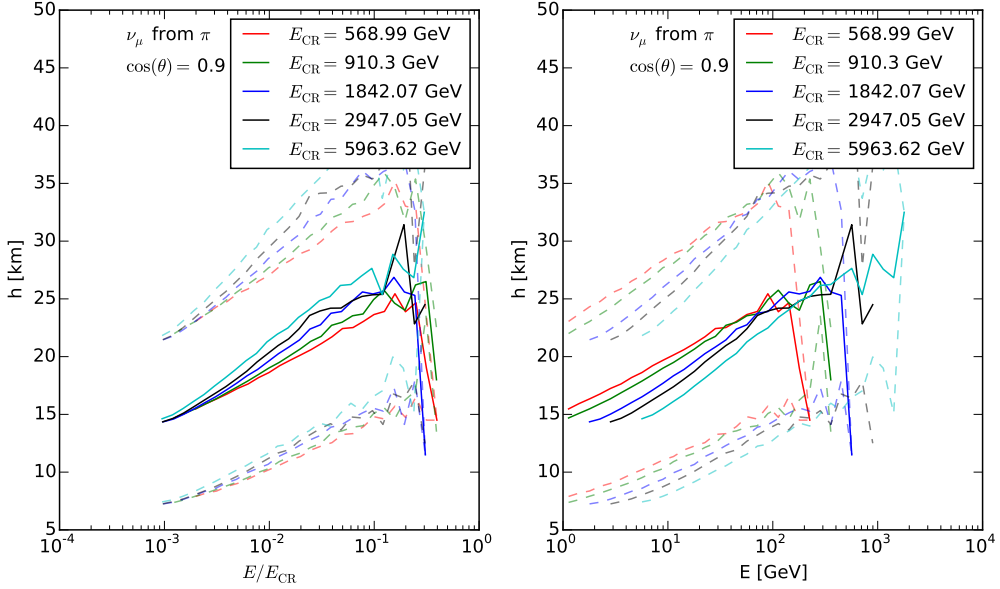


Figure 5.6.2.: Example distribution of the average production height h for different primary energies, as a function of x (left) and E (right); dashed lines correspond to one standard deviation.

tions, which depend on the neutrino energy, E is chosen as the variable for all geometry distributions. This in turn raises the question how a meaningful average of the production height can be calculated over different primary energies. The most accurate way would be to weight each histogram according to the contribution of the associated E_{CR} to the cosmic ray flux. These weights have already been calculated for use in the lepton fluxes, but as the production height is not an additive quantity, special care needs to be taken to only average over those histograms that actually contribute to the lepton flux at a given energy E . This approach however introduces deviations, probably due to the steeply falling primary spectrum, so instead all weights are chosen to be equal. The results show similar trends in both cases, but those trends are more easy to see in the case of equal weights.

5.6.1. Production height

For muons, the production height distribution does not differ significantly between muons from the decay of kaons, pions, and unflavored mesons, so only the average over all mesons is shown in Fig. 5.6.3. For neutrinos there is a difference between those produced from meson decay and those from muon decay. This is shown in Fig. 5.6.4. As a general trend, production height decreases toward the horizon. For leptons from meson decay, the production height rises as a function of energy, only for neutrinos from muon decay it decreases. This is expected, as higher energy neutrinos would be associated with higher Lorentz boost factors for the muons as well, which means the muons cover a

longer distance before they decay. On closer inspection the production height for muons and neutrinos from meson decay is not the same either. While the distribution for neutrinos from meson decay is shown to be composed of a relatively flat part between 1 GeV and 100 GeV and a more steeply rising part at higher energies, for muons the flat part disappears in favor of one continuously rising function toward the horizon. This is no contradiction. First of all, the energy distribution is not symmetrical in meson decay, but generally the resulting muon carries most of the energy, in particular for pion decay. In addition to that, low-energy muons are more likely to decay, in particular toward the horizon, and therefore the production height distribution is skewed toward lower altitudes. The distributions for EPOS and FLUKA are virtually indistinguishable, therefore only EPOS is shown here, the plots for FLUKA are shown in the appendix.

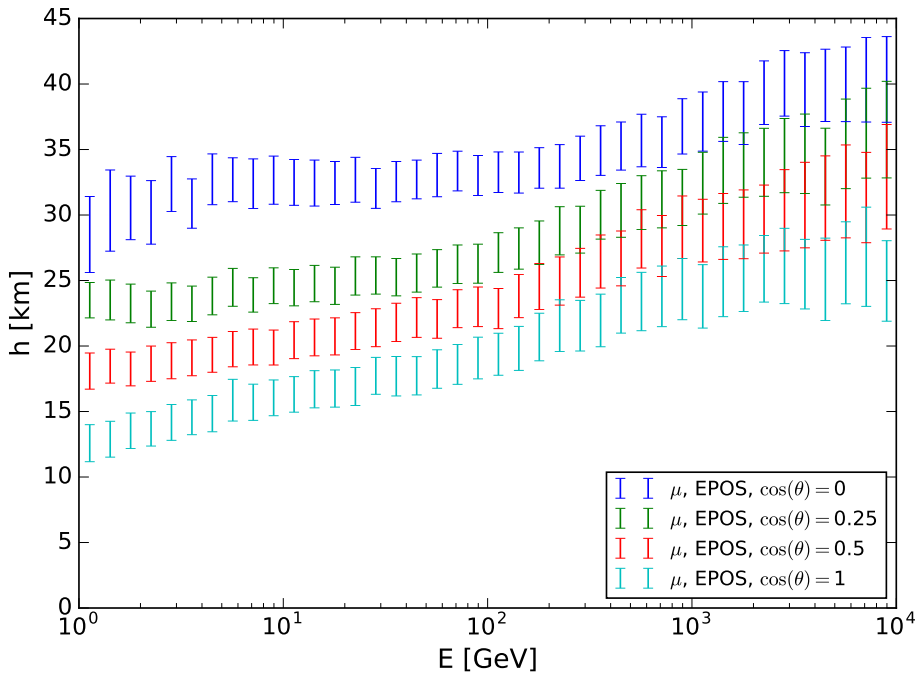


Figure 5.6.3.: Average production height of muons simulated with EPOS, shown for different zenith angles. Muons from horizontal directions ($\cos \theta = 0$) are produced at higher altitudes than vertical muons ($\cos \theta = 1$).

5.6.2. Opening Angle

For the distribution of the opening angle α , calculating averages using equal weights does not reduce visual noise, but it greatly distorts the distribution, so the weighting is done using appropriate weights calculated with the GH model. This is because the distributions are almost flat for primary energies below 100 GeV, and equal weights lead to overestimating the contribution from higher energies.

To show the dependence of the zenith angle, the distribution for a given value of $\cos(\theta)$ shown in the plots is the average taken over $\cos(\theta)$ and the two neighboring bins, e.g.

5. Results

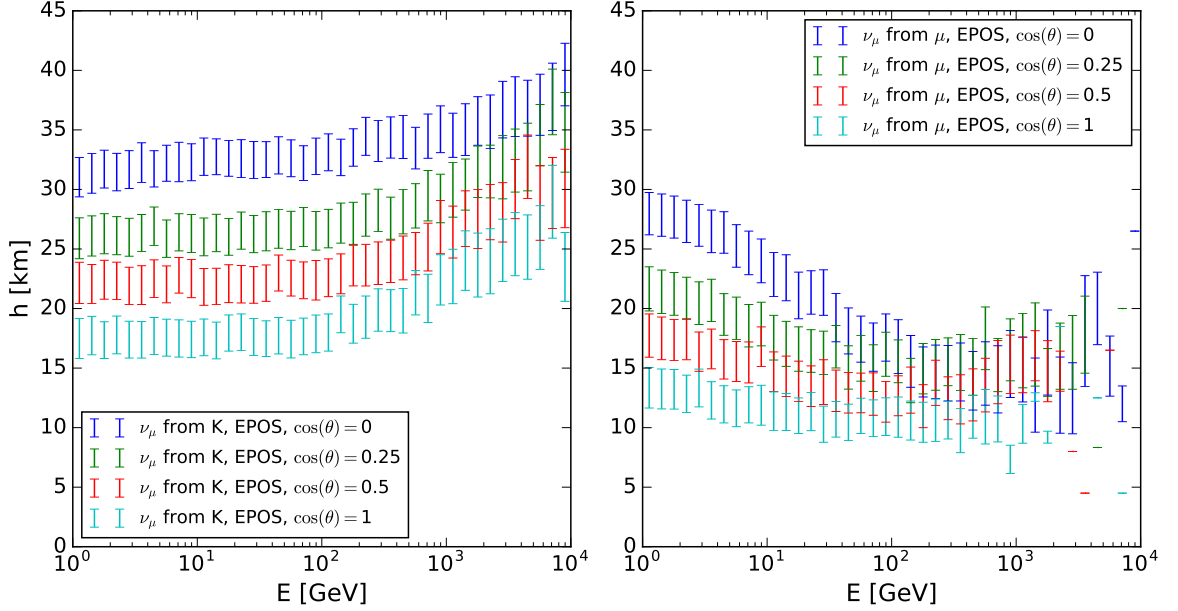


Figure 5.6.4.: Average production height of muon neutrinos from kaon (left) and muon decay (right) simulated with EPOS.

$\cos(\theta) = 0.3$ corresponds to the average over 0.25, 0.3 and 0.35. This reduces random noise without distorting the trend too much. The resulting distributions are shown in Fig. 5.6.5 for muons and in Fig. 5.6.6 for muon neutrinos. Generally α increases toward the horizon and decreases with lepton energy, however, below 10 GeV a plateau seems to form for horizontal neutrinos that do not exceed 20° . This is in part an effect of the projection of the shower cone onto the observation level in CORSIKA. For example in the case of $\cos(\theta) = 0.1$, which corresponds to 84.3° , particles deflected away from Earth by more than 6° would never make it to the observation level, which means that mostly particles scattered toward Earth contribute. Assuming a symmetrical shower cone, this leads to large opening angles being suppressed. The mirroring technique used in this simulation compensates this effect for the yields, but is not sufficient to eliminate the skew from the α distribution. As muons generally have smaller opening angles the effect is less visible here.

Another noteworthy difference between muons and muon neutrinos is that for muons the largest opening angles are seen in pion decay, whereas for neutrinos they are seen in kaon decay. The distribution for neutrinos from muon decay does not differ much from the distribution of neutrinos from meson decay, but unflavored mesons seem to show consistently lower opening angles than kaons and pions. A possible explanation for this is that the different energy distribution in meson decay lead to muons and neutrinos of the same energy having parent mesons of different energy. Unfortunately, the energy of the meson was not recorded, and only the ratio between primary energy E_{CR} and the energy of the lepton is known. This is shown in Fig. 5.6.7 for different parent mesons using in this case the ratio of the average cosmic ray energy over the lepton energy

$\frac{\langle E_{\text{CR}} \rangle}{E_S} = \bar{x}$. It can be seen that muons from kaon decay generally have smaller values of x than those from pion decay, which means that those kaons are produced in a younger part of the shower, at lower altitudes and in a denser medium. For muon neutrinos, those from pion decay are produced at lower x than those from kaon decay. Given that those distributions change more significantly between vertical and horizontal muons than they do for neutrinos, it seems less likely that this is an effect of the density of the surrounding medium, as the medium would change in a similar fashion for both particles. A lower value of x would likely mean a lower Lorentz boost for the parent mesons as well, and therefore a larger opening angle, but as that energy is not known, it is not possible to determine whether the kinematics of the hadronic interaction or of the weak decay contribute more significantly to the distribution of α .

The major difference between FLUKA and EPOS lies in the unflavored mesons, which are produced at much lower rates in FLUKA and therefore not sampled efficiently. As any meaningful comparison is lost in random noise the distributions for FLUKA have been moved to the appendix.

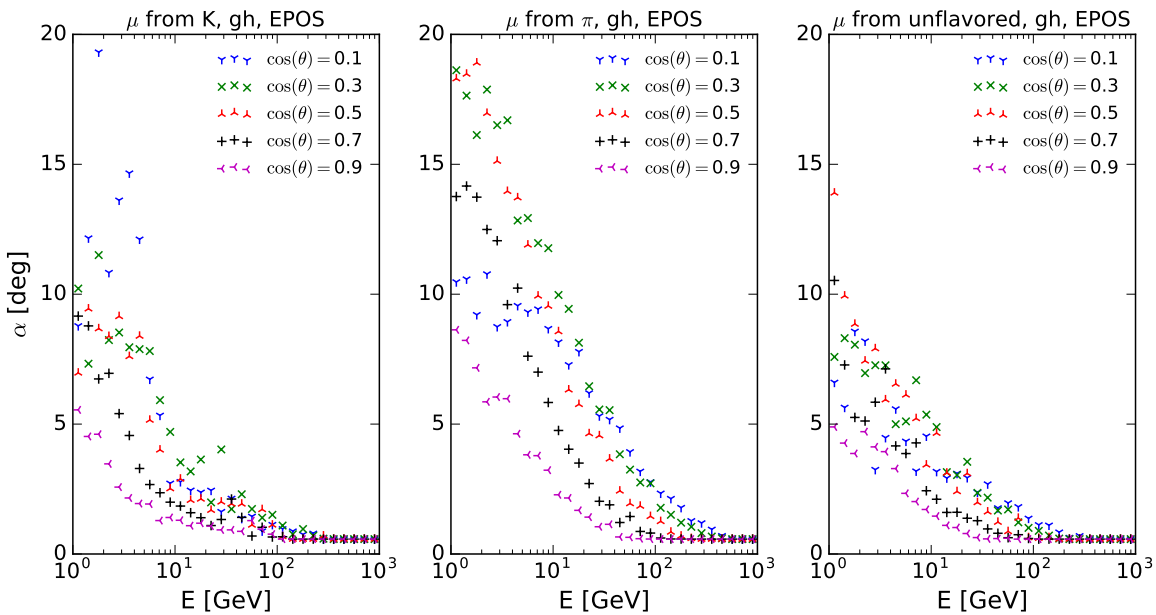


Figure 5.6.5.: Average opening angle of muons simulated with EPOS, shown for different zenith angles. From left to right: Muons produced in the decay of kaons, pions and unflavored (mostly η) mesons.

5.6.3. Comparison with Honda

One rather unexpected difference between FLUKA and EPOS can be seen in the zenith dependence of the low-energy part of the spectrum. The results of this simulation are compared to the result of the Honda simulation, which is a complete 3D simulation. This is shown in Fig. 5.6.8 for FLUKA and Fig. 5.6.9 for EPOS + UrQMD. For the purpose

5. Results

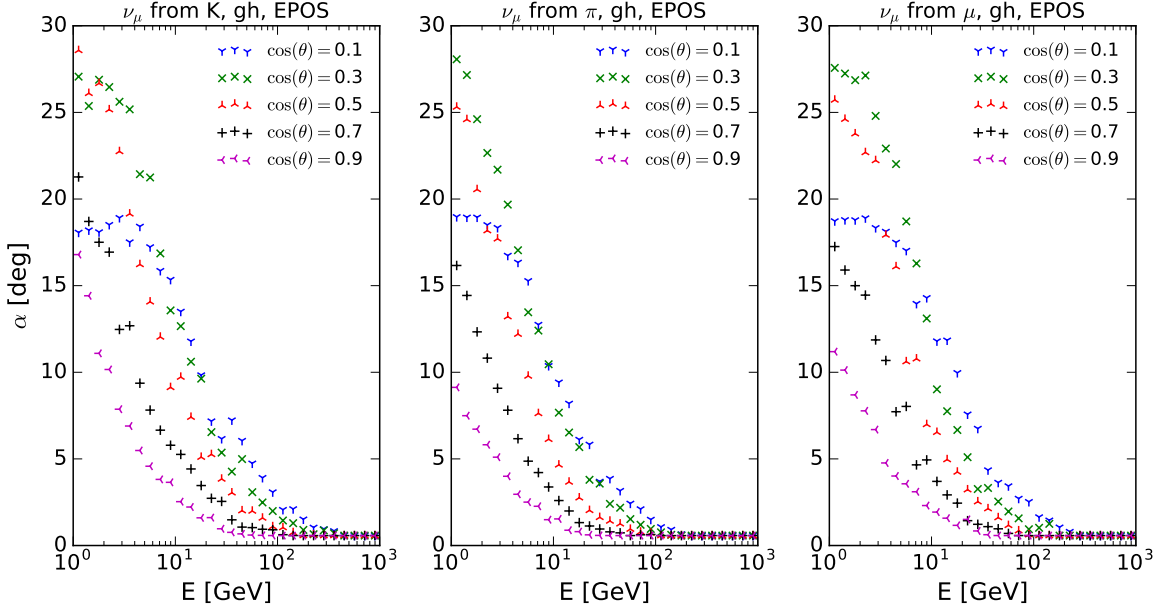


Figure 5.6.6.: Average opening angle of muon neutrinos from kaon (left) and muon decay (right) simulated with EPOS, shown for different zenith angles. From left to right: Muon neutrinos produced in the decay of kaons, pions and muons.

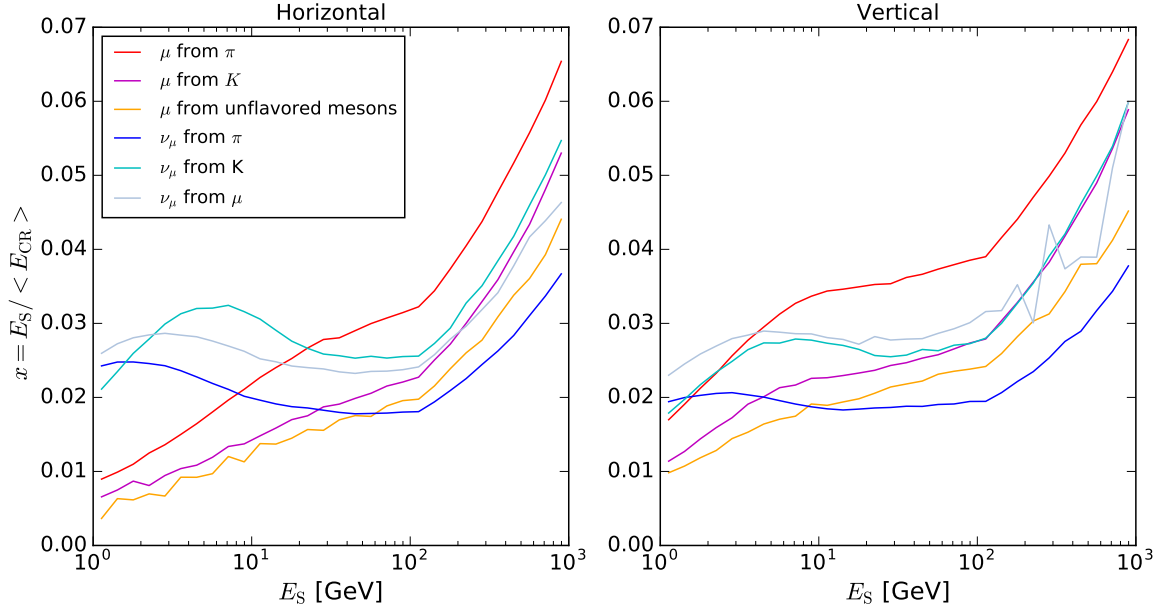


Figure 5.6.7.: Ratio between lepton energy and average CR energy $x = \frac{\langle E_{CR} \rangle}{E_S}$ for different mesons, horizontal ($\cos \theta = 0$) showers on the left, vertical ($\cos \theta = 1$) showers on the right. Muons in shades of red, muon neutrinos in shades of blue.

of this comparison the fluxes have been renormalized to the same value at $\cos(\theta) = 0.5$. This is necessary because neither the energy binning nor the primary flux model used by Honda matches the ones used in this work. For zenith angles below 70° there is no visible difference between the Honda 3D simulation and the 1D simulation using yields. At higher zenith angles the mirroring technique described in Section 3.3.3 is used. It provides a more conservative estimate for FLUKA than predicted by the Honda simulation, for EPOS however, it seems to introduce fluctuations. This behavior could be an artifact of the transition from EPOS to UrQMD visible in this energy range, or it could point to a more fundamental problem with the mirroring technique.

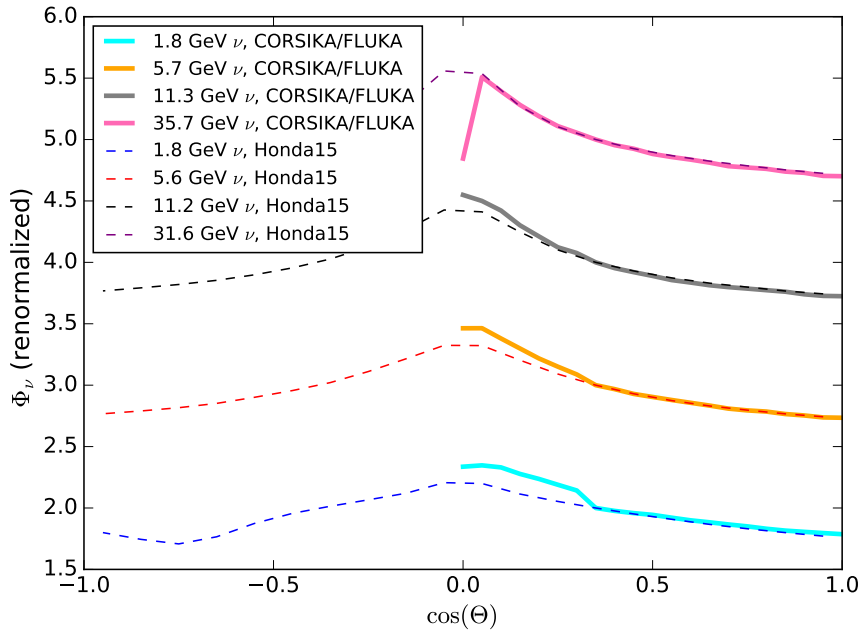


Figure 5.6.8.: Zenith dependence of the muon neutrino flux with FLUKA compared with Honda [57]. The fluxes have been renormalized to agree at $\cos \theta = 0.5$.

5. Results

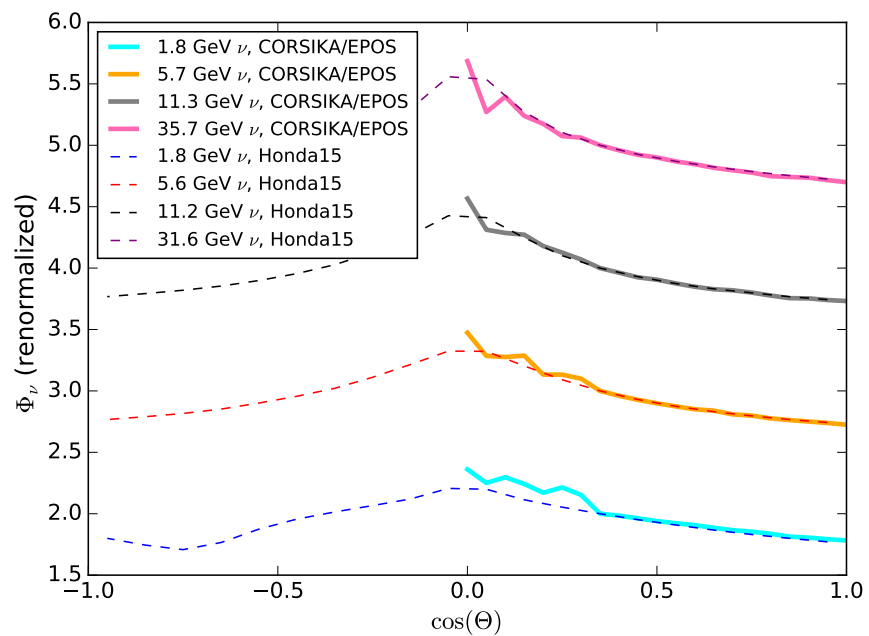


Figure 5.6.9.: Zenith dependence of the muon neutrino flux with EPOS compared with Honda [57]. The fluxes have been renormalized to agree at $\cos \theta = 0.5$.

5.7. Post-processing options

5.7.1. Geomagnetic cutoff

In principle the results of this work can be modified to account for the geomagnetic cutoff by changing the lower boundary of the energy integration when calculating the weights and setting the weights of yields to zero if the associated energy bin lies entirely below the cutoff. Calculating the actual value of the geomagnetic cutoff as a function of direction is beyond the scope of this work. Simply using the vertical cutoff value is not sufficient, as shown in [53] the value of the geomagnetic cutoff over the south pole can change from 1 GV to 40 GV for horizontal showers. It is fair to assume that it would increase even further for up-going particles. As an example the muon neutrino flux using the same primary model but different values of the cutoff is shown in Fig. 5.7.1, together with the flux measured by Frejus [61]. For neutrino energies above 30 GeV the effect of the cutoff disappears, but for energies below 5 GeV it could be possible to observe the difference experimentally, provided the experiment had an energy resolution comparable to Frejus and sufficient statistics.

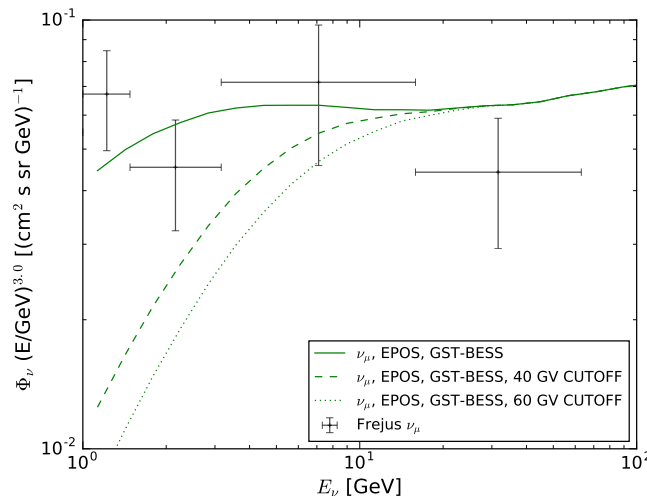


Figure 5.7.1.: Muon neutrino flux simulated with EPOS for different values of the geomagnetic cutoff, neutrino flux data taken from [61]. 40 GV corresponds to the highest cutoff for horizontal CRs at the South Pole.

5. Results

5.7.2. Neutrino Oscillations

At energies below 100 GeV neutrino oscillations can be expected, according to the PINGU LOI [39], there is a minimum of probability of the oscillation $\nu_\mu \rightarrow \nu_\mu$ around 25 GeV, with the exact energy depending on the zenith angle. This applies to up-going neutrinos, i.e. those that travel through the Earth. Because the radius of the Earth exceeds the thickness of the atmosphere by an order of magnitude, the height at which the neutrinos were produced is not expected to have a big effect on the length of their path and by extension their oscillation probability.

In order to test this quantitatively, the oscillation probabilities were calculated with NuSQUIDS [59], using the same binning for energy and production height that was used for the geometry histograms. The resulting probabilities for a production height of 100 km are shown in Fig. 5.7.2. The band of the minimum in the probability can be seen around 25 GeV at $\cos(\theta) = -1$, i.e. straight up through the earth, toward the horizon the energy of the minimum decreases and approaches 3 GeV. Fig. 5.7.3 shows the probabilities for $\nu_e \rightarrow \nu_e$, here the survival rate is much higher, and even at the lowest point the probability does not fall below 10%, therefore only the oscillations of muon neutrinos will be considered in more detail. Fig. 5.7.4 shows the difference between

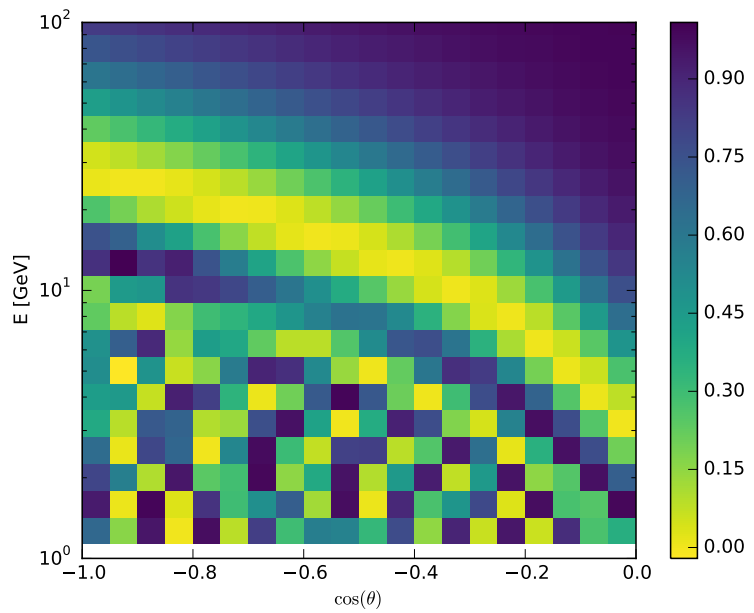


Figure 5.7.2.: Oscillation probability for $\nu_\mu \rightarrow \nu_\mu$ for 100 km production height. The band of the minimum in survival probability extends from ≈ 25 GeV for up-going ($\cos \theta = -1$) neutrinos to ≈ 3 GeV for horizontal ($\cos \theta = 0$) neutrinos.

the probabilities of $\nu_\mu \rightarrow \nu_\mu$ for the minimum and maximum production height recorded (100 km and 0.5 km, respectively). Above 10 GeV the differences are virtually nonexistent, and they only exceed 20% for horizontal neutrinos. This means that the spread

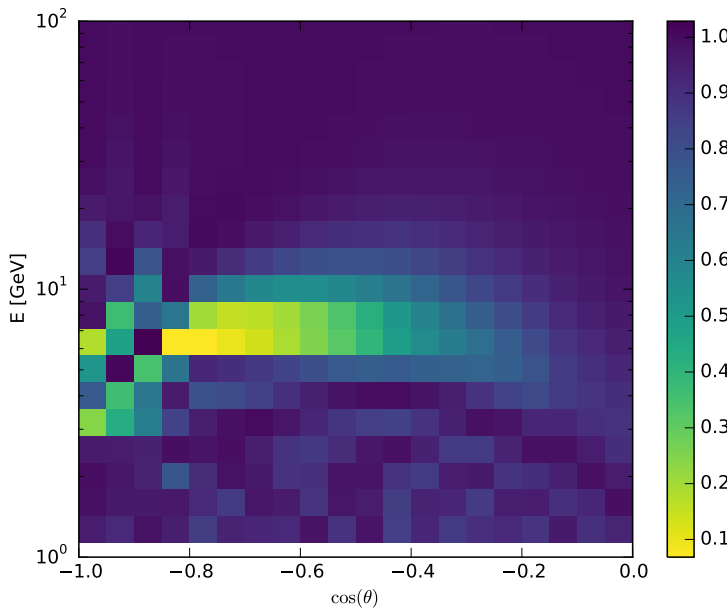


Figure 5.7.3.: Oscillation probability for $\nu_e \rightarrow \nu_e$ for 100 km production height. Apart from a small region below 10 GeV most electron neutrinos survive.

around the average production height will only be barely noticeable in the resulting flux.

The probabilities calculated with NuSQUIDS [59] can be applied to the up-going muon neutrino flux, to examine what flavor of neutrinos the muon neutrinos oscillate into. The exact procedure is described in Section 4.4.2 and the result is shown in Fig. 5.7.5. Here the height of the bars indicates the absolute value of the flux, while the colors denote the particular neutrino flavors. For comparison the unmodified electron neutrino flux is added as well. It can be seen that the flux from $\nu_\mu \rightarrow \nu_e$ is generally small compared to the electron neutrino flux, and only exceeds it around 5 GeV. The band of muon neutrino disappearance is clearly visible around 25 GeV, and it can also be seen that most of those muon neutrinos oscillate into tau neutrinos. There are also minima in the muon neutrino flux around 2 GeV, 4 GeV, and 9 GeV, but their energy range is relatively small, so they are isolated to single bins. Depending on the energy resolution of the detector, these minima would probably not be visible.

5. Results

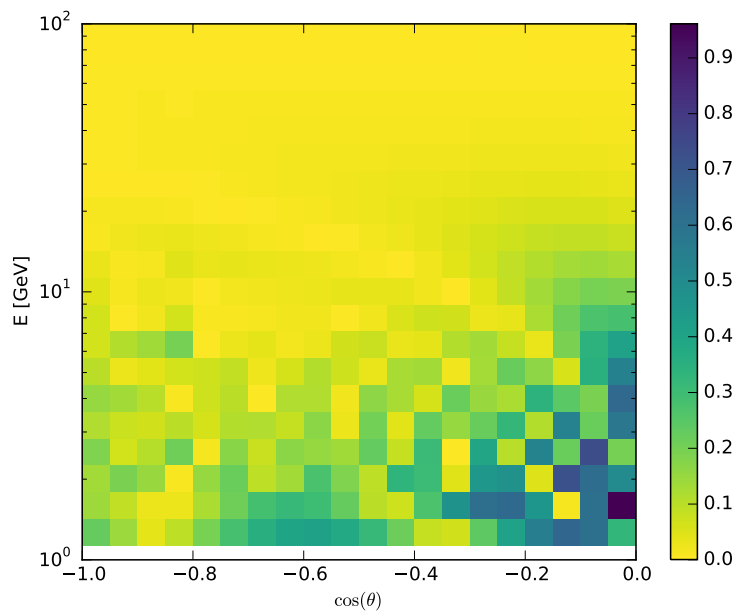


Figure 5.7.4.: Difference in probability for $\nu_\mu \rightarrow \nu_\mu$ between 100 km and 0.5 km production height. Note that the largest differences occur for horizontal neutrinos at the lowest energies.

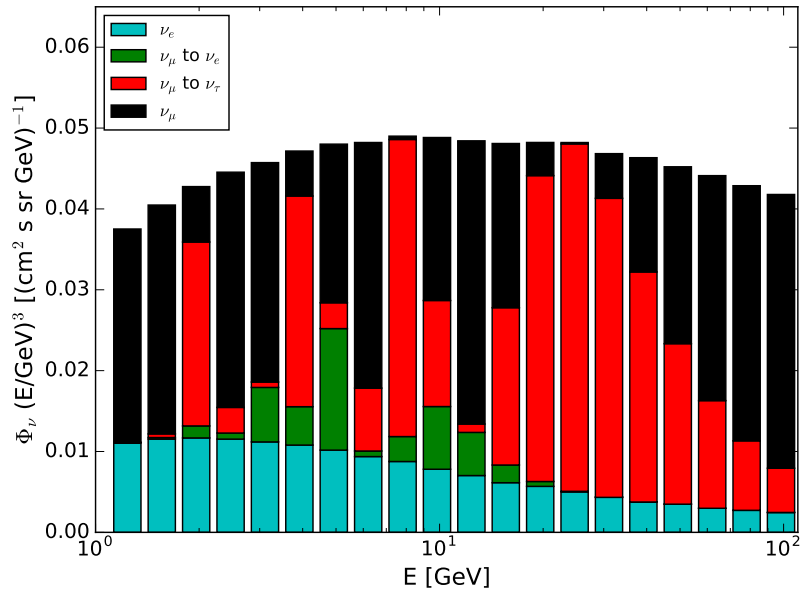


Figure 5.7.5.: Flux of up-going neutrinos ($\cos(\theta) = -1$). Resulting flavors shown for muon neutrinos after oscillation, unmodified electron neutrino flux added for comparison.

The recently published unfolding of the atmospheric neutrino fluxes by the Super Kamiokande experiment [66] suggests that oscillations need to be considered to obtain a correct prediction of the fluxes. Fig. 5.7.6 shows the published flux measurements as well as the fluxes obtained in this work. The down-going calculated in this work is shown without modification, the up-going flux was obtained by assuming up-down-symmetry and applying the corresponding oscillation weights to the flux. As can be seen, neither the up- nor the down-going spectrum agrees with the Super Kamiokande data, but the average between both matches the observations. The spectra obtained by Frejus [61] are shown for comparison. The agreement at higher energies appears to be quite good. The excess of the flux observed by Frejus at low energies could be explained by a different geometric distribution of the selected events, e.g. the excess of the horizontal flux is more pronounced at low energies which would affect the Frejus data more than the Super Kamiokande data, if Frejus is more sensitive to horizontal neutrinos.

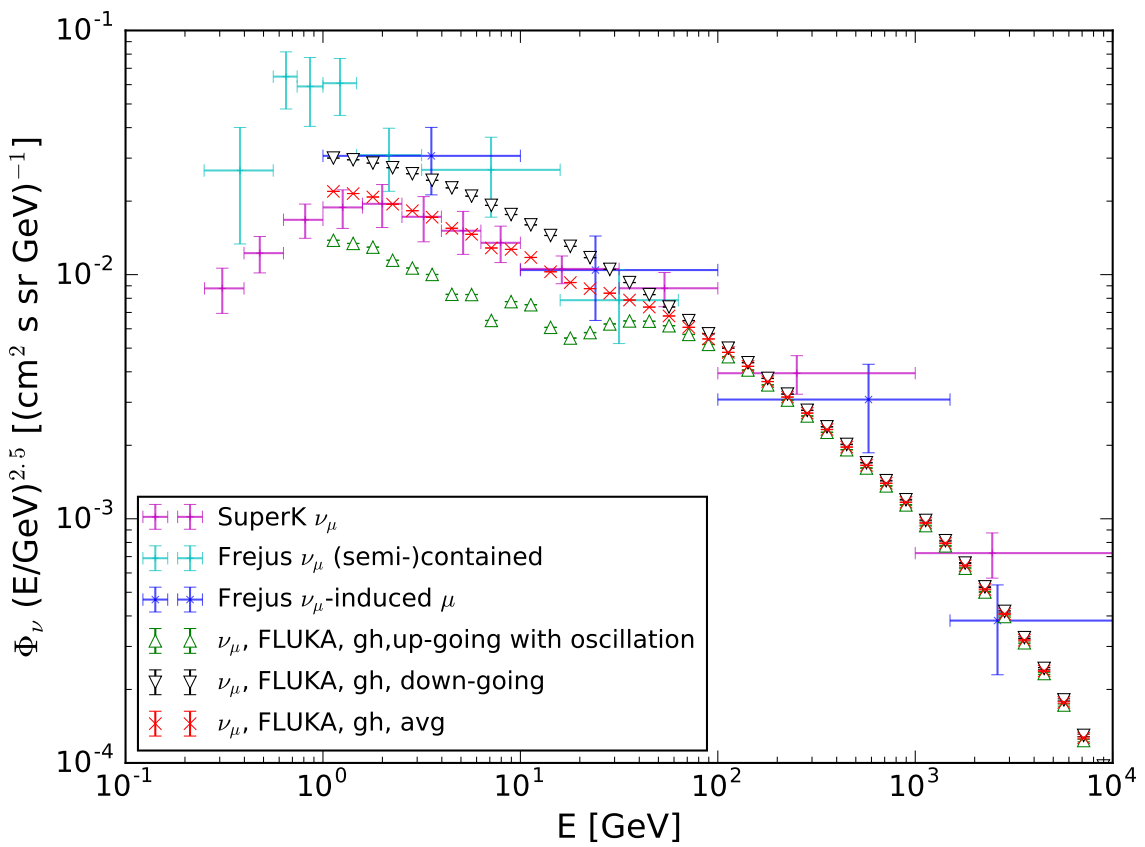


Figure 5.7.6.: Down-going muon neutrino flux simulated with FLUKA and up-going flux including oscillations calculated with NuSQUIDS [59]. The average of both directions agrees with Super Kamiokande [66] data. Frejus [61] data shown for comparison.

6. Conclusion and Outlook

6.1. Summary and Conclusion

The goal of this work was to develop a suitable method for the simulation of atmospheric muon and neutrino fluxes down to lepton energies of 1 GeV. The first step toward that goal was to determine how the simulation can be simplified and accelerated without reducing accuracy. The superposition approximation was found to be sufficient for the calculation of the flux. Combined with the sliding low-energy cutoff introduced in this work, these modifications allowed the simulation of 90 000 000 showers in less than 20 000 GHzCPUh using FLUKA and EPOS + UrQMD as interaction models. The CORSIKA output was modified to produce histograms instead of sequential binary files and the identification of the parent meson of atmospheric leptons was improved by using the information made available through the CORSIKA EHIST option. In addition to the particle yields, the distributions of the production height and the opening angle of the shower cone were extracted as well. The sample produced in this work contains yield histograms from CR particles covering an energy range from 5 GeV to 100 TeV in ten bins per logarithmic decade. Because those yields are stored in a custom tree-like data structure, they can easily be reweighted according to a number of models of the primary CR flux, including the possibility to add new models in the future without the need to repeat the simulation. The weights of the primary models can be modified to account for the geomagnetic cutoff. The production height of neutrinos was used to determine the correct length of the path for the calculation of the neutrino oscillation probabilities that were applied to the flux.

It was demonstrated that the method used in this work is suitable for neutrino energies down to 30 GeV for all zenith angles, and down to 1 GeV for zenith angles between $0^\circ \leq \theta \leq 70^\circ$. It was also shown that FLUKA can be used for CR energies from 5 GeV to 100 TeV, potentially eliminating the need for separate low-energy and high-energy models in CORSIKA. The simulation can be extended to take into account both neutrino oscillations and the geomagnetic cutoff, without having to repeat the simulation of the hadronic interactions in the shower. It combines the flexibility of using different combinations of models with a granularity of data that offers fine control over systematic effects, while simultaneously minimizing the necessary CPU resources. In addition to that, the systematic uncertainties of the atmospheric lepton fluxes between 1 GeV and 1 TeV have been studied quantitatively for the first time. The combined systematic uncertainties are less than 30 % for energies below 1 TeV. The statistical uncertainty of the sample never exceeds 8 %, for muons and muon neutrinos it is consistently less than 3 %.

6. Conclusion and Outlook

The most significant finding of this work is that the combination of the FLUKA interaction model with the GH primary model is able to consistently match all available experimental data for muons and neutrinos. This constitutes an improvement over the previous effort [2], which showed some disagreement in the muon charge ratios. In addition to that, the spread between FLUKA and EPOS is smaller than the spread between previously used interaction models. This suggests that more recent interaction models converge toward similar predictions as they are improved using new experimental data. While the deficit in the EPOS muon flux is surprising, the resulting uncertainty is not worse than with previously used models. This discrepancy also highlights the importance of performing cross-checks to ensure the optimal performance of the models being used.

It seems counterintuitive that the older GH model would show better agreement than the newer GST model, but that can be explained by taking into account that the muon fluxes used in this work were measured in roughly the same time period of the solar cycle as the primary CR data used to calculate the parameters of the GH model. Therefore, future experiments would still be better served by using a more recent primary model. Given that the uncertainty of both primary model and the superposition approximation are more significant than the interaction model at the lowest energies, it would seem prudent to update to a newer primary model as soon as new CR data, in particular by AMS or potentially ISS-CREAM, become available. Once the uncertainties of the primary flux are sufficiently reduced, abandoning the superposition approximation in favor of a more detailed simulation of the CR composition might become a more suitable approach. It should also be noted that recent observations of the CR spectrum by AMS are smooth enough (due to regularization) to be used for weighting, by using splines instead of a parametric interpolation model. This could facilitate the development of future CR models.

The main difficulty encountered in this work is the description of the zenith dependence of the flux for low-energy particles from inclined showers. Above 30 GeV or 70° the 1D simulation leads to results that are compatible with full 3D simulations, such as the one by Honda et al. The method of mirroring one half of the shower cone used in this work yielded better results than unmodified CORSIKA, but also revealed – or possibly introduced – another problem, i.e. fluctuations in the zenith dependence. It is not clear at this point whether these fluctuations are an artifact introduced by the combination of interaction models and the mirroring of the shower, or an indication of a more fundamental problem with CORSIKA. For studies of neutrino oscillations the results of this work are suitable in the range from $-1 \leq \cos \theta \leq -0.35$. That means neutrino trajectories through the Earth are mostly unaffected. For horizontal neutrinos, the minimum of the survival probability shifts toward lower energies, at $\cos \theta = -0.35$ it is closer to 10 GeV and therefore just outside the optimal sensitivity of PINGU [39]. For now, the mirroring technique leads to a more conservative estimate of the horizontal flux. Despite this challenge, the simulation still agrees well with the results from Super Kamiokande. This is because the errors affect only the horizontal part of the zenith distribution and are suppressed by averaging over all zenith angles.

In general, this work showed that a 1D simulation could potentially achieve results

similar to a full 3D calculation. Despite the limitations, FLUKA combined with the GH model matches experimental spectra of muons and neutrinos, as well as observed muon charge ratios and the neutrino flavor ratios from the Honda simulation. The methods developed, prepared and examined in this work – to incorporate neutrino oscillations or the geomagnetic cutoff, and to reduce the CPU needs of the simulation – can be applied in future works. Simulating the muon and neutrino fluxes in a consistent way, the possibility to calculate contributions from different mesons separately and to determine the transfer function in addition to the yields offer powerful tools to investigate the differences between interaction models and to study systematic uncertainties. The sample produced in this work can be used for studies of low-energy atmospheric neutrinos, in particular those related to neutrino oscillations. Incorporating oscillation probabilities for different scenarios, e.g. normal or inverted mass hierarchy, into the neutrino fluxes can be accomplished in a matter of minutes, without the need to repeat the simulation of the hadronic interactions. Similarly, updated models or data of CR fluxes can be included as they become available.

6.2. Outlook

Despite the good agreement with experimental data, there are still potential improvements and possible directions for future investigation. The largest systematic error is also the easiest to resolve: By extending the energy range of CR particles to be simulated the systematic errors due to the limited energy range can be removed. There are different possibilities on how to proceed: One possible solution is to continue using EPOS and FLUKA. This presents two challenges, as EPOS requires tremendous CPU resources, and FLUKA has only been used up to TeV CR energies so far. It would also be of great interest to compare these results with the more recent version of SIBYLL, SIBYLL-2.3. As FLUKA is considerably faster than EPOS, it is worthwhile to use EPOS with FLUKA as its low-energy model, albeit with a transition energy of about 100 TeV. This would greatly improve performance, as only the first few interactions are handled by EPOS and the majority of interactions is handled by FLUKA. This approach is not very well suited to study systematic uncertainties, but could offer a compromise between speed and accuracy for experiments to study the contribution of unflavored mesons. If the goal is simply to extend the energy range of secondary fluxes, the results of this work could also be combined with the results from Fedynitch et al. [2], because the binning of the secondary energies was chosen to coincide, and the same CR models are available in both simulations.

With regard to interaction models, the discrepancy in the kaon channel between EPOS and FLUKA, as well as the relative deficit of muons around 100 GeV in EPOS deserve further attention. Apart from inclusive fluxes, it would be worthwhile to investigate how well these models describe other shower observables. For example, L3+C measured muon multiplicities in air showers and compared them with the results of QGSJET [33]. Repeating this study with more recent interaction models, e.g. FLUKA, EPOS-LHC, and SIBYLL-2.3 could be a starting point.

6. Conclusion and Outlook

The zenith angle dependence toward the horizon at energies below 30 GeV needs to be investigated in order to have a correct description of the flux including the estimate of systematic uncertainties. The fundamental issue here is with secondary particles from inclined showers with large opening angles. The particles scattered away from Earth never appear in the CORSIKA output, but instead are discarded after a certain time has elapsed. See Section 3.3.3 for a more detailed description. Mirroring particles from the other half of the shower leads to fluctuations in some cases. Either the cause of these fluctuations needs to be resolved or a different way to extract shower particles that would normally time out needs to be found. The latter part could possibly be accomplished by modifying the INCLINED observation plane option in CORSIKA in a fashion similar to the modifications made to the ROOTOUT option in this work. An attempt has been made to create a method that would allow to correct simulated fluxes according to the distributions of the opening angle and production height of the particles. However, this method proved ineffective, it is included in the appendix for reference. For the purpose of neutrino oscillations the geometry could potentially be simplified. The only effect of the distribution of the production height appears for horizontal showers. If the most significant zenith range in an experiment covers mostly vertically up-going neutrinos, using simply the average production height appears to be sufficient.

For future studies, the representation of the uncertainties could be improved. Estimating the spread of possible CR fluxes from different CR models offers some insight into the uncertainty of the neutrino flux, but for use in experiments a more meaningful statistical measure is desirable. In case the uncertainties of the parameters of a CR model are known, the uncertainty related to that particular model could be estimated by a boot-strapping method. A number of pseudo-models – with their parameters sampled randomly from the CR model parameters considering the uncertainty – could be used to calculate the flux repeatedly. The final lepton flux would then be determined from the average and its uncertainty from the standard deviation of those calculated fluxes. This would allow to estimate the uncertainty associated with an individual CR model, instead of the spread of several different CR models that potentially have been tuned to data from different time periods.

7. Appendix

A. Superposition Approximation: Supplemental plots

While investigating the error due to the superposition approximation, a number of plots have been produced. As they take up a lot of space but offer very limited additional insight, they have been moved here from Section 3.1. Fig. A.1 and Fig. A.2 show the results for the flux of electron neutrinos from iron and helium, respectively. The results are similar to the results for muon neutrinos, but have larger statistical uncertainties, due to the relative rarity of electron neutrinos. Fig. A.3 shows the muon flux from helium, again the results are similar to the results for other leptons.

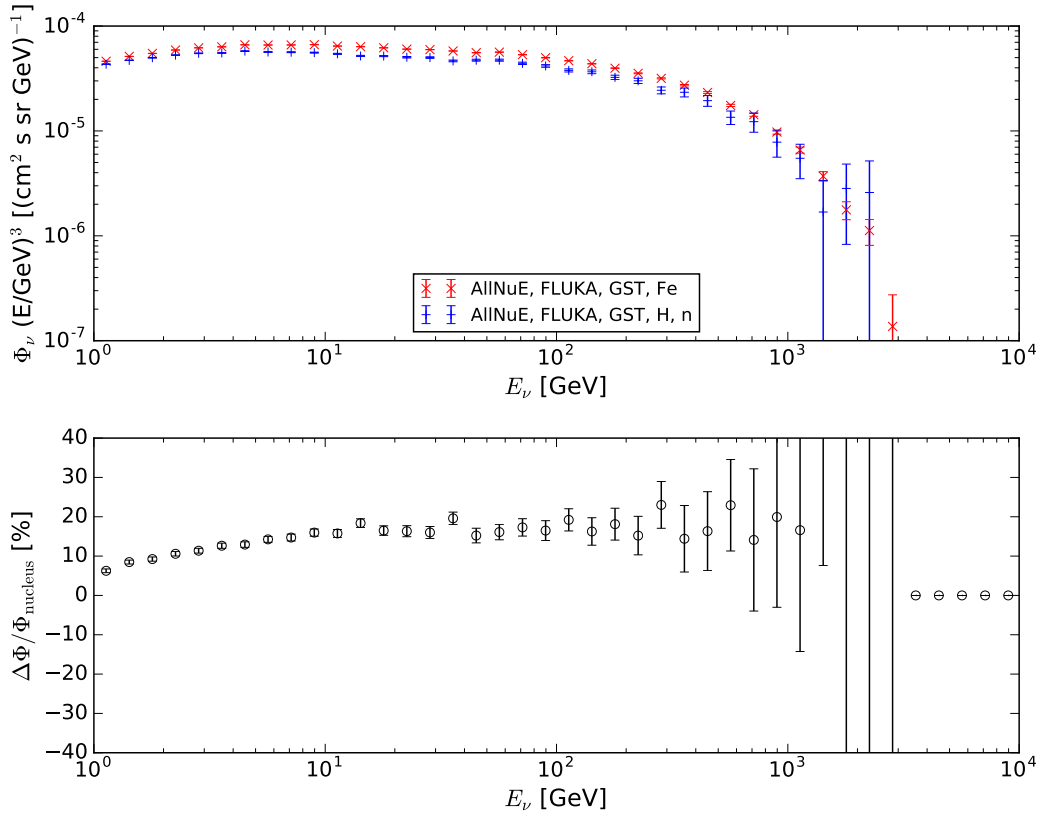


Figure A.1.: Comparison of the electron neutrino flux from iron, superposition in blue, iron nuclei in red. The deficit of the superposition rises continuously with energy.

7. Appendix

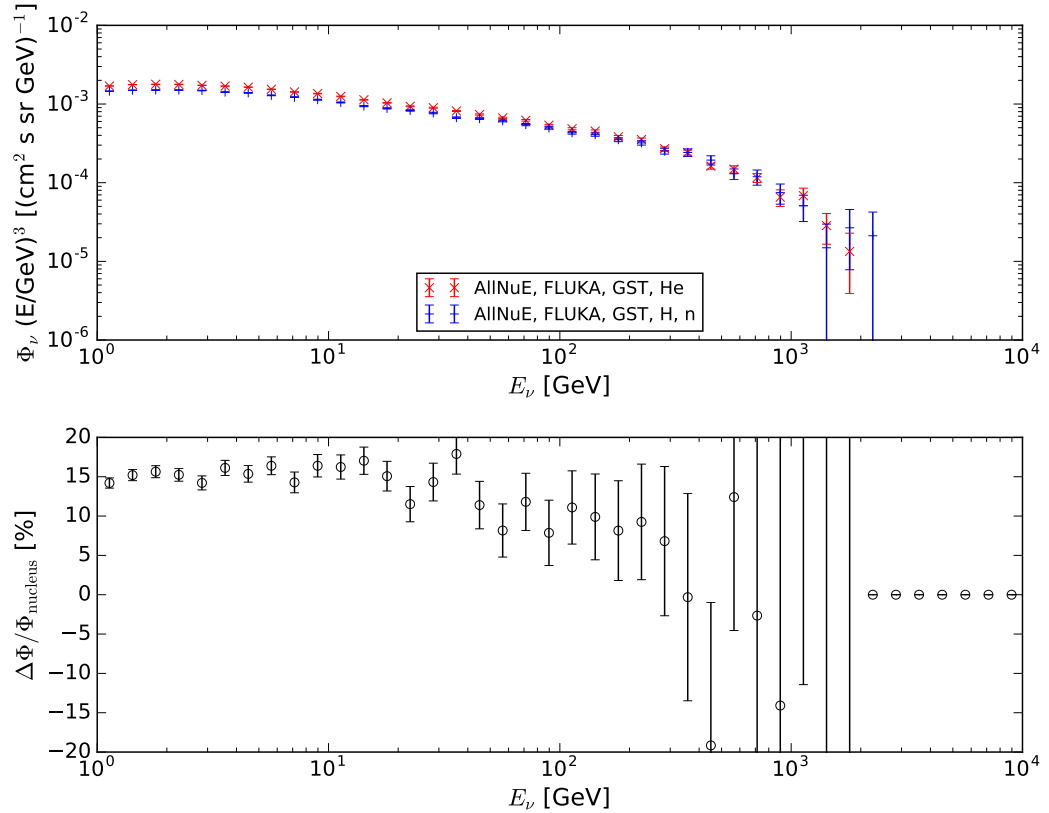


Figure A.2.: Comparison of the electron neutrino flux from helium, superposition in blue, helium nuclei in red. Here, the deficit of the superposition decreases toward higher energies.

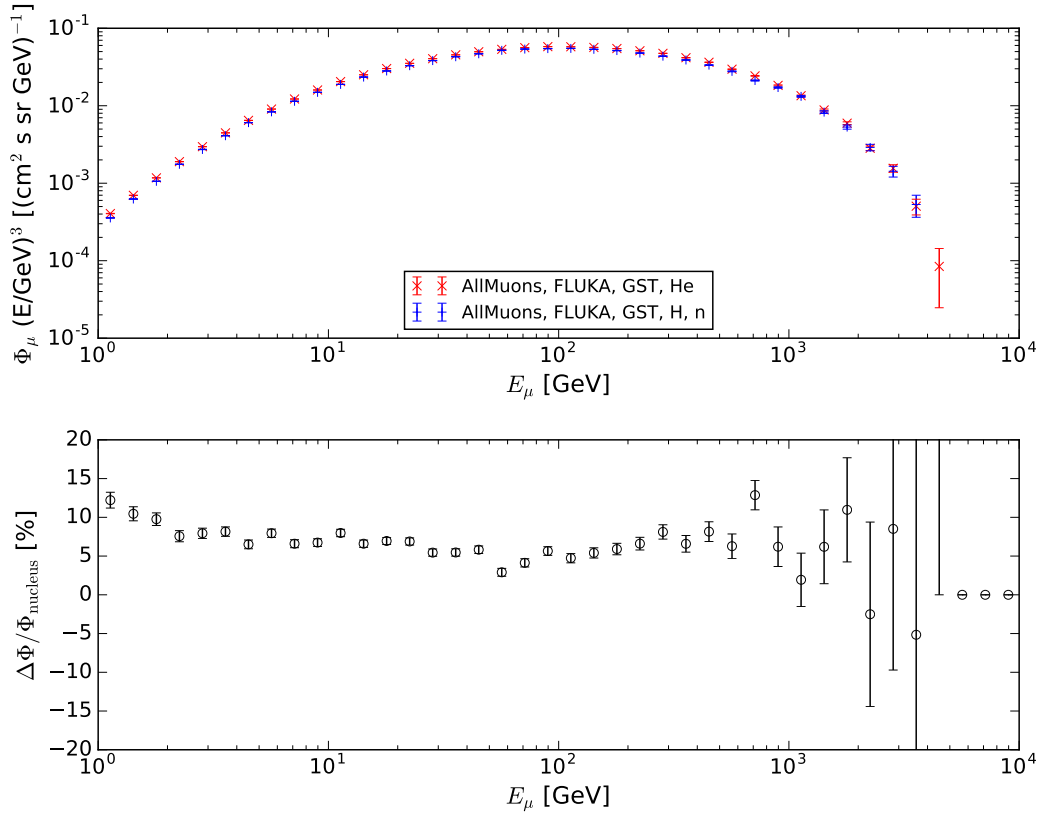


Figure A.3.: Comparison of the muon flux from helium, superposition in blue, helium nuclei in red. Here, the deficit is smallest around 100 GeV and increases toward lower and higher energies.

B. Geometry distributions for FLUKA

The histograms of the production height and opening angles for muons and neutrinos simulated with FLUKA have been moved here, because they offer little insight in addition to the results of EPOS. Fig. B.1 shows the averaged production height of muons simulated with FLUKA, Fig. B.2 shows the production height of muon neutrinos. The general trends observed with FLUKA are the same as with EPOS: The production height decreases toward the horizon, and increases as a function of energy, except for neutrinos from muon decay. The distribution for neutrinos from meson decay is composed of a relatively flat part between 1 GeV and 100 GeV and a more steeply rising part at higher energies. For muons the flat part disappears in favor of one continuously rising function.

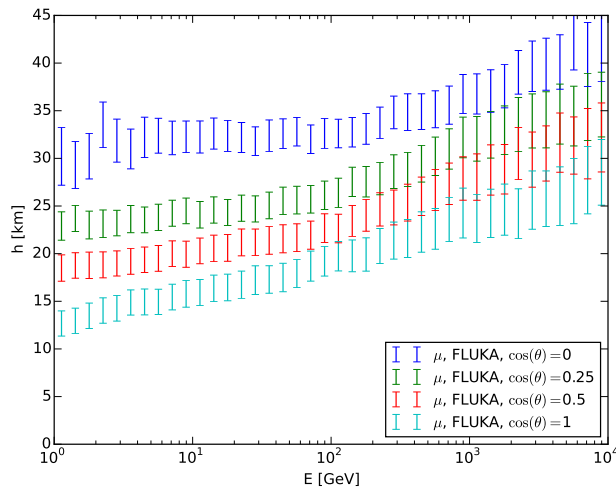


Figure B.1.: Average production height of muons simulated with FLUKA, shown for different zenith angles.

The opening angles of the showers simulated with FLUKA are shown in Fig. B.3 for muons and Fig. B.4 for muon neutrinos. The biggest difference between FLUKA and EPOS lies in the unflavored mesons, which are so few in FLUKA, that any trends in the distribution are obscured by statistical fluctuations. Apart from that, the trends are generally similar to EPOS: The opening angles of the shower cone grow larger toward the horizon and toward lower energies. However, for muon neutrinos closest to the horizon ($\cos \theta = 0.1$) the opening angles seem to reach a plateau for energies below 10 GeV. This could be related to the problems discussed in Section 3.3.4, namely that particles with very large opening angles may be deflected so far, that they never reach the surface and are therefore never written to the CORSIKA output.

B. Geometry distributions for FLUKA

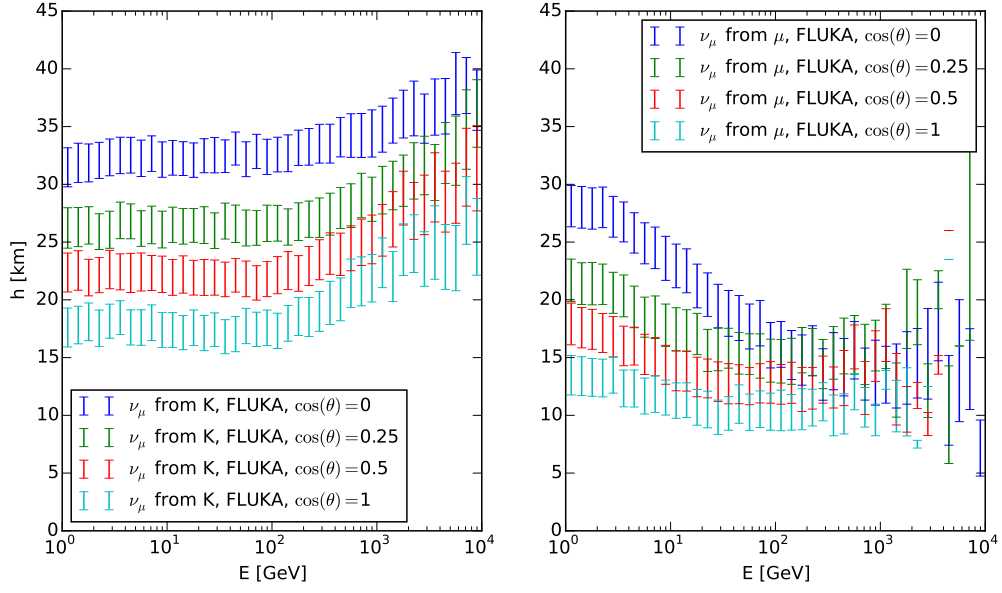


Figure B.2.: Average production height of muon neutrinos from kaon (left) and muon decay (right) simulated with FLUKA, shown for different zenith angles.

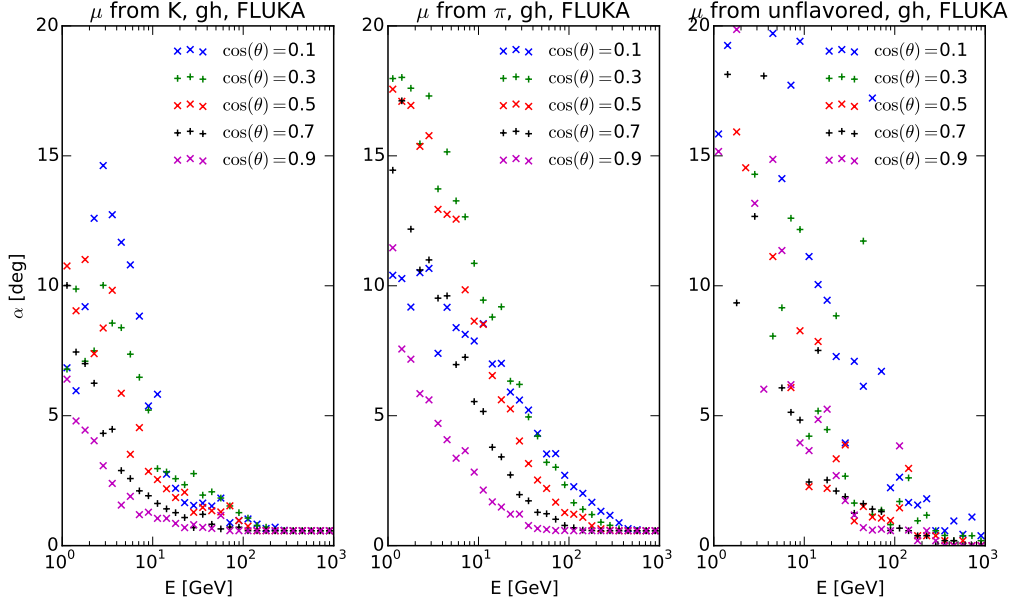


Figure B.3.: Average opening angle of muons simulated with FLUKA, shown for different zenith angles.

7. Appendix

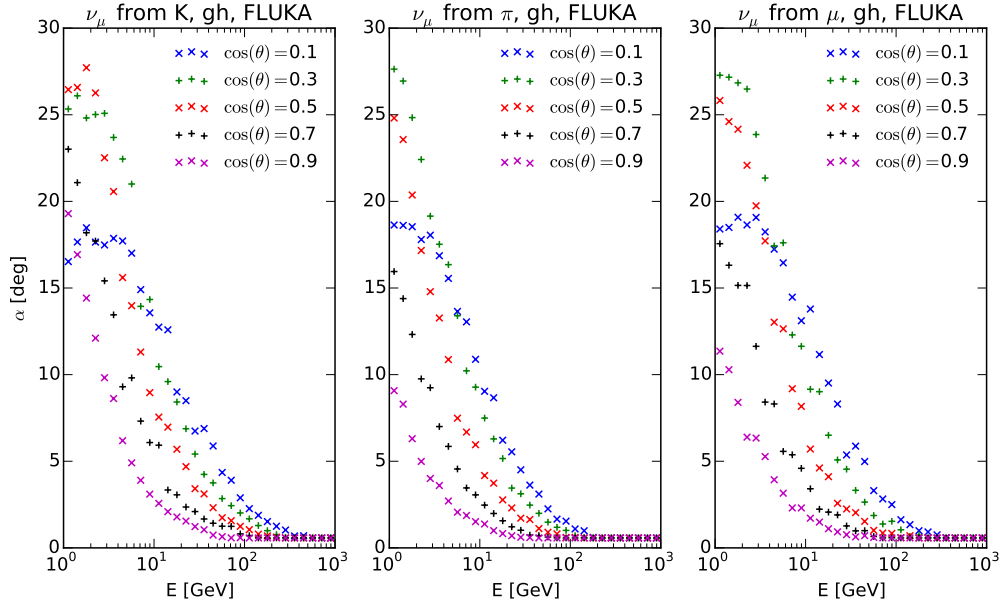


Figure B.4.: Average opening angle of muon neutrinos from kaon (left) and muon decay (right) simulated with FLUKA, shown for different zenith angles.

C. Shower Geometry - Attempted 3D corrections

The following section contains an attempt at a method to correct the results of a strictly 1D simulation to account for 3D effects. While it proved unsuccessful, it is still included here for reference, in the hope that it could provide some insight for future attempts.

In order to determine the correction in weights due to the 3D distribution of shower secondaries, one has to keep in mind that the Cosmic ray flux is mostly isotropic at every point on the surface of the atmosphere. That is, the CR flux is the same for all CR particles regardless of their angle relative to the surface normal of the atmosphere, as long as they are pointing towards the earth. This does only hold for CR energies above 100 GeV. Regardless of primary energy, leptons from EAS are scattered around the axis of the CR particle, with their scattering angle (mostly) only depending on Lorentz boost of the secondary particle. Simulating air showers from all these possible directions would be excessively expensive in terms of CPU usage. Instead, the range of θ between 0° and 90° is sampled at 20 different points, spaced in such a fashion that the distance l between the detector and the particle's entry point into the atmosphere does not deviate by more than 15 % between two points. For the simulated showers the distribution of the opening angle α between the primary CR direction and the direction of the secondaries is histogrammed as well as the fraction of l at which the particle was produced. In order to correctly weight the simulated showers it is necessary to compare the fraction of cosmic rays sampled in the 1D approximation with the weight obtained by the 3D distribution.

$$\int w(\phi, \theta, \Delta\theta, \Delta\phi) d\theta d\phi d\Delta\theta d\Delta\phi \quad (1)$$

For the calculation of the weights, a spherical detector with a radius c at a distance d from the center of the Earth is considered. The coordinate system is chosen so that the center of the (virtual) detector lies on the z axis and is hence symmetric with regard to ϕ .

For the weight w a CR particle arriving at a point (θ, ϕ) at the top of the atmosphere with angles $(\Delta\theta, \Delta\phi)$ relative to the line between the center of the detector and the point denoted by (θ, ϕ) is considered. In the 1D approximation the weight w_{1D} of the shower associated with this CR particle is 1 if the CR axis intersects with the detector and 0 otherwise.

For the (pseudo) 3D calculation the weight is calculated as follows: A plane is constructed through the center of the detector using the CR axis as the surface normal of the plane. The transverse distribution of the secondaries along the shower axis corresponds to a series of concentric rings around the point where the CR axis intersects with the plane. For each of those rings the overlap F_i between the ring and the detector is calculated. The final weight is then calculated by taking the weighted average the fraction of the are of the ring A_i that is covered by the detector

$$w_{3D} = \sum_i \frac{N_i}{N} \frac{A_i}{F_i} \quad (2)$$

with the radii r_i of the rings determined by the bin-boundaries in α and the length of the shower cone f , $r_i = f \tan \alpha_i$. N is the number of secondaries per shower, N_i the number inside one particular α bin.

Due to the ϕ symmetry the integral can be simplified to

$$\int w(\phi, \theta, \Delta\theta, \Delta\phi) d\theta d\Delta\theta d\Delta\phi \quad (3)$$

The final weight correction factor W for the weight of the yields is then given by the ratio between the integral over w_{1D} and w_{3D}

$$W = \frac{\int w_{1D}(\phi, \theta, \Delta\theta, \Delta\phi) d\theta d\Delta\theta d\Delta\phi}{\int w_{3D}(\phi, \theta, \Delta\theta, \Delta\phi) d\theta d\Delta\theta d\Delta\phi} \quad (4)$$

The integrals are evaluated numerically, first the coordinates (θ, ϕ) are transformed to cartesian coordinates, this is used as the starting point \vec{s} of a ray with the direction given by $(\Delta\theta, \Delta\phi)$:

$$\vec{d} = \frac{1}{(1 + \tan^2(\Delta\phi) + \tan^2(\xi))} \begin{pmatrix} -1 \\ -\tan(\Delta\phi) \\ -\tan(\xi) \end{pmatrix} \quad (5)$$

7. Appendix

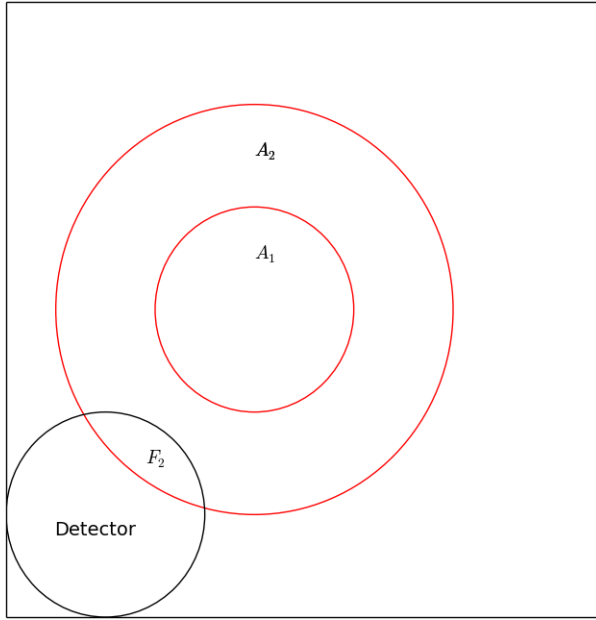


Figure C.1.: Illustration of the overlap between shower footprint and detector

with $\xi = 90^\circ - \theta - \Delta\theta$. If the center of the detector is denoted by the vector \vec{c} , then the distance between the CR trajectory and the detector is given by

$$d = |\vec{d} \times (\vec{c} - \vec{s})| \quad (6)$$

The 1D weight is then simply given by

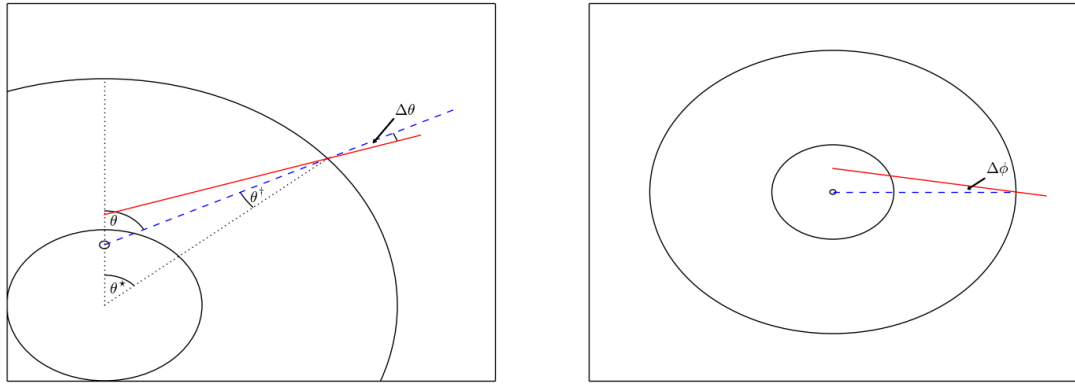
$$w_{1D} = \begin{cases} 1 & \text{if } d \leq c \\ 0 & \text{otherwise} \end{cases} \quad (7)$$

for the 3D weight the overlap between the detector and the rings representing the lateral distribution of the shower needs to be calculated. For concentric rings with radii r_i and a circle with radius c and a distance d between the two centers the overlap is calculated thusly. First the overlap between two circles is calculated by using

$$d_{(1/2)} = \frac{d^2 \pm (r_i^2 + c^2)}{2d} \quad (8)$$

to calculate the area of the two circular segments

$$A'(R', d') = R'^2 \arccos \left(\frac{d'}{R'} \right) - d' \sqrt{R'^2 - d'^2} \quad (9)$$



for each circle the overlap is then given by

$$F'(r_i, c, d) = A'(r_i, d_1) + A'(c, d_2) \quad (.10)$$

the overlap for one ring is given by

$$F(r_i, c, d) = F'(r_i, c, d) - F'(r_{i-1}, c, d) \quad (.11)$$

The area A_i of the individual rings is given by $A_i = \pi (r_i^2 - r_{i-1}^2)$ and the final weight for one shower is equal to

$$w_{3D} = \sum_i \frac{N_i}{N} \frac{A_i}{F_i} \quad (.12)$$

Bibliography

- [1] The Nobel Foundation. *The Nobel Prize in Physics 1936*. 2016. URL: http://www.nobelprize.org/nobel_prizes/physics/laureates/1936/ (visited on 06/07/2016).
- [2] A. Fedynitch, J. Becker Tjus, and P. Desiati. “Influence of hadronic interaction models and the cosmic ray spectrum on the high energy atmospheric muon and neutrino flux”. In: *Phys. Rev. D* 86.11, 114024 (Dec. 2012), p. 114024.
- [3] T.K. Gaisser. *Cosmic Rays and Particle Physics*. Cambridge University Press, 1990.
- [4] T. K. Gaisser. “Spectrum of cosmic-ray nucleons, kaon production, and the atmospheric muon charge ratio”. In: *Astroparticle Physics* 35 (July 2012), p. 801.
- [5] A. R. Bell. “The acceleration of cosmic rays in shock fronts - II”. In: *Monthly Notices of the Royal Astronomical Society* 182.3 (1978), p. 443.
- [6] M. Boezio et al. “The cosmic-ray proton and helium spectra measured with the CAPRICE98 balloon experiment”. In: *Astroparticle Physics* 19 (Aug. 2003), p. 583.
- [7] T. K. Gaisser, T. Stanev, and S. Tilav. “Cosmic ray energy spectrum from measurements of air showers”. In: *Frontiers of Physics* 8 (Dec. 2013), p. 748.
- [8] H. S. Ahn et al. “Energy Spectra of Cosmic-ray Nuclei at High Energies”. In: *The Astrophysical Journal* 707 (Dec. 2009), p. 593.
- [9] Y. S. Yoon et al. “Cosmic-ray Proton and Helium Spectra from the First CREAM Flight”. In: *The Astrophysical Journal* 728, 122 (Feb. 2011), p. 122.
- [10] S. Haino et al. “Measurements of primary and atmospheric cosmic-ray spectra with the BESS-TeV spectrometer”. In: *Physics Letters B* 594 (July 2004), p. 35.
- [11] P. Picozza et al. “PAMELA A payload for antimatter matter exploration and light-nuclei astrophysics”. In: *Astroparticle Physics* 27 (Apr. 2007), p. 296.
- [12] O. Adriani et al. “PAMELA Measurements of Cosmic-Ray Proton and Helium Spectra”. In: *Science* 332 (Apr. 2011), p. 69.
- [13] O. Adriani et al. “Measurement of Boron and Carbon Fluxes in Cosmic Rays with the PAMELA Experiment”. In: *The Astrophysical Journal* 791, 93 (Aug. 2014), p. 93.
- [14] M. Aguilar et al. “Precision Measurement of the Proton Flux in Primary Cosmic Rays from Rigidity 1 GV to 1.8 TV with the Alpha Magnetic Spectrometer on the International Space Station”. In: *Physical Review Letters* 114.17, 171103 (May 2015), p. 171103.

Bibliography

- [15] M. Aguilar et al. "Precision Measurement of the Helium Flux in Primary Cosmic Rays of Rigidities 1.9 GV to 3 TV with the Alpha Magnetic Spectrometer on the International Space Station". In: *Physical Review Letters* 115.21, 211101 (Nov. 2015), p. 211101.
- [16] The Pierre Auger Collaboration et al. "The Pierre Auger Observatory I: The Cosmic Ray Energy Spectrum and Related Measurements". In: *ArXiv e-prints* (July 2011).
- [17] J. C. Espadanal. "Measurement of the Muon Content of EAS with the Pierre Auger Observatory". In: *Particle and Astroparticle Physics, Gravitation and Cosmology: Predictions, Observations and New Projects*. Ed. by R. A. Ryutin and A. Petrov Vladimir. June 2015, p. 287.
- [18] M. G. Aartsen et al. "Measurement of the cosmic ray energy spectrum with IceTop-73". In: *Phys. Rev. D* 88 (4 Aug. 2013), p. 042004.
- [19] M.A.K. Glasmacher et al. "The cosmic ray energy spectrum between 1014 and 1016 eV". In: *Astroparticle Physics* 10.4 (1999), p. 291.
- [20] A P Garyaka et al. "An all-particle primary energy spectrum in the 3-200 PeV energy range". In: *Journal of Physics G: Nuclear and Particle Physics* 35.11 (2008), p. 115201.
- [21] S.F. Berezhnev et al. "Tunka-133: Primary Cosmic Ray Energy Spectrum in the energy range $6 \cdot 10^{15} - 10^{18}$ eV". In: *ICRC 2011 Proceedings* (2011).
- [22] M. Amenomori et al. "The All-Particle Spectrum of Primary Cosmic Rays in the Wide Energy Range from 1014 to 1017 eV Observed with the Tibet-III Air-Shower Array". In: *The Astrophysical Journal* 678.2 (2008), p. 1165.
- [23] W.D. Apel et al. "The spectrum of high-energy cosmic rays measured with KASCADE-Grande". In: *Astroparticle Physics* 36.1 (2012), p. 183.
- [24] L. Merten. *CosmicRayDataBase*. 2015. URL: <https://github.com/lukasmerten/CosmicRayDataBase> (visited on 06/07/2016).
- [25] T. K. Gaisser and M. Honda. "Flux of atmospheric neutrinos". In: *Annual Review of Nuclear and Particle Science* 52 (2002), p. 153.
- [26] J. R. Hörandel. "On the knee in the energy spectrum of cosmic rays". In: *Astroparticle Physics* 19 (May 2003), p. 193.
- [27] V. I. Zatsepin and N. V. Sokolskaya. "Three component model of cosmic ray spectra from 10 GeV to 100 PeV". In: *Astronomy and Astrophysics* 458 (Oct. 2006), p. 1.
- [28] M. Thunman, G. Ingelman, and P. Gondolo. "Charm production and high energy atmospheric muon and neutrino fluxes". In: *Astroparticle Physics* 5 (Oct. 1996), p. 309.
- [29] D. Maurin, F. Melot, and R. Taillet. "A database of charged cosmic rays". In: *Astronomy and Astrophysics* 569, A32 (Sept. 2014), A32.

- [30] Y. Shikaze et al. “Measurements of 0.2 20 GeV/n cosmic-ray proton and helium spectra from 1997 through 2002 with the BESS spectrometer”. In: *Astroparticle Physics* 28 (Sept. 2007), p. 154.
- [31] R. D. Strauss and M. S. Potgieter. “Where does the heliospheric modulation of galactic cosmic rays start?” In: *Advances in Space Research* 53 (Apr. 2014), p. 1015.
- [32] K.A. Olive and Particle Data Group. “Review of Particle Physics”. In: *Chinese Physics C* 38.9 (2014), p. 090001.
- [33] Yuqian Ma and C. Zhang. “A measurement of high multiplicity muon events with the L3+C detector”. In: *Proceedings, 30th International Cosmic Ray Conference (ICRC 2007)*. Vol. 5. 2007, p. 1213.
- [34] P. Achard et al. “Measurement of the atmospheric muon spectrum from 20 to 3000 GeV”. In: *Physics Letters B* 598.1-2 (2004), p. 15.
- [35] P. Adamson et al. “Measurement of the atmospheric muon charge ratio at TeV energies with the MINOS detector”. In: *Phys. Rev. D* 76 (5 Sept. 2007), p. 052003.
- [36] Raymond Davis. “Solar Neutrinos. II. Experimental”. In: *Phys. Rev. Lett.* 12 (11 Mar. 1964), p. 303.
- [37] IceCube Collaboration. *Official IceCube website*. 2016. URL: <https://icecube.wisc.edu/> (visited on 07/18/2016).
- [38] R. Abbasi et al. “The design and performance of IceCube DeepCore”. In: *Astroparticle Physics* 35 (May 2012), p. 615.
- [39] The IceCube-PINGU Collaboration. “Letter of Intent: The Precision IceCube Next Generation Upgrade (PINGU)”. In: *ArXiv e-prints* (Jan. 2014).
- [40] A. C. Vincent, S. Palomares-Ruiz, and O. Mena. “Analysis of the 4-year IceCube HESE data”. In: *ArXiv e-prints* (May 2016).
- [41] Ruhe, T., Scherianu, F., and Schmitz, M. “Measurement of the atmospheric muon neutrino energy spectrum with IceCube in the 79- and 86-String configuration”. In: *EPJ Web of Conferences* 116 (2016), p. 08004.
- [42] P. Lipari. “Tev muons in hadronic showers”. In: *Astroparticle Physics* 1 (Dec. 1993), p. 399.
- [43] Isaac Saba, Julia Becker Tjus, and Francis Halzen. “Limits on the source properties of FR-I galaxies from high-energy neutrino and gamma observations”. In: *Astroparticle Physics* 48 (2013), p. 30.
- [44] D. Heck et al. *CORSIKA: a Monte Carlo code to simulate extensive air showers*. Feb. 1998.
- [45] A. Capella et al. “Dual parton model”. In: *Physics Reports* 236.4-5 (1994), p. 225.
- [46] A. Fasso’ et al. “The physics models of FLUKA: status and recent development”. In: *ArXiv High Energy Physics - Phenomenology e-prints* (June 2003).

Bibliography

- [47] G. Battistoni et al. “A 3-dimensional calculation of the atmospheric neutrino fluxes”. In: *Astroparticle Physics* 12 (Jan. 2000), p. 315.
- [48] K. Werner, F.-M. Liu, and T. Pierog. “Parton ladder splitting and the rapidity dependence of transverse momentum spectra in deuteron-gold collisions at the BNL Relativistic Heavy Ion Collider”. In: 74.4, 044902 (Oct. 2006), p. 044902.
- [49] T. Pierog et al. “EPOS LHC : test of collective hadronization with LHC data”. In: *ArXiv e-prints* (June 2013).
- [50] J. Wentz et al. “Simulation of atmospheric muon and neutrino fluxes with CORSIKA”. In: *Phys. Rev. D* 67.7, 073020 (Apr. 2003), p. 073020.
- [51] S. A. Bass et al. “Microscopic models for ultrarelativistic heavy ion collisions”. In: *Progress in Particle and Nuclear Physics* 41 (1998), p. 255.
- [52] L. Baldini. “Space-Based Cosmic-Ray and Gamma-Ray Detectors: a Review”. In: *ArXiv e-prints* (July 2014).
- [53] J. Bieber et al. “Continued decline of South Pole neutron monitor counting rate”. In: *Journal of Geophysical Research (Space Physics)* 118 (Nov. 2013), p. 6847.
- [54] M. G. Aartsen et al. “Observation of the cosmic-ray shadow of the Moon with IceCube”. In: *Phys. Rev. D* 89 (10 May 2014), p. 102004.
- [55] D. Heck and T. Pierog. *Extensive Air Shower Simulations with CORSIKA: A User’s Guide*. Feb. 2016.
- [56] P. Lipari. “The geometry of atmospheric neutrino production”. In: *Astroparticle Physics* 14 (Nov. 2000), p. 153.
- [57] M. Honda et al. “Atmospheric neutrino flux calculation using the NRLMSISE-00 atmospheric model”. In: *Phys. Rev. D* 92 (2 July 2015), p. 023004.
- [58] ITMC TU Dortmund. *LiDO*. 2016. URL: http://www.mathematik.uni-dortmund.de/lsiii/lidong/lidong_systemoverview.png (visited on 07/18/2016).
- [59] C. A. Arguelles Delgado. *nuSQuIDS*. 2016. URL: <https://github.com/arguelles/nuSQuIDS> (visited on 07/18/2016).
- [60] C. A. Arguelles Delgado, J. Salvado, and C. N. Weaver. “A Simple Quantum Integro-Differential Solver (SQuIDS)”. In: *ArXiv e-prints* (Dec. 2014).
- [61] K. Daum et al. “Determination of the atmospheric neutrino spectra with the Fréjus detector”. In: *Zeitschrift fur Physik C Particles and Fields* 66 (Sept. 1995), p. 417.
- [62] R. Abbasi et al. “The energy spectrum of atmospheric neutrinos between 2 and 200 TeV with the AMANDA-II detector”. In: *Astroparticle Physics* 34 (Aug. 2010), p. 48.
- [63] The ANTARES Collaboration et al. “Measurement of the atmospheric ν_μ energy spectrum from 100 GeV to 200 TeV with the ANTARES telescope”. In: *ArXiv e-prints* (Aug. 2013).

- [64] M. G. Aartsen et al. “Measurement of the Atmospheric ν_e Flux in IceCube”. In: *Phys. Rev. Lett.* 110 (15 Apr. 2013), p. 151105.
- [65] M. Honda et al. “New calculation of the atmospheric neutrino flux in a three-dimensional scheme”. In: *Phys. Rev. D* 70 (4 Aug. 2004), p. 043008.
- [66] E. Richard et al. “Measurements of the atmospheric neutrino flux by Super-Kamiokande: energy spectra, geomagnetic effects, and solar modulation”. In: *ArXiv e-prints* (Oct. 2015).

Acknowledgements

Contrary to their own insistence theoretical physicists don't enjoy working in a frictionless vacuum very much. And not unlike Conway's game of life no thesis can grow in isolation. I would like to use this opportunity to express my gratitude to all the people who helped turning this thesis from possibility to reality.

- Zuerst möchte ich meiner Doktormutter Prof. Dr. Julia Tjus danken. Dafür, dass sie mir die Möglichkeit gegeben hat dieses Thema zu bearbeiten und für die vielen hilfreichen Diskussionen und Ratschläge zum Inhalt und ihre Unterstützung bei Problemen mit der Anfertigung dieser Arbeit: Vielen Dank!
- Außerdem danke ich meinem Zweitbetreuer Prof. Dr. Evgeny Epelbaum für seine Unterstützung.
- Dem Zweitgutachter meiner Arbeit, Prof. Dr. Dr. Wolfgang Rhode danke ich für die Verbindung zu Frau Tjus während meiner Diplomarbeit, die letztendlich zu dieser Arbeit führte.
- Besonderer Dank gebührt Dr. Anatoli Fedynitch, der mich mit dem Thema dieser Arbeit vertraut gemacht hat und dessen Projekt ich weiterführen durfte. Für die Unterstützung bei allen technischen Schwierigkeiten und die hilfreichen Erklärungen: Dankeschön!
- Allen gegenwärtigen und ehemaligen Mitgliedern der Arbeitsgruppe von Frau Tjus danke ich für interessante Diskussionen, und viel mehr noch für all die erheiternden Blödeleien. Insbesondere danke ich Dr. Florian Schuppan für die Durchsicht dieser Arbeit und seine hilfreichen Anmerkungen, Fabian Bos danke ich für seine Hilfe mit NuSQUIDS, Lukas Merten danke ich für den regen Austausch über python und die Einführung in Pandas.
- Dem Systemadministrator des Lehrstuhls, Bernd Neubacher, möchte ich dafür danken, dass er mir eine Menge an Rechenleistung zur Verfügung stellte, die die Anfertigung dieser Arbeit sehr beschleunigt hat.
- Den Mitgliedern der Arbeitsgruppe von Herrn Rhode in Dortmund danke ich für den regen Austausch in allen Dingen IceCube. Insbesondere möchte ich Dr. Florian Scheriau und Dr. Martin Schmitz danken, für die anregenden Diskussionen über atmosphärische Neutrinos und ihren Einsatz als Betatester für ANflux.

Bibliography

- I would like to thank every member of the IceCube collaboration for creating an environment full of uniquely brilliant people that is truly inspirational. In particular I would like Dr. Paolo Desiati for making me feel welcome in the collaboration and for his interest in my work. Furthermore, I would like to thank Dr. Jakob van Santen, Dr. Chris Weaver and Dr. Carlos Aguelleres for their help with CORSIKA and NuSQUIDS.
- Auch meinen ehemaligen Kollegen bei der Startext möchte ich danken: Zuerst dem Gründer Paul Bantzer für die Chance Teil des Teams zu sein, Noel Marx von dem ich viel über Programmierung gelernt habe und Alexander Herschung der mir gezeigt mit widerspenstigen Daten und Formaten umzugehen.

Sebastian Schöneberg

Lebenslauf Sebastian Schöneberg

Angaben zur Person

Name Schöneberg, Sebastian
Adresse Deutsch-Luxemburger Str. 128
44225 Dortmund
Geboren am 15.9.1985 in Bonn-Duisdorf
Familienstand ledig

Studium

seit 2012 Promotion Physik an der Ruhr-Universität Bochum
Thema *The spectrum of atmospheric neutrinos above GeV energies*
Betreuer Prof. Dr. Julia Becker Tjus
09.7.2012 Diplom Physik
Thema *Klassifikation von Starburst Galaxien für Source Stacking Analysen*
Betreuer Prof. Dr. Dr. Wolfgang Rohde
Prof. Dr. Julia Becker Tjus
2004–2012 Studium Physik an der TU Dortmund

Schulbildung

23.07.2004 International Baccalaureate Diploma
25.06.2004 Abitur
2002–2004 Friedrich-Ebert-Gymnasium Bonn - Dualer Bildungsgang Abitur und International Baccalaureate
1996–2002 Friedrich-Ebert-Gymnasium Bonn - bilingual deutsch-französischer Zweig
1993–1996 Grundschule Hachenburg
1992–1993 Münsterschule - Gemeinschaftsgrundschule Bonn